School of Advanced Studies

Chemical and Pharmaceutical Sciences and Biotechnology

PhD Curriculum: Chemical Sciences

XXXI Cycle

_____

Environmental Remediation by Light Driven Advanced Oxidation Processes: Pollutant Degradation and Bacterial Disinfection

Scientific Sector CHIM/12

PhD Student   **Supervisor Unicam**

Dr. Elena Rommozzi   *Dr. Rita Giovannetti*

_____

XXXI Cycle 2015/16-2018/19

To my Parents
To my Sister
To my Husband
To my Daughter

"You are the love of my life.
Everything I have and everything I am is yours.
Forever."

Preface

This PhD thesis in Chemical Science started in November 2015 at the School of Advanced Studies of University of Camerino.

The research activity described in this PhD thesis was carried out at University of Camerino in the School of Science and Technology (Dr. Rita Giovannetti's Research Group) and at École Polytechnique Fédérale de Lausanne in the Institut des Sciences et Ingénierie Chimiques (Prof. César Pulgarin's Research Group).

In this PhD thesis, after a "GENERAL INTRODUCTION" about the aim of the PhD project, are reported an INTRODUCTION regarding environmental and water pollution and Advanced Oxidation Processes, in Chapter 1, and two successive Sections.

In Section 1, entitled "GRAPHENE BASED TiO_2 NANOCOMPOSITES FOR PHOTOCATALYTIC DEGRADATION OF SYNTHETIC DYES", are present three Chapters. After a general introduction in Chapter 2 on TiO_2 and Graphene-TiO_2 photocatalysis, in Chapter 3 and Chapter 4 are reported all obtained results.

In particular, in Chapter 3 is reported the first work regarding the preparation and optimization of a new heterogeneous photocatalyst constituted by TiO_2 and graphene prepared by exfoliation of graphite, with a special attention into preparation and characterization of graphene dispersion. The new graphene-TiO_2 photocatalyst was used for the photodegradation of Alizarin Red S solution under visible light irradiation. Meanwhile, in Chapter 4 is reported the second work regarding the preparation, optimization and characterization of a new heterogeneous photocatalyst constituted by TiO_2 and reduced graphene oxide prepared by thermal reduction of graphene oxide, with a special attention into preparation and characterization of reduced graphene oxide dispersion. As in the case of Chapter 3, the new reduced graphene oxide-TiO_2 photocatalyst was used for the photodegradation of Alizarin Red S solution under visible light irradiation.

In Section 2, entitled "SOLAR DISINFECTION AND PHOTO-FENTON PROCESSES FOR BACTERIA INACTIVATION IN WATER", are present two Chapters. After a general introduction in Chapter 5 on Solar Disinfection and Photo-Fenton treatments for water depuration, in Chapter 6 are reported all obtained results.

In particular, the effect of the presence of various inorganic ions, which individually or in combination with each other can act as scavenger of OH radicals or can produce additional OH radicals or other

active radical species on inactivation of Escherichia Coli with Solar Disinfection and Photo-Fenton processes is discussed in detail.

Results of this PhD thesis are published and/or submitted for publication in scientific international journals and presented as Congress communications.

Publications:

R. Giovannetti, **E. Rommozzi**, M. Zannotti, C. A. D'Amato, S. Ferraro, M. Cespi, G. Bonacucina, M. Minicucci and A. Di Cicco, Exfoliation of graphite into graphene in aqueous solution: an application as graphene/TiO_2 nanocomposite to improve visible light photocatalytic activity, *RSC Advances*, 2016, 6, 93048; doi: 10.1039/c6ra07617c.

R. Giovannetti, **E. Rommozzi**, M. Zannotti and C. A. D'Amato, Recent Advances in Graphene Based TiO_2 Nanocomposites ($GTiO_2Ns$) for Photocatalytic Degradation of Synthetic Dyes, *Catalysts*, 2017, 7, 305; doi:10.3390/catal7100305.

E. Rommozzi, M. Zannotti, R. Giovannetti, C. A. D'Amato, S. Ferraro, M. Minicucci, R. Gunnella and A. Di Cicco, Reduced Graphene Oxide/TiO_2 Nanocomposite: From Synthesis to Characterization for Efficient Visible Light Photocatalytic Applications, *Catalysts*, 2018, 8, 598; doi:10.3390/catal8120598.

E. Rommozzi, S. Giannakis, R. Giovannetti and C. Pulgarin, Which ions hold photo-chemical implications during solar and photo-Fenton inactivation of bacteria in natural waters? A systematic assessment, in preparation for submission.

Congress Communications:

R. Giovannetti, M. Zannotti, C. A. D'Amato, S. Ferraro, M. Minicucci and **E. Rommozzi**, Graphene/TiO_2 Nanocomposite for Efficient Visible-Light Photocatalysis: Synthesis, Characterization and Photocatalytic Applications. GraphITA 2015, Bologna, Italy.

E. Rommozzi, R. Giovannetti, M. Zannotti, C. A. D'Amato, S. Ferraro, M. Cespi, G. Bonacucina, M. Minicucci, A. Di Cicco, From TiO_2 and Graphite to Graphene doped TiO_2 for photocatalytic

applications, ISBN 9788867680269. 5th Scientific Day of the School of Science and Technology, 2016, Camerino, Italy.

E. Rommozzi, M. Zannotti, C. A. D'Amato, R. Giovannetti, S. Ferraro, Two different graphene: which of the two is the best in the photocatalytic activity of TiO_2 under visible light?, ISBN 9788867680368. 6th Scientific Day of the School of Science and Technology, 2018, Camerino, Italy.

During this PhD other studies were also performed and are published in scientific international journals.

Abstract: The effect of pH change on 5, 10, 15, 20-Tetrakis(4-hydroxyphenyl)-21H,23H-porphine (THPP) with its aggregation as function of water-ethanol mixture was studied with UV–Vis, fluorescence, Raman and computational analysis. In neutral pH, THPP was present as free-base and, increasing the water amount, aggregation occurred with the formation of H- and J-aggregates. The aggregation constant and the concentration of dimers were calculated, other information about the dimer aggregation were evaluated by computational study. In acidic pH, by the insertions of two hydrogens in the porphyrin rings, the porphyrin changed its geometry with a ring deformation confirmed by red-shifted spectrum and quenching in fluorescence; at this low pH, increasing the water amount, the acidic form $(THPPH_2)^{2+}$ resulted more stable due to a polar environment with stronger interaction by hydrogen bonding. In basic pH, reached by NH_4OH, THPP porphyrin was able to react with alkali metals in order to form sitting-atop complex (M_2THPP) confirmed by the typical absorption spectrum of metallo-porphyrin, Raman spectroscopy and by computational analysis.

Abstract: A new approach to obtain a heterogeneous photocatalytic material with gold nanoparticles and TiO_2 semiconductor was performed exploiting the reducing ability of acetylacetone, a chemical

present in the TiO$_2$ paste formulation. Gold/TiO$_2$ heterogeneous catalyst supported on polypropylene [PP@Au-TiO$_2$]$_A$ was prepared; composition, structure and morphology of this new material were defined by using UV–Vis spectroscopy, Scanning Electron Microscopy (SEM), Atomic Force Microscopy (AFM), X-ray diffraction (XRD), X-ray Fluorescence (XRF), Raman Spectroscopy, Photoluminescence and Diffuse Reflectance Spectroscopy. The new material was tested in the photocatalytic degradation of Alizarin Red S in water solution, as target pollutant, under visible light and correlated with structural and spectroscopic characterizations. [PP@Au-TiO$_2$]$_A$ showed higher photocatalytic activity respect to pure [PP@TiO$_2$]$_A$ with an improvement of photodegradation kinetic. The best performance was obtained using [PP@Au-TiO$_2$]$_A$ sample with 0.006 wt.% of Au and the photocatalytic improvement was correlated with the band gap energy decrease of photocatalyst.

C. A. D'Amato, R. Giovannetti, M. Zannotti, **E. Rommozzi**, M. Minicucci, R. Gunnella, A. Di Cicco,

Abstract: The effect of surface modification using ascorbic acid as a surface modifier of nano-TiO$_2$ heterogeneous photocatalyst was studied. The preparation of supported photocatalyst was made by a specific paste containing ascorbic acid modified TiO$_2$ nanoparticles used to cover Polypropylene as a support material. The obtained heterogeneous photocatalyst was thoroughly characterized by scanning electron microscope (SEM), RAMAN, X-ray diffraction (XRD), X-ray photoelectron spectroscopy (XPS), photoluminescence (PL), and Diffuse Reflectance Spectra (DRS) and successfully applied in the visible light photodegradation of Alizarin Red S in water solutions. In particular, this new supported TiO$_2$ photocatalyst showed a change in the adsorption mechanism of dye with respect to that of only TiO$_2$ due to the surface properties. In addition, an improvement of photocatalytic performances in the visible light photodegration was obtained, showing a strict correlation between efficiency and energy band gap values, evidencing the favourable surface modification of TiO$_2$ nanoparticles.

Contents

CHAPTER 6. WHICH IONS HOLD PHOTOCHEMICAL IMPLICATIONS DURING SODIS AND PHOTO-FENTON INACTIVATION OF BACTERIA IN NATURAL WATER? A SYSTEMATIC ASSESSMENT

GENERAL INTRODUCTION

Water resources, that are essential to support physiological activities of any biological cell [1], to maintaining human life, health, agricultural production and economic activities, are continuously subject to pollution impact from industrial and natural chemical compounds. Due to toxicity, stability to natural decomposition and persistence in the environment, these pollutants have caused many problems in the water resources. For this, water pollution is a major cause of global concern as it leads to onset of numerous fatal diseases [2].

Among many technologies for the wastewater treatment utilized to remove contaminants such as dyes, drugs, pesticides and bacteria or to degrade them into harmless products [3], recent developments attracting considerable interest regarded the improvement of Advanced Oxidation Processes (AOPs) [4, 5]. The main purpose of AOPs is the mineralization of refractory organic substances and/or the inactivation of bacteria or viruses. All AOPs are characterized by the production of highly reactive species as hydroxyl (OH) radicals [6] by a strong oxidizing agent and/or catalyst in presence of an irradiation source [6, 7].

In the large group of light driven AOPs, photocatalytic degradation of organic pollutants using TiO_2, has attracted considerable attention for water depuration [8] since the discovery of its photocatalytic properties by Fujishima and Honda [9, 10]. In the application of TiO_2 as photocatalyst, there are two limitations; the first is referred to the absence of photoactivity under visible light due to its wide band gap (3.2 eV) [11 - 13] and the second is the fast recombination rate of electron-hole pairs that decreases the efficiency of photocatalytic reactions [14, 15]. The combination of TiO_2 with graphene [56 - 59] represents a possible solution. Graphene is in fact an ideal nanomaterial for this purpose thanks to its properties that extend the visible light absorption of TiO_2 [16, 17] and reduces the electron-hole recombination enhancing therefore its photocatalytic efficiency [18].

Another process in which the potential of solar light is used to disinfect drinking water from chemical and microbial contaminants is Solar Disinfection (SODIS) [19]. This process exploit the ability of solar light to kill pathogens through genome damages and intracellular oxidative reactions [20] and can be enhanced by the addition of various chemicals [21]. A widely studied AOP in this field is the photo-Fenton process in which OH radicals are generated using light, iron and hydrogen peroxide and act as oxidant species in water treatment [22, 23]. Particularly, photo-Fenton system involves reactions of H_2O_2 with Fe^{2+} ions leading to the formation of Reactive Oxygen Species (ROS) and

reactive radical species, like OH radicals and other less reactive radicals, that are highly oxidant species for the inactivation of bacteria and viruses [24].

In this PhD thesis, the fundamental knowledge and the research approach of different light driven AOPs for water depuration are presented. Different AOPs was applied to chemical contaminant depuration and to water disinfection respectively, as schematized in Figure 1.

The application in the chemical contaminant depuration was performed in two steps. The first step was referred to the preparation and characterization of different materials: graphene and graphene/TiO_2 nanocomposites. The second step regarded the applications of as prepared photocatalysts in the visible light photodegradation of Alizarin Red S as target water pollutant.

In the water disinfection application, conducted during the abroad period in Pulgarin's research group, the effect of inorganic ions and natural organic matter present in aqueous E. Coli suspension on both SODIS and photo-Fenton processes was studied. These compounds, individually or in combination with each other, can act as scavenger of OH radicals, otherwise can produce additional OH radicals or other active radical species, decreasing or improving the efficiency of both processes.
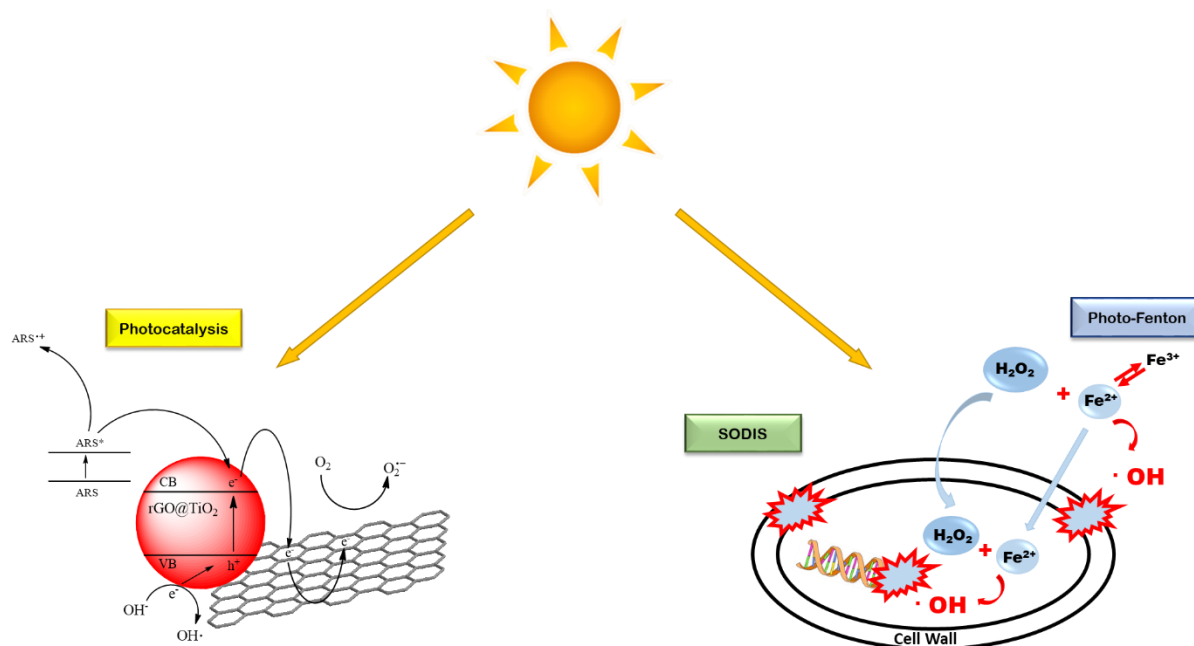
Figure 1: *Light driven AOPs for water depuration.*

References

[1] D. H. Kumar Reddy and S.M. Lee, *J. Environ. Anal. Toxicol.*, 2012, 2, 5.

[2] A. Agrawal, R. S. Pandey and B. Sharma, *J. Water Res. Prot.*, 2010, 2, 432-448.

[3] R. B. M. Bergamini, E. B. Azevedo, L. R. Raddi de Araujo, *Chem. Eng. J.*, 2009, 149, 212–220.

[4] P. R. Gogate, A. B. Pandit, *Adv. Environ. Res.*, 2004, 8, 501–551.

[5] I. Oller, S. Malato, J. A. Sánchez-Pérez, *Sci. Total. Environ.*, 2011, 409, 4141–4166.

[6] R. Andreozzi, V. Caprio, A. Insola, R. Marotta, *Catal. Today*, 1999, 53, 51–59.

[7] Y. Deng, R. Zhao, *Curr Pollution Rep*., 2015, 1, 167–176.

[8] M. R. Hoffmann, S. T. Martin, W. Choi, D. W. Bahneman, *Chem. Rev.*, 1995, 95, 69–96.

[9] S. Kalathil, M. M. Khan, S. A. Ansari, J. Lee, M. H. Cho, *Nanoscale,* 2013, 5, 6323–6326.

[10] R. Asahi, T. Morikawa, T. Ohwaki, K. Aoki, Y. Taga, *Science,* 2001, 293, 269–271.

[11] V. Iliev, D. Tomova, L. Bilyarska, G. Tyuliev, *J. Mol. Catal. A-Chem.,* 2007, 263, 32–38.

[12] A. Mills, C. O'Rourke, K. Moore, *J. Photoch. Photobio. A,* 2015, 310, 66–105.

[13] A. Truppi, F. Petronella, T. Placido, M. Striccoli, A. Agostiano, M. L. Curri, R. Comparelli, *Catalysts,* 2017, 7, 100.

[14] W. Qian, P. A. Greaney, S. Fowler, S. K. Chiu, A. M. Goforth, J. Jiao, *ACS Sustainable Chem. Eng.,* 2014, 2, 1802−1810.

[15] K. Hashimoto, H. Irie, A. Fujishima, *Jpn. J. Appl. Phys.,* 2005, 12, 8269–8285.

[16] C. Lee, X. Wei, J. W. Kysar, J. Hone, *Science*, 2008, 321, 385–388.

[17] M. D. Stoller, S. Park, Y. Zhu, J. An, R. S. Ruoff, *Nano Lett.*, 2008, 8, 3498–3502.

[18] H. Zhang, X. Lv, Y. Li, Y. Wang, J. Li, *ACS Nano*, 2010, 4, 380–386.

[19] K. G. McGuigan, R. M. Conroy, H. J. Mosler, M. du Preez, E. Ubomba-Jaswa, P.Fernandez-Ibanez, *J. Hazard. Mater.*, 2012, 235–236, 29–46.

[20] S. Giannakis, *Environ. Sci. Pollut.,* 2018, 1–17.

[21] S. Kehoe, T. Joyce, P. Ibrahim, J. Gillespie, R. Shahar, K. McGuigan, *Water Res.*, 2001, 35, 1061–1065.

[22] S. Giannakis, M. I. Polo Lòpez, D. Spuhler, J. A. Sànchez Pèrez, P. Fernàndez Ibànez, C. Pulgarin, *Appl. Catal. B Environ.*, 2016, 199, 199–223.

[23] S. Giannakis, M. I. Polo Lòpez, D. Spuhler, J. A. Sànchez Pèrez, P. Fernàndez Ibànez, C. Pulgarin, *Appl. Catal. B Environ.*, 2016, 198, 431–446.

[24] G. Ruppert, R. Bauer, G. Heisler, *J. Photochem. Photobiol., A: Chem.*, 1993, 73, 75–18.

CHAPTER 1. INTRODUCTION

1.1. Environmental Pollution

Environmental pollution is one of the most serious problems facing humanity and other life forms on our planet today. Environmental pollution is defined as "the contamination of the physical, chemical and biological components of the Earth system to such an extent that normal environmental processes are adversely affected" [1].

There are several kinds of environmental pollution and all types of pollution are interconnected. The main ones are the following five:

- **Air pollution** [2]**:** it involves any contamination of the atmosphere that modifies the natural composition of the air. It can be in the form of particulate matter such as dust or excessive gases like carbon dioxide or other vapours. It comes from a wide range of sources, natural and not. Depending on the concentration of air pollutants, several effects can be noticed, such as smog increases, higher rain acidity, crop depletion from inadequate oxygen and higher rates of asthma.

- **Water pollution** [3]**:** it involves any contaminated water, whether from chemical, particulate, or bacterial matter that decreases the quality and purity of water. It can occur in every source of water like oceans, rivers, lakes, underground reservoirs and because different water sources flow together, this kind of pollution can very quickly spread causing various environmental problems. The effects of water pollution include the decrease of the amount of drinking water available, the lower water supplies for crop irrigation and the impact on fish and wildlife populations that require water of a certain purity for survival.

- **Soil pollution** [4]**:** it is a contamination of the soil that prevents natural growth and balance in the land, whether it is used for farming, housing, or preserving wildlife. Some cases of soil pollution, such as the creation of landfills, are deliberate, while many more are accidental and can have widespread effects. It can lead to poor growth and reduced crop yields, to loss of wildlife habitat, to soil erosion, and to desertification.

- **Noise pollution** [5]**:** it refers to undesirable levels of noises caused by human activity that disrupt the standard of living in the affected area. Some noise pollution sources may be

temporary, while other are permanent. Effects may include hearing loss, wildlife disturbances, and a general degradation of lifestyle.

- **Light pollution** [6]**:** it is due to the over illumination of an area that is considered obtrusive. It interfere with astronomical observation and personal enjoyment. If it is near residential areas, can also degrade the quality of life for residents.

Pollution is the introduction of contaminants into the natural environment. A contaminant is an external agent which is added into the environment and that causes a change in its composition. It is a biological, chemical or physical substance, which, in enough concentration, can negatively affect living organisms through air, water, soil and/or food. These substances are not present in the normal composition of natural system or they are at a very low concentration.

Generally, pollutants are grouped in two classes [7]:

- Anthropogenic: pollutants caused or produced by human activity. They represent the main health and environmental problems such as bad air quality, global warming and destruction of the ozone layer.
- Natural: pollutants created by substances of natural origin such as volcanic dust, sea salt particles, photo-chemically formed ozone and products of forest fibres, among others.

Both anthropogenic and natural contaminants can be classified into [7]:

- Biodegradable: easily degraded by the biological activity of microorganism and enter the biogeochemical cycles. These pollutants are natural organic substances, which can be decomposed, removed or consumed and thus, reduced to acceptable levels either by natural processes, like biological or microbiological action, or by some engineered systems, like sewage treatment plants.
- Non-Biodegradable: hard to destroy due to their resistant chemical structure. Between these substances, insecticides and other pesticides, mercury, lead and arsenic are the most important pollutant. Many of these pollutants are accumulated in the environment and are biologically magnified as they move along the food chain These may also react with other compounds in the environment to produce toxins.

Moreover, contaminant species can be classified as primary or secondary pollutants. They are distinguished according to their chemical composition, their physical state and their reactivity in the

atmosphere. Primary pollutants are substances that are directly released in the environment and remain in their original form, while secondary pollutants are substances that are formed by chemical reactions between primary pollutants and constituents of the environment.

Although pollution exist since life began, it has seen a strong growth since the onset of the industrial revolution in the 19th century. Factors such as population growth, technological advancement, and urbanization lead to a very quick increase of environmental diseases [1].

In the last years, a fast evolution of research activities oriented to environment protection has been recorded due to the special attention paid to the environment by social, political and legislative international authorities leading to the delivery of very strict severe regulations [8]. Many studies are aimed in searching for new ecologically sustainable methods for cleaning the environment [8, 9]. For those reasons, various solutions have already been designed but only some of them really remove the pollutants and also they require additional processes to eliminate toxic compounds. The usual methods used for clean-up environmental system, even if effective, are often more intensive of a chemical point of view and their residues can represent additional problems of contamination.

1.2. Water Pollution

Water resources are vital for maintaining human life, health, agricultural production and economic activities. Water quality is important in our lives because it is essential to support physiological activities of any biological cell [10]. Unfortunately, water resources are gradually becoming polluted and unavailable because of the increasing contamination of systems with industrial and natural chemical compounds. A serious problem derives from the growing number of contaminants that are entering in water resources from industrialization and human activity, such as heavy metals, dyes, pharmaceuticals, pesticides, insecticides, detergents and so on [11].

Water pollution is the contamination of water bodies such as lakes, rivers, oceans and groundwater by human activities; this may be defined in terms of the undesirable changes in chemical and physical properties of water. All water pollution affects organisms and plants that live in water bodies and in almost all cases the effect is damaging to the individual species, to population and to the natural biological communities. Water pollution occurs when pollutants are discharged directly or indirectly into water bodies without adequate treatment to remove harmful constituents. Therefore, organic compounds are often present as pollutants in wastewater. Water pollution is a major cause of global

concern as it leads to onset of numerous fatal diseases that is responsible for the death of over 14.000 people every day [12].

Water pollutants sources can be categorized in two main categories [7]:

- Point Source (PS): harmful substances are emitted directly into a body of water. Outlet pipes of industrial facilities or wastewater treatment plants are examples of point sources.
- Non-Point Source (NPS): pollutants are released indirectly through environmental change. NPS usually results from precipitation, atmospheric deposition, drainage or hydrologic modification. NPS pollution is often the cumulative effect of small amounts of contaminants accumulated from a large area.

Several technologies can monitor and regulate PS, whereas NPS are much more difficult to control. It is indispensable to remove these contaminants and to develop methods for the degradation of toxic or non-biodegradable compounds from wastewater. Toxicity, stability to natural decomposition and persistence in the environment of pollutants have caused many problems that regard their decomposition. In fact, some of these compounds are not amenable to microbial degradation [13]. Water always requires some treatments prior to reuse; the extent of these treatments depends on the contamination degree. Biological processes are more natural and easier to implement, but they have the drawback of the sludge production proportionally to the volume of treated water. In this field, chemical treatments are better than biological processes because with them the contaminant is not being transferred, but concerted, or in the ideal case mineralized; however, their application is restricted due to high cost, poor degradation efficiency, secondary pollution and complicated technology [14].

Many technologies for the wastewater treatment have been developed to remove contaminants such as dyes, drugs, pesticides and bacteria or to degrade them into non-toxic ones. Recent developments in chemical water treatment have led to an improvement of Advanced Oxidation Processes (AOPs) [15, 16]. These technologies have been attracting considerable interest because they are more effective and sustainable in the long term.

1.2.1. Dye Wastewater Pollution

Dyes are an important class of synthetic organic compounds that are found in water bodies coming from different sources such as textile industries, paper and pulp industries, pharmaceutical industries, tannery and so on. Residual dyes from these sources, even in low concentrations, are considered as a large class of pollutants introduced on water resources. Fifteen percent of the total world production of dyes is lost during dyeing process and is released in wastewater. The release of those coloured wastewaters in the ecosystem is a source of aesthetic pollution, of eutrophication and of perturbations of aquatic life [17]. In fact, the discharge of dyes into water environment is unwanted because of their colour and because many released dyes and their breakdown products are toxic, carcinogenic or mutagenic to life forms. In addition, these wastewaters contain considerable amounts of non-fixed dyes and a huge amount of inorganic salts [18].

For all these reasons, it is necessary that water contaminated by dyes undergo treatment before wastewater disposal. There are many effluent treatment methods [19], as reported in Table 1.1, including various physical, chemical and biological procedures, but none of them is completely satisfactory.

*Table 1.1: Effluent Treatment Methods [**Errore. Il segnalibro non è definito.**].*

Physical Method	Chemical Method	Biological Method
Sedimentation	Neutralization	Stabilization
Filtration	Reduction	Aerated Lagoons
Coagulation	Oxidation	Trickling Filters
Reverse Osmosis	Catalysis	Activated Sludge
Solvent Extraction	Ion Exchange	Anaerobic Digestion
Adsorption	Electrolysis	Fungal Treatment
Incineration		Flocculation
Distillation		
Membrane Treatment		

Because of their synthetic origin and their complex structure, many dyes are stable and refractory making them difficult to destroy [19]. For this, most of these methods are not destructive but permit only to transfer the contamination from one phase to another, resulting in a new or different kind of

pollution that need to be treated [20]. In the last years, a wide range of technologies have been developed to remove dyes from wastewaters and to reduce their impact on the environment improving the quality of life.

1.2.1.1. Structure and Properties of Dyes

Dyes are water-soluble compounds and are very difficult to remove by conventional treatment systems. Unlike most organic compounds, dyes present a characteristic colour due to the absorption of visible light by structures named chromophores, having a conjugated system and exhibiting electronic resonance [21].

From a chemical point of view, a dye molecule can be characterized by [22]:

- The basic structure, which is related to a dye family and contains chromophores that induce coloration to the solution; placement of chromophores in different parts of dye structures can lead to different colours.

- The substituents or auxochromes groups, which interfere with aqueous solubility by ionization and can enhance conjugation in the dye molecule. Auxochromes groups are not responsible for colour but their presence can shift the colour of a colorant.

The most important families of dyes are azo-compounds and anthraquinone.

Azo dyes [23] are characterized by at least an azo bond (-N=N-) connected to aromatic or heterocyclic rings, as shown in the chemical structure of Methyl Orange, a common azo dye, reported in Figure 1.1, but can contain two, three, or, more rarely, four or more azo groups.
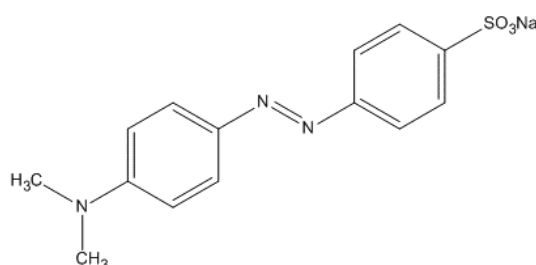
Figure 1.1: *Chemical structure of Methyl Orange, a common azo dye.*

Azo dyes are a ubiquitous class of dyes produced by textile fibres or by diazotization of a primary aromatic amine followed by coupling of the resulting diazonium salt with a nucleophile [24]; about 50-70% of available dyes on market are azo compounds.

Anthraquinone dyes [25] are derivatives of substituted anthraquinone and have two carbonyl groups in their chemical structure. Various substitutes can be found, such as alkyl, amino, hydroxyl, halogen, sulphate or more complex groups. One of the main examples of anthraquinone derivatives used as dyes is Alizarin and its derivative sodium salt, Alizarin Red S. Chemical structures of Alizarin and Alizarin Red S are reported in Figure 1.2.
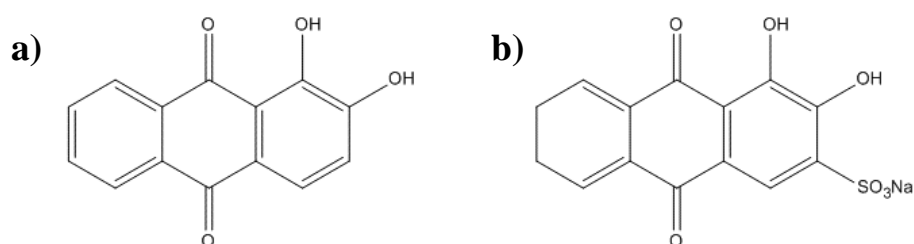
Figure 1.2: Chemical structure of Alizarin (a) and Alizarin Red S (b), common anthraquinone dyes.

Anthraquinone dyes are used in many fields like cotton and silk dyeing, clinical application and geologic field [26, 27].

1.2.2. Bacterial Wastewater Pollution

Most of the current outbreaks of diseases in the world can derive from water contaminated by bacteria, as examples cholera, caused by Vibrio Cholera, diarrhoea and dysentery, caused by Escherichia Coli and food poisoning and typhoid, caused by Salmonella Typhi [28]. These pathogens are the main cause of diseases leading to mortality in developing countries. In fact, it has been recently reported that over 1.3 million deaths of children are caused by diarrhoeal illness, linked to unsafe water supply and hygiene, worldwide every year [29 - 31].

These kind of bacteria are naturally present in the intestines of warm-blooded animals. Human sources of these bacteria include failing septic tanks and leaking sewer lines, while animal source includes manure spread from livestock on land, or streams, and improper disposal of farm animal wastes. The source of infection may be due to the transportation of manure to groundwater by leaching and precipitation [32, 33].

The most common method used for removal, deactivation or killing of pathogenic microorganisms in water is chlorination [31]; this is due to the effectiveness of chlorine, to its low cost and its extra protection against regrowth of bacteria and pathogens. Nevertheless, the addition of these chemicals alter the flavour of water and react with various constituents to form disinfection by-products, many of which are carcinogens. In addition, bacteria have developed chlorine-induced antibiotic resistance [34] and, in the last years, a wide range of technologies have been developed to remove bacteria from wastewaters and to reduce their impact on quality of life.

1.2.2.1. Structure and Properties of Bacteria

Bacteria are extremely numerous and the total biomass of bacteria on Earth is more than all plants and animals combined.
Bacteria are unicellular prokaryotic microorganisms that do not have a nucleus and are less complex than eukaryotic cells. Their DNA is located in a nucleoid which is an irregularly shaped region that does not have a nuclear membrane. Bacteria also have a cell membrane and a cell wall that, together, are referred to as the cell envelope [35].
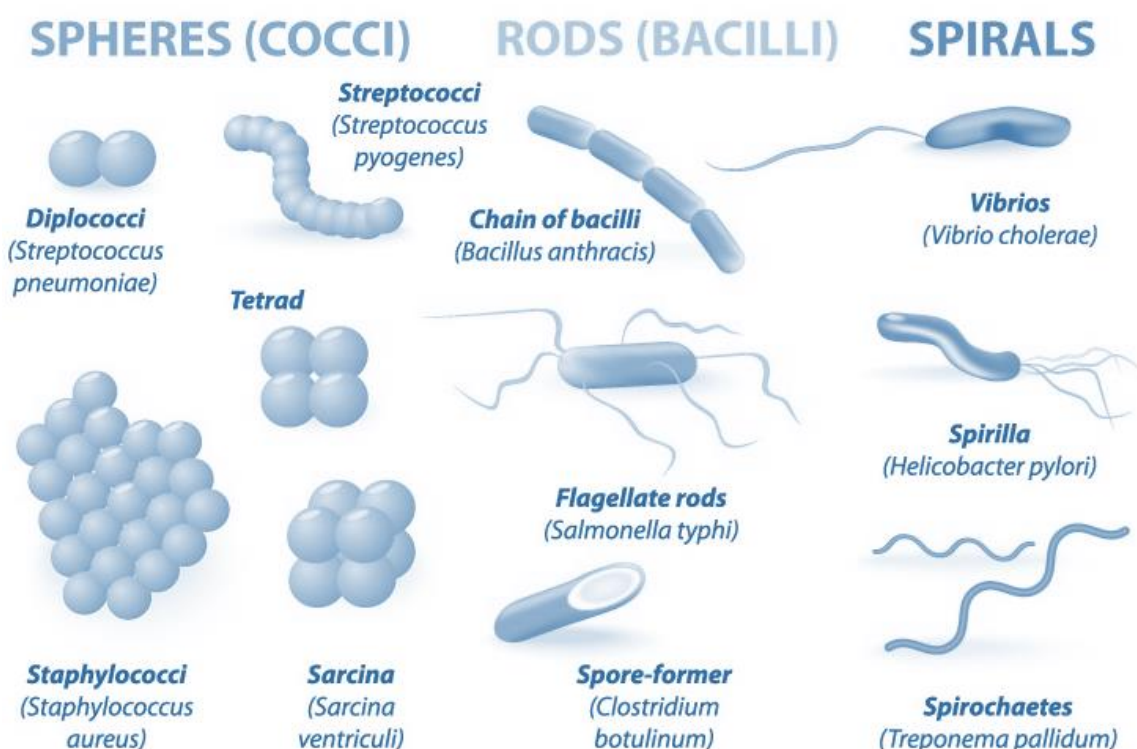
Figure 1.3: *Bacterial morphology diagram.*

Bacteria exist in different forms, such as filamentous, square, star-shaped and stacked, but the main shapes are classified as follow and shown in Figure 1.3 [36]:

- Cocci: bacteria that are spherical or ovoid in shape. Some cocci remain attached after binary fission, even though separate cells have been formed. For example, diplococci are cocci in pairs, streptococci are chains, and staphylococci are clusters of multiple cocci.
- Spiral bacteria: bacteria with a spiral-shaped. Spirillums are thick, tough spirals. Spirochetes are spirals that are thin and flexible. Vibrios are comma-shaped rods with a small twist.
- Bacilli: bacteria with rod-shaped. Like cocci, bacilli can be solitary or arranged together. Diplobacilli are two bacilli arranged next to each other, and streptobacilli are chains of bacilli.

One example of a common species of bacteria is Escherichia Coli [35]. They are bacillus-shaped bacteria and are found naturally in the intestine of many animals including humans, where they produce vitamin K and B-complex vitamins. Escherichia Coli is often used in laboratory research since it reproduces itself quickly and is very hardy. Most strains of Escherichia Coli are harmless to humans, but in some cases can cause infection that can result in gastrointestinal problems like diarrhoea, and in more severe cases, in bacterial meningitis or pneumonia.

1.3. Advanced Oxidation Processes

Typical processes used to treat wastewater are physical, chemical and biological but each of these methods present some disadvantages and are clearly not suitable to treat toxic and non-biodegradable organic pollutants; for this purpose, new treatment methods have been developed and tested [37].

Recent developments in chemical water treatment have led to an improvement of Advanced Oxidation Processes (AOPs) [38, 39]. These technologies have been attracting considerable interest because they are more effective and sustainable in the long term, compared to traditional methods [37].

All AOPs are characterized by the same chemical feature: the production of highly reactive species as hydroxyl (OH) radicals, that have the power to destroy pollutants with a constant rate usually in the order of $10^8 - 10^{10}$ M^{-1} s^{-1} [40]; they have also a little selectivity of attack that is useful for solving pollution problems [8]. For the production of OH radicals, AOPs generally offer different possible

ways using a strong oxidizing agent and/or catalyst in presence or absence of an irradiation source [8, 40]. The main purpose of AOPs is the mineralization of refractory organic substances that are present in industrial effluents; final products are carbon dioxide, water and inorganic compounds or, at least, the transformation of refractory organic substances into harmless products [41]. Main advantages of AOPs are high rates of pollutant oxidation, flexibility concerning water quality variations and small dimension of the necessary equipment; main disadvantages include high treatment costs, special safety requirements due to the use of very reactive chemicals and high energy sources [42].

A list of the different possibilities offered by AOPs for OH radicals production is as follows:

- **Semiconductor Photocatalysis:** Process that use a metal oxide semiconductor as catalyst and oxygen as oxidizing agent [43].The first step of photocatalytic process is the absorption of UV-Vis radiation with the formation of electron-hole pairs on semiconductor material. Successively, the formed electrons allow to reduce the dissolved oxygen with the formation of the superoxide radical ions, on the other hand holes are able to oxidize adsorbed water or hydroxide ions to HO radicals [8]. Finally, these radicals lead to the removal of a wide range of organic compounds.

- **Fenton and Photo assisted Fenton Processes:** Production of OH radicals by Fenton reagent occurs by the addition of H_2O_2 and Fe^{2+} salts to the reaction system [44]. This reactant is an attractive oxidative system for wastewater treatment because iron is a very abundant and non-toxic element and hydrogen peroxide is easy to manage and environmentally safe [8]. The degradation rate of organic pollutant with Fenton reagent is strongly accelerated by irradiation with UV-Vis light in Photo-Fenton processes [45, 46].

- **Ozone Water System:** The ozone decomposition in aqueous solution, based on O_3/H_2O_2 and O_3/UV processes, develops through the formation of OH radicals by the ozone chemistry in alkaline conditions, leading to the decomposition of organic pollutants.

Among various AOPs, the photocatalytic degradation of organic pollutants using semiconductor metal oxide, particularly TiO_2, has attracted considerable attention for water depuration [47].

TiO_2 has been widely studied as good photocatalyst for water purification from pollutants since the discovery of its photocatalytic properties by Fujishima and Honda [48, 49]. This semiconductor material presents different advantages such as high efficiency for the decomposition of organic pollutants, non-toxicity, biological and chemical inertness, photochemical stability, inexpensive,

strong resistance to corrosion, etc. [50, 51]. However, despite the potential of TiO₂ as photocatalyst, there are two limitations in its application. The first is that TiO₂ is not photoactive under visible light due to its wide band gap (3.2 eV) [52 - 54]; the second is the fast recombination rate of electron-hole pairs that decreases the efficiency of photocatalytic reactions [50, 55].

A possible solution for these limitations is the doping with various species such as graphene [56 - 59]. Graphene is an ideal nanomaterial for doping TiO₂ thanks to its large specific surface area, to its high electrical and thermal conductivity, to its high chemical stability, to its high transparency and to the formation of Ti-O-C bonds that extend the visible light absorption of TiO₂ [60 - 63]. Furthermore, electrons are easily transported from TiO₂ to graphene sheets and the electron-hole recombination is considerably reduced, enhancing the photocatalytic efficiency [56]. Thus, it has been reported that graphene based semiconductor nanocomposites are considered as good photocatalyst for pollutant degradation [58].

Another process in which the potential of solar light is used to disinfect drinking water from chemical and microbial contaminants is Solar Disinfection (SODIS) [64]. This process exploit the ability of solar light to kill pathogens through genome damages and intracellular oxidative reactions [65] and can be enhanced by the addition of various chemicals [64, 66]. In the SODIS context, processes like AOPs produce a great potential. A widely studied AOP in this field is the photo-Fenton process in which OH radicals are generated using light, iron and hydrogen peroxide and act as oxidant species in water treatment [67, 68]. Particularly, photo-Fenton system involves reactions of H₂O₂ with Fe^{2+} ions leading to the formation of Reactive Oxygen Species (ROS) and reactive radical species, like OH radicals and other less reactive radicals, that are highly oxidant species for the inactivation of bacteria and viruses [69]. Water sources contain a large amount of inorganic ions naturally present or introduced in natural cycles by agricultural, domestic and industrial activities. These compounds could lead to OH radicals generation or could have a scavenging effect on OH radicals; to this aim, depending on their concentrations, SODIS and photo-Fenton processes are inhibited or promoted in varying degrees by inorganic ions [70].

References

[1] I. V. Muralikrishna and V. Manickam, *Environmental Management*, BSP books Pvt Ltd, Elsevier Inc., 2017, ISBN 978-0-12-811989-1.

[2] C. J. Nobles, E. F. Schisterman, S. Ha, K. Kim, S. L. Mumford, G. M. Buck Louis, Z. Chen, D. Liu, S. Sherman and P. Mendola, *Environ. Res.*, 2018, 163, 228–236.

[3] Z. Wu, X. Guo, C. Lv, H. Wang, D. Di, *Ecol. Indic.*, 2018, 92, 189–194.

[4] Y. Chae and Y. J. An, *Environ. Pollut.*, 2018, 240, 387–395.

[5] N. Auger, M. Duplaix, M. Bilodeau-Bertrand, E. Lo and A. Smargiassi, *Environ. Pollut.*, 2018, 239, 599–606.

[6] J. Ngarambe, H. S. Lim and G. Kim, *Sustain. Cities. Soc.*, 2018, 42, 337–343.

[7] J. J. Peirce, F. R. Weiner, P. A. Vesilind, *Environmental Pollution and Control*, Elsevier, 1998, ISBN: 978-0-7506-9899-3.

[8] R. Andreozzi, V. Caprio, A. Insola, R. Marotta, *Catal. Today*, 1999, 53, 51–59.

[9] M. A. Shannon, P. W. Bohn, M. Elimelech, J. G. Georgiadis, B. J. Mariñas and A. M. Mayes, *Nature*, 2008, 452, 301–310.

[10] D. H. Kumar Reddy and S.M. Lee, *J. Environ. Anal. Toxicol.*, 2012, 2, 5.

[11] R. P Schwarzenbach, B. I Escher, K. Fenner, T. B. Hofstetter, C. A. Johnson, U. von Gunten and B. Wehrli, *Science*, 2006, 313, 1072–1077.

[12] A. Agrawal, R. S. Pandey and B. Sharma, *J. Water Res. Prot.*, 2010, 2, 432-448.

[13] M. M. Haque, D. Bahnemann and M. Muneer, *Photocatalytic Degradation of Organic Pollutants: Mechanisms and Kinetics*, InTech, 2012, ISBN 978-953-307-917-2.

[14] M. B. Ahmed, J. L. Zhou, H. H.Ngo, W. Guo, N, S. Thomaidis a,d J. Xu, *J. Hazard. Mater.*, 2017, 323, 274–298.

[15] P. R. Gogate, A. B. Pandit, *Adv. Environ. Res.*, 2004, 8, 501–551.

[16] I. Oller, S. Malato, J. A. Sánchez-Pérez, *Sci. Total. Environ.*, 2011, 409, 4141–4166.

[17] C. Guillard, H. Lachheb, A. Houas, M. Ksibi, E. Elaloui and J. M. Herrmann, *J. Photochem. Photobiol. A: Chem.*, 2003, 158, 27-36.

[18] C. M. The and A. R. Mohamed, *J. Alloys Compd.*, 2011, 509, 1648–1660.

[19] R. Kant, *Natural Sci.*, 2012, 4, 22-26.

[20] Y. M. Slokar and A. M. Le Marechal., *Dyes Pigments.*, 1998, 37, 335–356.

[21] C. Burgess and O. Thomas, *Techniques And Instrumentation In Analytical Chemistry*, Elsevier, 2007, 27, ISBN: 13: 978-0-444-53092-9.

[22] E. N. Abrahart, *Dyes and their Intermediates*, Chemical Publishing, 1977, ISBN: 13: 978-0-713-12580-1.

[23] T. Kodom, E. Amouzou, G. Djaneye-Boundjoua and L. M. Bawa, *Intern. J. Chem. Tech.*, 2012, 4, 45-56.

[24] K. R. Raghavendra and K. Ajay Kumar, *Int. J. ChemTech Res.*, 2013, 5, 1756, 1760.

[25] Y. Zhang, W. Hou and Y. Tan, *Dyes Pigments.*, 1997, 34, 25–35.

[26] H. Paul, A. J. Reginato and H. R. Schumacher, *Arthritis Rheum.*, 1983, 26, 191-200.

[27] A. D. Proia and N. T.Brinn, *Arch. Pathol. Lab. Med.*, 1985, 109,186-189.

[28] E. I. Unuabonah, C. G. Ugwuja, M. O. Omorogie, A. Adewuyi and N. A. Oladoja, *Appl. Clay. Sci.*, 2018, 151, 211–223.

[29] K. K. Jyoti and A. B. Pandit, *Biochem. Eng. J.*, 2001, 7, 201–212.

[30] C. Liu, X. Xie, W. Zhao, N. Liu, P. A. Maraccini, L. M. Sassoubre, A. B. Boehm and Y. Cui, *Nano Lett.*, 2013, 13, 4288–4293.

[31] X. Ma, W. Zhou, Z. Fu, Y. Cheng, M. Min, Y. Liu, Y. Zhang, P. Chen and R. Ruan, *Bioresour. Technol.*, 2014, 167, 8–13.

[32] S. A. Bradford, V. L. Morales, W. Zhang, R. W. Harvey, A. I. Packman, A. Mohanram and C. Welty, *Crit. Rev. Environ. Sci. Technol.*, 2013, 43, 775–893.

[33] C. Ferguson, A. M. R. Husman, N. Altavilla, D. Deere and N. Ashbolt, *Crit. Rev. Environ. Sci. Technol.*, 2013, 33, 299–361.

[34] C. M. Villanueva, K. P. Cantor, J. O. Grimalt, N. Malats, D. Silverman, A. Tardon, R. Garcia-Closas, C. Serra, A. Carrato, G. Castaño-Vinyals, R. Marcos, N. Rothman, F. X. Real, M. Dosemeci, and M. Kogevinas, *Am. J. Epidemiol.*, 2007, 165, 148–156.

[35] T. J. Beveridge, *Bacteria in Nature*, Springer, 1989, 3. ISBN: 978-1-4613-0803-4

[36] K. D. Young, *Microbiol. Mol. Biol. Rev.*, 2006, 70, 660–703.

[37] J. H. Ramirez, M. A. Vicente, L. M. Madeira, *Appl Catal B. Environ.*, 2010, 98, 10–26.

[38] P. R. Gogate, A. B. Pandit, *Adv. Environ. Res.*, 2004, 8, 501–551.

[39] I. Oller, S. Malato, J. A. Sánchez-Pérez, *Sci. Total. Environ.*, 2011, 409, 4141–4166.

[40] Y. Deng, R. Zhao, *Curr Pollution Rep.*, 2015, 1, 167–176.

[41] R. B. M. Bergamini, E. B. Azevedo, L. R. Raddi de Araujo, *Chem. Eng. J.*, 2009, 149, 212–220.

[42] J. Kochany, J. R. Bolton, *Environ. Sci. Technol.*, 1992, 26, 262–265.

[43] H. Al-Ekabi, D. F. Ollis, *Photocatalytic Purification and Treatment of Water and Air*, Elsevier, 1993, ISBN: 978-0-4448-9855-5.

[44] F. Haber and J. Weiss, *Proc. R. Soc. Lond.*, 1934, 147, 332.

[45] J. Kiwi, C. Pulgarin, P. Peringer and M. Gratzel, *Appl. Catal. B: Environ.*, 1993, 3, 85.

[46] C. Pulgarin and J. Kiwi, *Chimia*, 1996, 50, 50.

[47] M. R. Hoffmann, S. T. Martin, W. Choi, D. W. Bahneman, *Chem. Rev.*, 1995, 95, 69–96.

[48] S. Kalathil, M. M. Khan, S. A. Ansari, J. Lee, M. H. Cho, *Nanoscale*, 2013, 5, 6323–6326.

[49] R. Asahi, T. Morikawa, T. Ohwaki, K. Aoki, Y. Taga, *Science*, 2001, 293, 269–271.

[50] K. Hashimoto, H. Irie, A. Fujishima, *Jpn. J. Appl. Phys.*, 2005, 12, 8269–8285.

[51] M. M. Khan, S. A. Ansari, D. Pradhan, M. O. Ansari, D. H. Han, J. Lee, M. H. Cho, *J. Mater. Chem. A*, 2014, 2, 637–644.

[52] V. Iliev, D. Tomova, L. Bilyarska, G. Tyuliev, *J. Mol. Catal. A-Chem.*, 2007, 263, 32–38.

[53] A. Mills, C. O'Rourke, K. Moore, *J. Photoch. Photobio. A,* 2015, 310, 66–105.

[54] A. Truppi, F. Petronella, T. Placido, M. Striccoli, A. Agostiano, M. L. Curri, R. Comparelli, *Catalysts,* 2017, 7, 100.

[55] W. Qian, P. A. Greaney, S. Fowler, S. K. Chiu, A. M. Goforth, J. Jiao, *ACS Sustainable Chem. Eng.,* 2014, 2, 1802−1810.

[56] H. Zhang, X. Lv, Y. Li, Y. Wang, J. Li, *ACS Nano*, 2010, 4, 380–386.

[57] D. Zhao, G. Sheng, C. Chen, X. Wang, *Appl. Catal. B,* 2012, 111–112, 303–308.

[58] N. R. Khalid, E. Ahmed, Z. Hong, L. Sana, M. Ahmed, *Curr. Appl. Phys.*, 2013, 13, 659–663.

[59] Y. Gu, M. Xing, J. Zhang, *Appl. Surf. Sci.*, 2014, 319, 8–15.

[60] C. Lee, X. Wei, J. W. Kysar, J. Hone, *Science*, 2008, 321, 385–388.

[61] M. D. Stoller, S. Park, Y. Zhu, J. An, R. S. Ruoff, *Nano Lett.*, 2008, 8, 3498–3502.

[62] K. S. Novoselov, A. K. Geim, S. V. Morozov, D. Jiang, Y. Zhang, S. V. Dubonos, I. V. Grigorieva, A. A. Firsov, *Science*, 2004, 306, 666–669.

[63] A. A. Balandin, S. Ghosh, W. Bao, I. Calizo, D. Teweldebrhan, F. Miao, C. N. Lau, *Nano Lett.*, 2008, 8, 902–907.

[64] K. G. McGuigan, R. M. Conroy, H. J. Mosler, M. du Preez, E. Ubomba-Jaswa, P.Fernandez-Ibanez, *J. Hazard. Mater.*, 2012, 235–236, 29–46.

[65] S. Giannakis, *Environ. Sci. Pollut.,* 2018, 1–17.

[66] S. Kehoe, T. Joyce, P. Ibrahim, J. Gillespie, R. Shahar, K. McGuigan, *Water Res.*, 2001, 35, 1061–1065.

[67] S. Giannakis, M. I. Polo Lòpez, D. Spuhler, J. A. Sànchez Pèrez, P. Fernàndez Ibànez, C. Pulgarin, *Appl. Catal. B Environ.*, 2016, 199, 199–223.

[68]S. Giannakis, M. I. Polo Lòpez, D. Spuhler, J. A. Sànchez Pèrez, P. Fernàndez Ibànez, C. Pulgarin, *Appl. Catal. B Environ.*, 2016, 198, 431–446.

[69] G. Ruppert, R. Bauer, G. Heisler, *J. Photochem. Photobiol., A: Chem.*, 1993, 73, 75–18.

[70] J. Ndounla, C. Pulgarin, *Environ. Sci. Poll. Res.*, 2015, 22, 17082–17094.

SECTION 1

GRAPHENE BASED TiO$_2$ NANOCOMPOSITES FOR PHOTOCATALYTIC DEGRADATION OF SYNTHETIC DYES

CHAPTER 2. INTRODUCTION

One of the biggest problems that the world is facing today is environmental pollution, which increases every year and causes serious and irreparable damage to the Earth [1]. Therefore, environmental protection and a new approach in environmental remediation are important factors for a real improvement in quality of life and for sustainable development.

Due to the industrialization and the lack of effective treatments of effluents at the source, a severe deterioration of freshwater resources caused by the release of a wide range of hazardous substances into water bodies occurred. Synthetic dyes represent a large part of these substances and deserve particular attention due to the high amounts (more than 800,000 tons) that are produced annually worldwide [2]. Approximately, one third of these substances is released into receiving waters every year through industrial wastewater discharges [3] determining a severe influence on both the environment and human health, affecting photosynthetic activity as well as dissolved oxygen concentration and causing serious ecologic problems [4]. Taking into account these considerations, there is an urgent need to develop new methods for the treatment of industrial wastewater containing synthetic dyes.

In recent years, photocatalysis based on the use of semiconductor material as photocatalyst has been used for environmental remediation; the photocatalyst present different properties as versatile, low-cost, environmentally friendly treatment technology for many pollutants [5, 6], and the use of heterogeneous photocatalysis is an emerging application in water decontamination.

A semiconductor (SC) material is characterized by an electronic band structure in which the lowest occupied energy band, called valence band (VB), and the highest empty band, called conduction band (CB), are separated by a band gap with a value in the range between 1 and 4 eV [7]. In particular, a material is classified as semiconductor when the band gap energy is less than 3 eV, while it is classified as wide band gap semiconductor when its band gap energy value is the range between 3 and 4 eV [7], as in the case of TiO_2. Semiconductors used for the photocatalytic degradation are usually metal oxides or metal sulfides; the most common and their respective band structures are shown in Figure 2.1 [8].
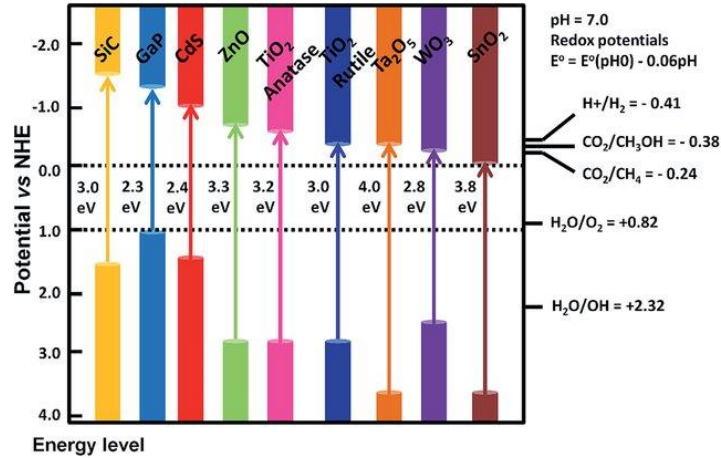
Figure 2.1: *Band gap and band edge positions of a range of semiconductors vs. NHE [8].*

Semiconductor based photocatalysis starts with the activation of SC by solar light or artificial light; when the SC is irradiated with photons whose energy is higher or equal to its band gap energy, a promotion of an electron from the VB to the CB occurs with the concomitant generation of a hole in the VB [9].

In a water system, oxygen adsorbed on the surface of the semiconductor acts as electron acceptor, while the adsorbed water molecules and hydroxyl anions act as electron donors, leading to the formation of a very powerful oxidizing hydroxyl (OH) radicals. Successively, the electron presents in the CB after the irradiation, react with oxygen molecule to form the superoxide (O_2^-) radical anion. When is present an organic molecule (M) adsorbed on the semiconductor surface, the OH radical is the primary oxidant and with the O_2^- radical, start the oxidation of the organic compound. The reaction catalysed by these radicals product adducts, followed by the fragmentation of the molecular structure into several intermediates species until the total mineralization of contaminant that is completed with the formation of CO_2 and H_2O. [10 - 12].

The successful of photocatalytic process is strictly dependent on the competition between the reaction of the electron with water on the semiconductor surface and the electron-hole recombination process that releases heat or radiation. The overall process can be described by following reactions (Equations 2.1–2.6):

$$SC + hv \ \rightarrow SC(e_{CB}^- + h_{VB}^+) \tag{2.1}$$

$$SC(h_{VB}^+) + H_2O_{ads} \ \rightarrow SC + \cdot OH_{ads} + H_{ads}^+ \tag{2.2}$$

$$SC(e_{CB}^-) + O_{2ads} \ \rightarrow SC + O_{2ads}^{-\cdot} \tag{2.3}$$

$$SC(h_{VB}^+) + M_{ads} \rightarrow SC + M_{ads}^{+\cdot} \qquad\qquad (2.4)$$

$$(\cdot OH_{ads} \ and/or \ O_{2ads}^{-\cdot}) + M_{ads} \rightarrow intermediate \ products \rightarrow CO_2 + H_2O \qquad (2.5)$$

$$e_{CB}^- + h_{VB}^+ \rightarrow N + E \qquad\qquad\qquad \text{N=Neutral Centre} \qquad\qquad (2.6)$$
$$\text{E=Energy (heat or radiation)}$$
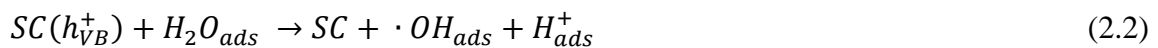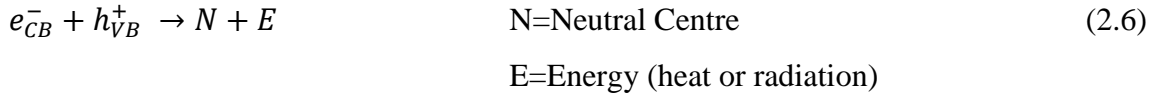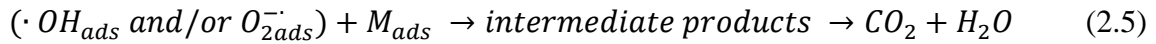
Within a great number of oxide semiconductors, TiO_2 is the most widely used as promising photocatalyst, demonstrating a very important role in environmental remediation [13, 14], solar energy [15], and other fields [16, 17] due to its non-toxicity, low cost, corrosion resistance, abundant resources and high photocatalytic efficiency [18 - 20].

A high number of studies concerning TiO_2 regard wastewater treatments [21 - 24] and, in many cases, total mineralization of pollutants without any waste disposal problem have been published [25]. On the other hand, the practical applications of this technique are limited to a narrow excitation wavelength because of TiO_2 large band gap energy (3.2 eV, see paragraph 2.1), high recombination rate of the photo produced electron–hole pair, and poor adsorption capacity [26 - 28]. For these reasons, in recent years, various attempts have been applied to improve the catalytic efficiency of TiO_2 [21, 29, 30].

Due to its wide band-gap, TiO_2 is active only under UV-light irradiation; considering that the percentage of UV-light is less than 5% of the total incident solar spectrum on the Earth, in recent years research has focused on extending the light absorption of TiO_2 under visible light. The research goal of TiO_2 photocatalysis, as for other semiconductors, is represented by the combination of TiO_2 with other nanomaterials to achieve both visible light activation and adsorption capacity improvement, with the simultaneous limitation of the electron-hole recombination rate. For this reason, to improve the photocatalytic performances of TiO_2 photocatalysis, different approaches have been investigated, such as the use of co-catalysts and loading with noble metal particles, dye, metallic or non-metallic doping [31 - 39]. Recently, enhancements of the photocatalytic activity of TiO_2 by visible light have been also demonstrated by the modification of TiO_2 with carbonaceous substances such as fullerenes, carbon nanotubes, and graphene to form carbon-TiO_2 composites [40 - 43].

In particular, graphene nanomaterials in combination with TiO_2 highlight new prospective in the field of photocatalysis for their large specific surface area, flexible structure, extraordinary mobility of charge carriers at room temperature, high thermal and electrical conductivities and high chemical stability [44 - 51]. Because of its properties, graphene-TiO_2 nanocomposites emerging as one of the

most promising materials for enhancing the photocatalytic performance in the new generation of photocatalysts [52 - 59].

2.1. Titanium Dioxide: Concepts and Properties

Titanium dioxide (TiO_2) is one of the most useful material for photocatalytic purposes, owing to its exceptional optical and electronic features, its biological and chemical stability, non-toxicity, low cost and high efficiency for the decomposition of organic pollutants [60, 61].

TiO_2 exists in three different polymorphs: Anatase, Rutile and Brookite, represented in Figure 2.2. These different crystalline forms exhibit different physical, chemical and catalytic properties [62, 63]. The crystal systems of Rutile and Anatase are tetragonal, while Brookite is orthorhombic. The stable form of TiO_2 is Rutile, whereas Anatase and Brookite are metastable and are quickly transformed to Rutile with temperatures exceeding 600 °C [64].
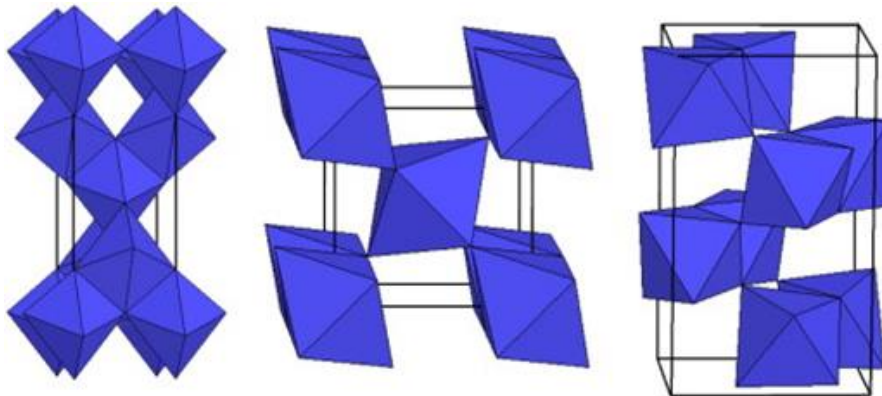
Figure 2.2: *TiO$_2$ polymorphism. From right Anatase, Rutile and Brookite [63].*

The crystal structure of TiO_2 polymorphs can be explained by different spatial arrangements of TiO_6 octahedra; differences between the three structures are due to the various degrees of distortion and 3D assembly of the TiO_6 octahedra [65]. In the Anatase crystal structure each octahedron shares corners to form (0 0 1) planes, the Rutile crystal structure consists of edge sharing octahedrons forming the (0 0 1) planes, while the orthorhombic structure of Brookite phase is made up of both corner and edge sharing octahedra [65]. Anatase crystals are too small and the range of natural colour goes from blue sapphire to yellow-brown, Rutile crystals can be found in nature as black or reddish and transparent when completely without impurities and Brookite structure forms very flat small

tubular crystals with a colour from yellow to brown reddish [64]. These different crystal structures result in various densities and electronic structures of the three TiO_2 polymorphs as reported in Figure 2.3 [65].
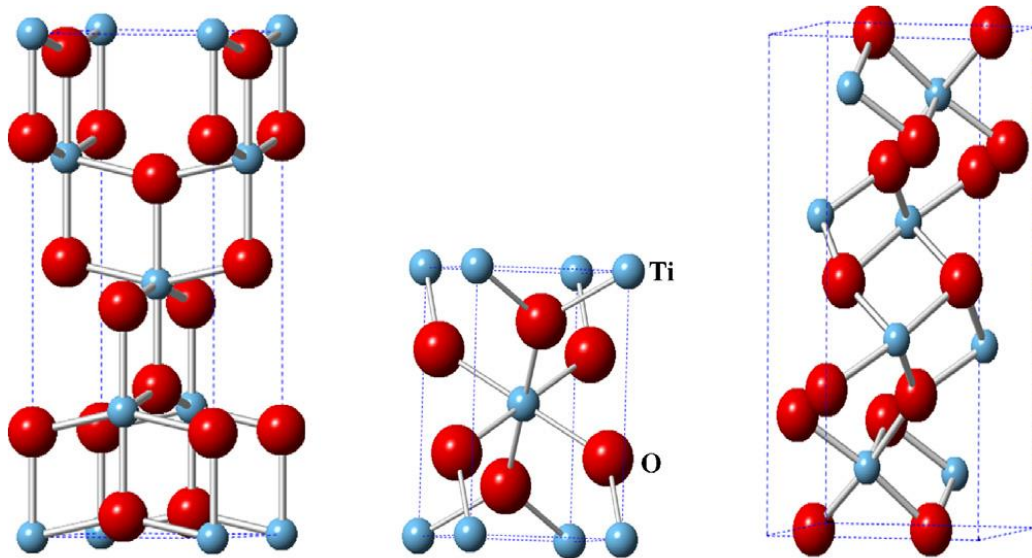
Figure 2.3: *Crystalline structures. From right Anatase, Rutile and Brookite [65].*

Anatase, Rutile and Brookite forms are characterized by high band gap, respectively equal to 3.2 eV, 3.0 eV and 3.4 eV allowing to utilize only radiations with a wavelength lower than 400 nm, which represents about 5% of solar radiation [66 - 68]. Although the band gap energy values of Anatase, Rutile and Brookite are very close to each other, Anatase form presents the higher activity in terms of photocatalytic efficiency due to the easier and favourable electron transfer that occurred into its conduction band [69].

One of the most used commercial TiO_2 materials for photocatalytic applications is Aeroxide P-25, which consists of a mixture of Anatase and Rutile forms in a ratio of about 80:20 [70]. It is not yet well known the exact crystalline composition of Aeroxide P-25, but it has a relatively large surface area of about 50 m^2/g [71]. In particular, Aeroxide P-25 is a titanium photocatalyst widely used because its efficiency is relatively higher in several photocatalytic reaction systems [71]. The higher efficiency in terms of photocatalytic activity of Aeroxide P-25 can be attributed to the presence of Anatase and Rutile forms because the transfer of electron-hole pairs between interconnecting Anatase and Rutile particles can improve charge separation and thus improve efficiency of electron-hole pairs [72].

2.2. Fundamentals of TiO₂ Photocatalysis

In TiO₂ photocatalytic process, the electron-hole pairs are generated when aqueous TiO₂ suspension is irradiated with light energy greater than its band gap of 3.2 eV. Photogenerated electrons can reduce organic compounds or react with electron acceptors such as O₂ adsorbed on the semiconductor surface or dissolved in water, reducing it to O_2^- radicals. Photogenerated holes can oxidize the organic molecule or react with H₂O or OH^- oxidizing them into OH radicals. The radical species are responsible for the TiO₂ photodecomposition of organic substrates (e.g. dyes) [69], as shown in Figure 2.4.
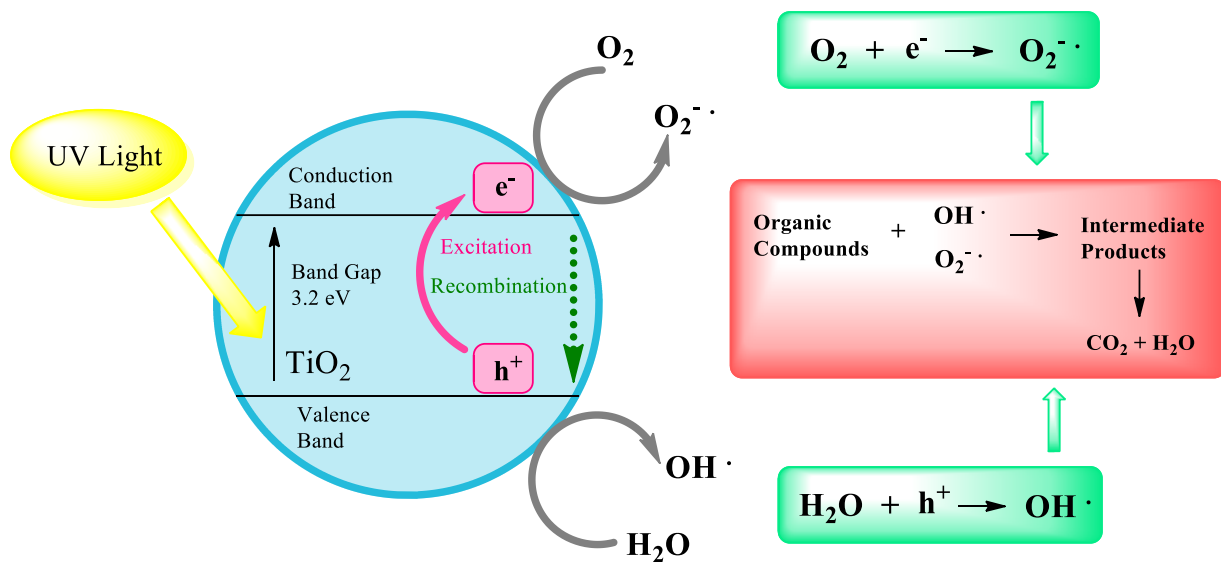
Figure 2.4: *TiO₂ photocatalytic process under UV light irradiation.*

The reactions at the semiconductor surface that cause the degradation of organic compounds can be expressed as follows (Equations 2.7–2.11) [69]:

$$TiO_2 + hv(UV) \rightarrow TiO_2(e_{CB}^- + h_{VB}^+) \tag{2.7}$$

$$TiO_2(h_{VB}^+) + H_2O \rightarrow TiO_2 + H^+ + OH \cdot \tag{2.8}$$

$$TiO_2(h_{VB}^+) + OH^- \rightarrow TiO_2 + OH \cdot \tag{2.9}$$

$$TiO_2(e_{CB}^-) + O_2 \rightarrow TiO_2 + O_2^{-\cdot} \tag{2.10}$$

$$O_2^{-\cdot} + H^+ \rightarrow HO_2 \cdot \hspace{6cm} (2.11)$$

The resulting OH radicals, being a very strong oxidizing agents with a standard redox potential of 2.8 V [73], can oxidize most of organic compounds like dyes until the final mineralized products (Equations 2.12–2.14) [74].

$$OH \cdot + Dye \rightarrow Degradation\ Products \hspace{4cm} (2.12)$$

$$h_{VB}^+ + Dye \rightarrow Oxidation\ Products \hspace{4cm} (2.13)$$

$$e_{CB}^- + Dye \rightarrow Reduction\ Products \hspace{4cm} (2.14)$$

The mechanism of photosensitized oxidation by visible radiation ($\lambda > 420$ nm) is different from the UV light radiation pathway. Indeed, the visible light mechanism, reported in Figure 2.5, suggests that excitation of the adsorbed dye takes place by visible light to appropriate singlet or triplet states, subsequently followed by electron injection from the excited dye molecule onto the conduction band of the TiO$_2$ particles, whereas the dye is converted to the cationic dye radicals that undergoes degradation to yield products as follows (Equations 2.15–2.20) [74 - 76]:

$$Dye + hv(Vis) \rightarrow Dye^* \hspace{5cm} (2.15)$$

$$Dye^* + TiO_2 \rightarrow Dye^{+\cdot} + TiO_2(e_{CB}^-) \hspace{3.5cm} (2.16)$$

$$TiO_2(e_{CB}^-) + O_2 \rightarrow TiO_2 + O_2^{-\cdot} \hspace{4cm} (2.17)$$

$$O_2^{-\cdot} + e_{CB}^- + 2H^+ \rightarrow H_2O_2 \hspace{4.5cm} (2.18)$$

$$H_2O_2 + e_{CB}^- \rightarrow OH \cdot + OH^- \hspace{4.5cm} (2.19)$$

$$Dye^{+\cdot} + (OH \cdot and/or\ O_2^{-\cdot}) \rightarrow Peroxide\ or\ Hydroxyl\ Intermediates \rightarrow$$
$$Mineralized\ Products \hspace{6cm} (2.20)$$
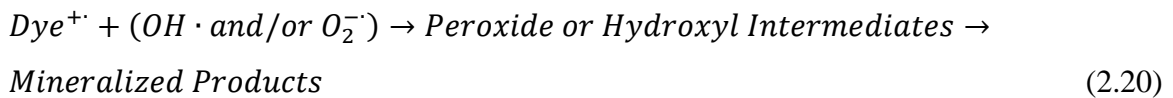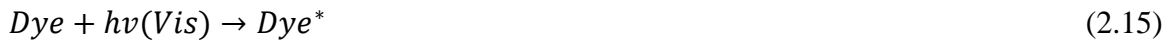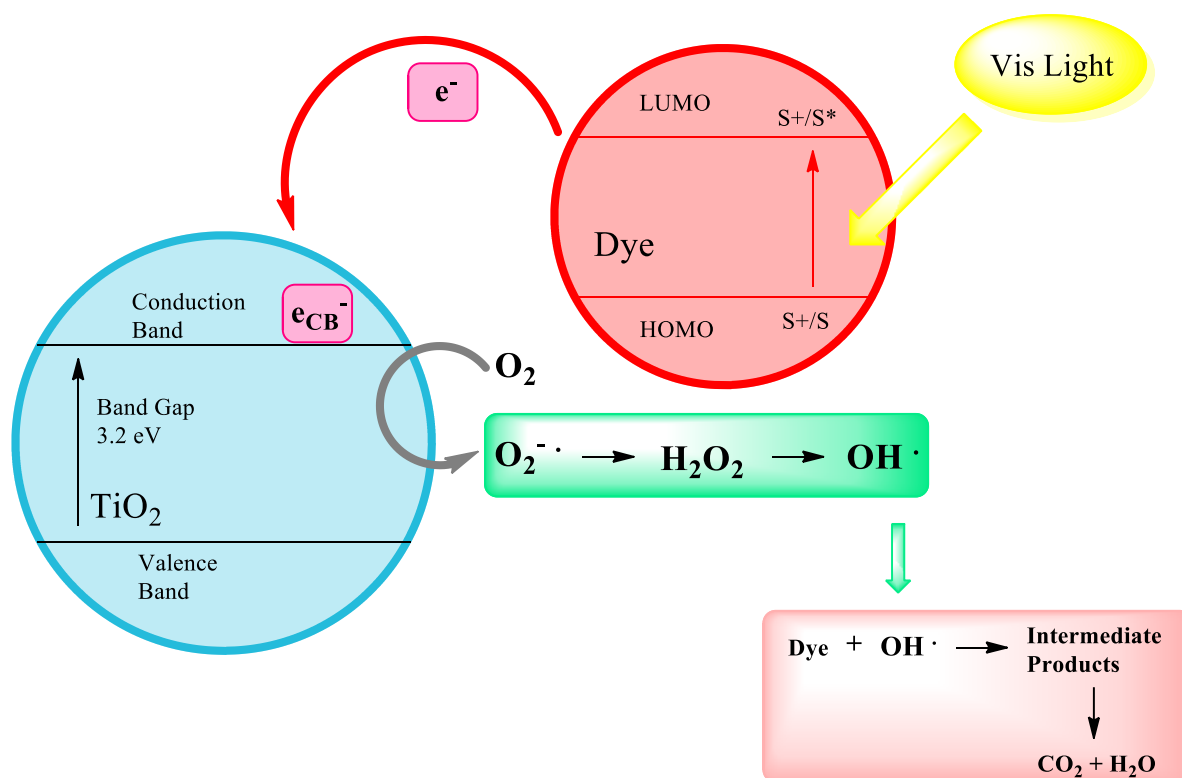
Figure 2.5: *Photocatalytic mechanism under visible light irradiation with dye adsorbed on TiO$_2$ surface.*

The electron-hole pair can recombine releasing the absorbed energy as heat [77] and this phenomenon negatively affects the photocatalytic reactions on semiconductor surface, reducing the efficiency of the overall process.

2.2.1. Factors Influencing the Photocatalytic Process

Photocatalytic degradation is a complex process involving several operational parameters that may affect the total efficiency of treatment. These parameters include physical and chemical properties of the photocatalyst, pH of the medium, reaction temperature, type of solvent and type of precursor, substrate concentration and light intensity [78]. The most important factors to consider are:

- **Particle size and catalyst loading:** Particle size is of primary importance in heterogeneous catalysis, because it is directly related to the efficiency of a photocatalyst through its specific surface area. The surface area of the catalyst is related to the concentration of active sites present on the catalyst surface. This effect can influence the photodegradation process because

the small size of nanoparticles provides a higher specific surface area [79]. In addition, initial rates of reaction are directly proportional to the mass of catalyst. However, many studies [74, 80 - 82] have noted that, above a certain amount, the reaction rate decreased and it became independent of the catalyst concentration. This limit corresponds to the availability of active sites on TiO_2 surface. The availability of active sites increased with the increase of catalyst loading, but there could be unfavourable light scattering and the light penetration into the solution decreased due to catalyst agglomeration. Indeed, part of the catalyst surface became unavailable for dye and photon absorption. The optimal concentration of TiO_2 depends on geometry, working conditions of the photo reactor and type of light sources in order to avoid excess catalyst and ensure total absorption of efficient photons [77].

- **Initial pollutants concentration:** The degradation rate of the photocatalysis is influenced by pollutant concentration up to a certain level, but its further increase beyond the allowed limit, leads to decrease the degradation kinetics of the process [83]. In fact, the degradation rate is affected by the formation of OH radical and by the adsorption equilibrium of reactants on TiO_2 surface; the reaction rate of OH radicals with other chemical species and intermediates generated during the process are significant on the degradation rate [84]. In the case of organic compounds, the degradation rate is due to the probability of OH radicals formation on the catalyst surface and its probability to react with organic molecule.

- **Solution pH:** the pH of solution affects the surface charge of the photocatalyst and the ionization or speciation of organic compounds. The pH is related to the surface speciation according to the following reactions (Equations 2.21 and 2.22) [85 - 87]:

$$TiOH + H^+ \rightarrow TiOH_2^+ \tag{2.21}$$

$$TiOH + OH^- \rightarrow TiO^- + H_2O \tag{2.22}$$
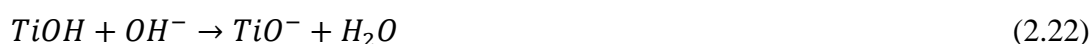
Under acidic or alkaline conditions, the surface of titanium can be protonated or deprotonated, respectively; as a result, pH changes can influence the adsorption of pollutant on the TiO_2 surface.

For instance, the adsorption study of Alizarin Red S (ARS) on TiO_2 surface positively charged through Equation 2.21, conducted at various pH [21] showed that the acidic condition gives the better adsorption efficiency. In fact, the acidic condition influences the chemistry of ARS structure, that shown negative charges on sulfonic and hydroxyl groups and an evident adsorption of ARS was observed as a result of the electrostatic attraction with TiO_2 photocatalyst; this behaviour is reported in Figure 2.6.
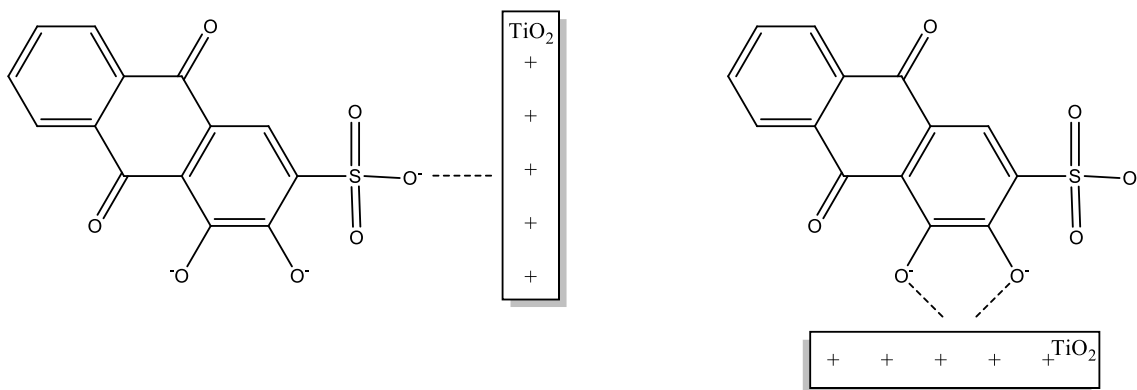
Figure 2.6: *Structural interaction between ARS and TiO$_2$ surface.*

2.2.2. Applications of TiO$_2$

TiO$_2$ is involved in a wide range of applications (Figure 2.7) like paints, coatings, plastics, paper, inks, fibres, foods, pharmaceuticals, cosmetics and biomedical purposes [61, 88 - 90].
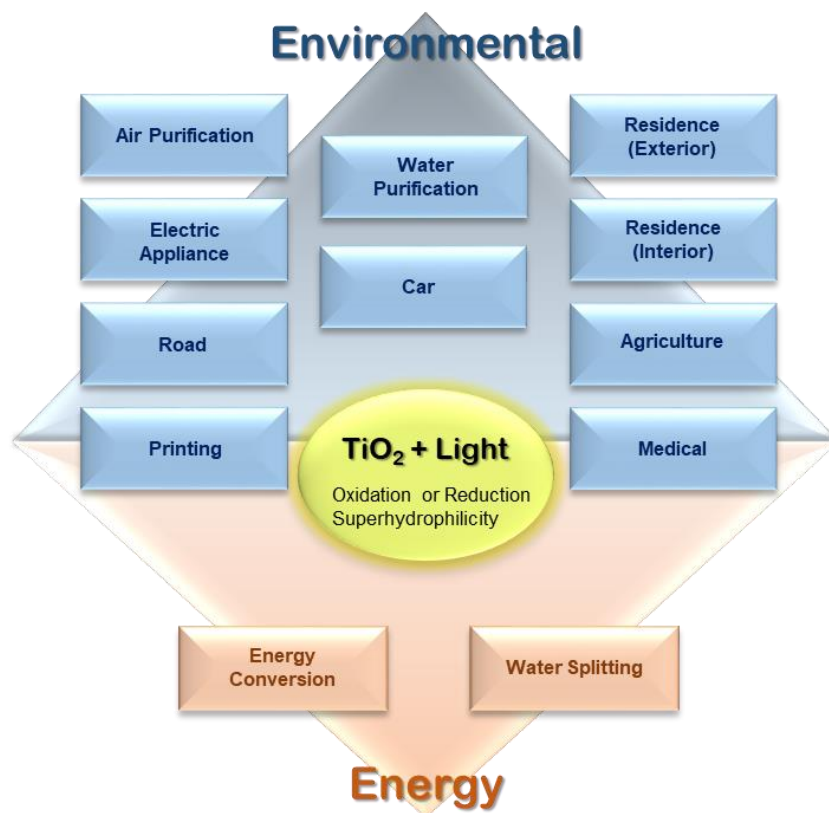
Figure 2.7: *Various applications of TiO$_2$ photocatalysis in environment and energy fields.*

Because of its high refractive index, the main use of TiO_2 is as white powder pigment; indeed a low level of TiO_2 is needed to achieve a white opaque coating that is resistant to discoloration under UV light radiation.

Because of the strong oxidative properties of TiO_2 under UV light, it is used for sterilizing, deodorizing and anti-fouling. Moreover, when irradiated with UV light, it becomes hydrophilic and can be used for anti-fogging coatings and self-cleaning windows, TiO_2 is also used as gas sensors [91, 92].

TiO_2 is considered as the most efficient and environmentally friendly photocatalyst, it is used for the photocatalytic water splitting; in fact, under UV light irradiation, water is photocatalytic converted to hydrogen gas using TiO_2 electrode [93, 94].

Finally, another significant application of TiO_2 in the field of energy conversion is its use in Dye-Sensitized Solar Cell (DSSC) that provide a low cost alternative to commercially available silicon based photovoltaic devices [95].

2.3. Graphene Materials: Concepts and Properties

Graphene is the term used to indicate carbon atoms tightly packed in a plane monolayer into a two-dimensional (2D) "honeycomb lattice" sp^2 hybridized that represents the building block for all graphitic materials such as 0D fullerenes, 1D nanotubes and 3D graphite [51], as shown in Figure 2.8. The IUPAC commission proposed the term "graphene" to substitute the older term "graphite layers", which was inappropriate in the research of 2D monolayers of carbon atoms because the 3D stacking structure is identified as "graphite" [96].
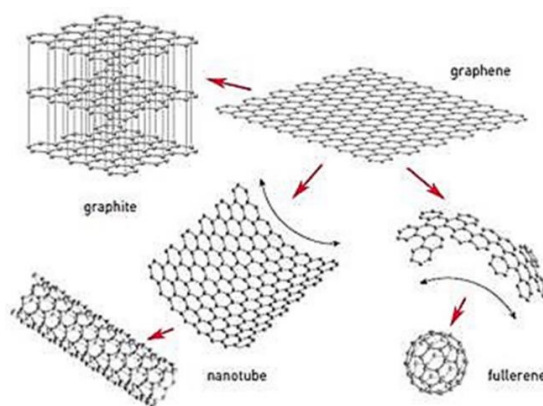
Figure 2.8: *Graphene and its derivatives.*

The isolation of graphene from graphite in 2003, by Prof. A. Geim and Prof. K. Novoselov, which was the first paper published in Science in 2004 [45] and was awarded the Nobel Prize in Physics in 2010, has fascinated and revolutionized the scientific community [45, 96]. This is due to graphene's notable properties and to the high range of applications that these properties offer to technologies such as energy storage and photocatalysis [97 - 103]. With its high electron mobility (about 200000 $cm^2 V^{-1} s^{-1}$), its large specific surface area, its high thermal conductivity (about 5000 W m^{-1} K^{-1}) and its mechanical strength (about 1 TPa), graphene is a powerful material [104, 105]. Indeed, graphene is a promising modifier for photocatalysts materials, due to its unique properties [106]. The zero band gap of graphene provides the condition for a perfect sensitizer; in fact, photoinduced electrons can be excited on the Fermi level of graphene by visible and infrared radiation. Moreover, its high electron mobility, due to delocalized conjugated π electron, is good for photocatalytic performances [107, 108]. Furthermore, its large specific surface area enhances photocatalysts adsorption ability of several pollutants [109] and its high electron mobility reduces the electron-hole pairs recombination [106].

2.3.1. Graphene Synthesis

From the first report on graphene, which was obtained manually by mechanical cleavage with a Scotch Tape sample of graphite, various techniques have been developed to produce thin graphitic films [58, 110, 111]. These can be divided into two main groups: bottom-up and top-down methods [58, 111], as schematized in Figure 2.9 [112].

In the bottom-up growth, the synthesis of graphene can be obtained via epitaxial growth [113, 114], chemical vapor deposition (CVD) [115, 116], electrochemical reduction of CO and CO_2 [117, 118], arc discharge [119, 120], unzipping carbon nanotubes [121, 122], organic synthesis [123], and pyrolysis [124, 125].

The top-down approach offers considerable economic advantages over bottom-up methods [126, 127], producing high quality graphene. In this case, the graphene is derived from the exfoliation of graphite, from mechanical [128, 129], electrochemical expansion [130, 131], thermal [132], electrostatic deposition [133], and chemical synthesis [134, 135].
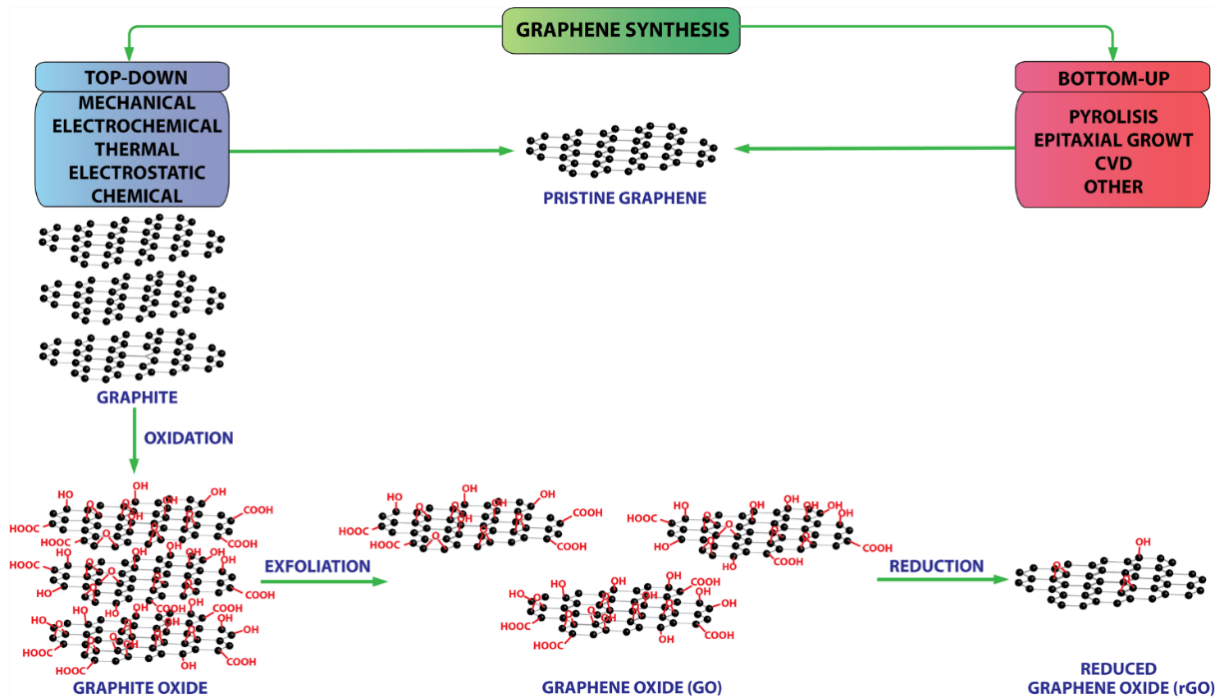
Figure 2.9: *Schematic graphene synthesis: top-down and bottom-up methods [112].*

Some other techniques are unzipping nanotube [136, 137] and microwave synthesis [138, 139], or by chemical and/or thermal graphene oxide reduction [140]. This last method allows the production of low-cost and large-scale graphene, though with oxygen-containing groups and defects [141, 142]. Much interest is directed at the study of proceedings to obtain graphene in the form of highly reduced graphene oxide [143, 144] or chemically modified graphene [145, 146] from the oxidation and exfoliation of graphite and successive chemical reduction.

The strong oxidation of graphite produces bulk solid graphite oxide that can be exfoliated in water or in other suitable organic solvents to form graphene oxide [147, 148]; several recent reviews report the synthesis of graphene oxide [149, 150], that can be prepared by Brodie [151], Staudenmaier [152] and Hummers [153] methods. The synthetic technique and the extent of the reaction influence the degree of graphite oxidation; the most oxidized graphite oxide is produced with the Staudenmaier method, but this reaction may take several days. However, because both Staudenmaier and Brodie methods generate highly toxic ClO_2 gas that can decompose in air violently, the most widely used method to prepare graphite oxide and successively graphene oxide is Hummers method.

With Hummers method, the graphene oxide is prepared by exfoliating graphite oxide obtained from the oxidation of graphite powder with strong chemical oxidants, such as HNO_3, $KMnO_4$ and H_2SO_4 [141, 142, 153]. Graphene oxide can be successively reduced to graphene by the partial restoration

of the sp2-hybridization by thermal [154], chemical [155], electrochemical [156], photo-thermal [157], photocatalytic [111, 158], sono-chemical [159, 160] and microwave reduction methods [161]. The high number of oxygen-containing groups of the obtained graphene oxide permits the interaction with cations, providing important reactive molecules for the nucleation and growth of nanoparticles and, therefore, the formation of various graphene-based composites.

2.4. Fundamentals of Graphene-TiO₂ Photocatalysis

The successful of photocatalytic process is strictly dependent on the competition on the kinetics of charge carriers and redox reactions, therefore, the knowledge of electronic processes that occur at the level of the semiconductor surface are of great importance.

The photocatalytic activity is greatly limited by electron–hole recombination, and therefore several methods are used to increase the efficiency of charge carrier separation and therefore to improve the photocatalytic performance of the semiconductor photocatalyst [162 - 164]. In this context, the combination of graphene with the semiconductor photocatalyst represents an innovative strategy [58, 111, 165].

TiO_2 is generally considered the best semiconductor material that can be used as photocatalyst [21, 162, 166], showing almost all of the required properties for an efficient photocatalytic process, except for activity under visible light irradiation.

From these considerations, graphene-TiO₂ nanocomposites are widely used for photocatalytic applications, exploiting their potential in environmental applications.

The effective role of graphene in a photocatalytic event on graphene-TiO₂ nanocomposites has not been completely investigated or is not completely understood. In order to explain the possible mechanism, the light source (UV or visible light) and the presence/absence of dye molecules, or rather the presence of a compound able to absorb visible light, are fundamental.

When the target molecule does not adsorb light and is efficiently adsorbed on the photocatalyst surface:

1) UV light excitation of graphene-TiO₂ nanocomposites photogenerates the electron–hole pairs and the electrons are then injected into graphene due to its more positive Fermi level [167]. This process is favoured by the position of the work function of graphene that is −4.42 eV, with respect to the conduction band of TiO_2 that is located at −4.20 eV [168]; from this consideration, the

electron in the conduction band of TiO_2 is injected into graphene. Graphene scavenges photogenerated electrons by dissolved oxygen, facilitates the electron-hole pairs separation, reducing the recombination and, due to its high carrier mobility, accelerates the electron transport, enhancing the photocatalytic performances [165, 169].

2) When the operational mechanism takes place via visible light, the electron transfer of the photogenerated electron is promoted from the graphene photoexcited state and then delocalized to the TiO_2 surface. M.T Silva et al. indicated, in rGO photoluminescence study, that the photogenerated electrons under Vis or NIR laser can be transferred to the surface of TiO_2 with a consequent quenching of photoluminescence; also in this case, charge recombination is inhibited with a consequent increasing in photocatalytic activity under visible light [170]. It is important to know that the presence of graphene in graphene-TiO_2 photocatalyst produces a red shift in the absorption, reducing its band gap and thus extending the photoresponse to a longer wavelength [171]. The explanation of visible light activation in the graphene-TiO_2 composites is not clear, but it is possible to attribute this phenomenon to the sensitization of TiO_2 due to the presence of graphene [170, 172, 173]. In this case, in the visible light excitation of graphene-TiO_2 photocatalyst, graphene absorbs the light, and the photoexcited electrons in high energy graphene states are delocalized into the conduction band of the TiO_2 surface with the dissipation of excess energy due to electron vibrational interaction [174]; successively electrons react with oxygen, resulting in the formation of superoxide radicals. In Figure 2.10, the activation mechanisms of graphene-TiO_2 photocatalyst under UV and visible light are reported.
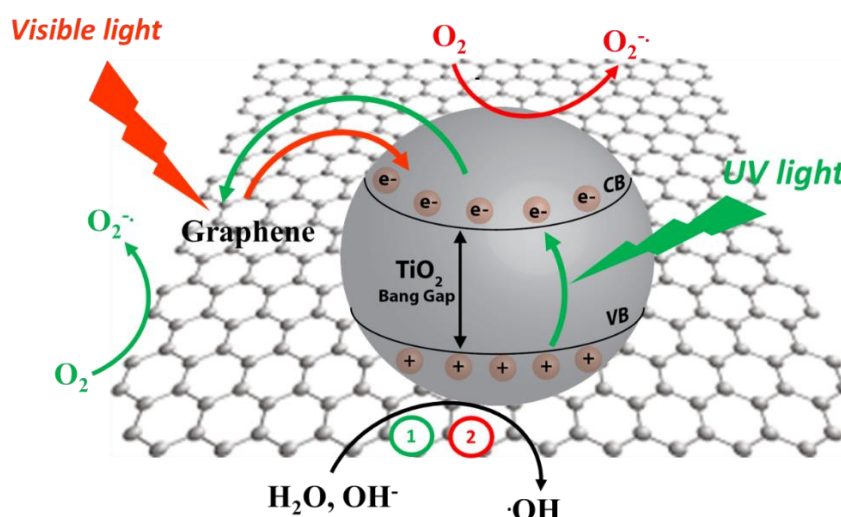
Figure 2.10: *Mechanisms of UV and visible light activation of graphene-TiO_2 photocatalyst [112].*

When a dye as a target molecule is efficiently adsorbed onto the photocatalyst surface, the UV mechanism is the same as that reported in the first case while, under visible light, different activation pathways can be found. In this case, the dye acts both as a sensitizer for visible-activation and as a pollutant during the photocatalytic process, promoting the electron transfer from the excited dye molecules state to the conduction band of TiO_2 while graphene acts as an electron scavenger, as in the UV mechanism [170]. The other possible pathway under visible light involves graphene that acts as visible light sensitizer promoting the electron transfer to the conduction band of TiO_2 (as in 2) [175 - 177] (Figure 2.11). This process is less probable due to the competition between graphene and dye as light sensitizers, but in any case, is possible.
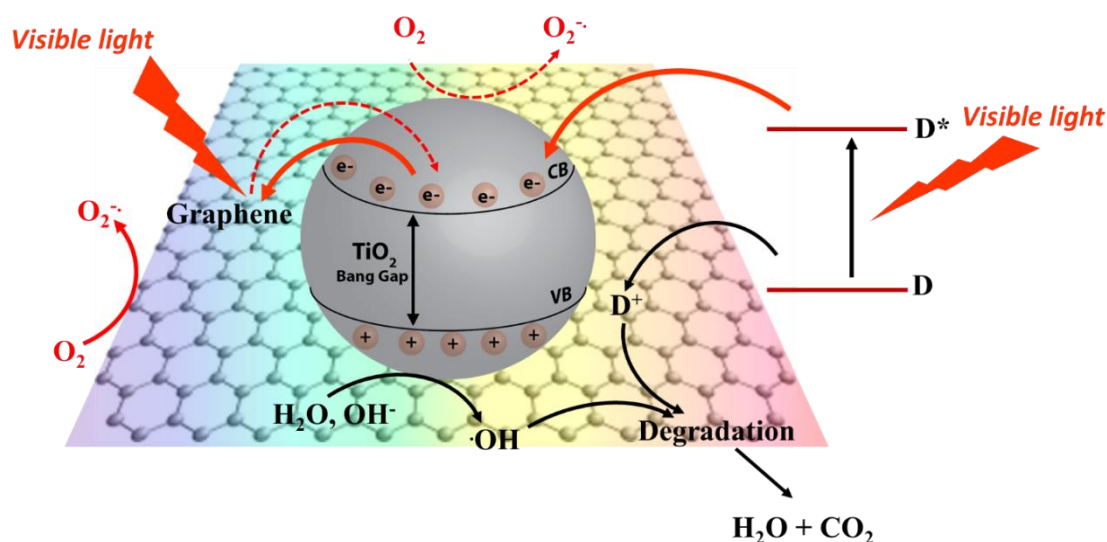
Figure 2.11: *Mechanisms of visible light activation of graphene-TiO₂ photocatalyst in the presence of dye [112].*

2.4.1. Preparation Methods of Graphene-TiO₂ Nanocomposites

The use of graphene in TiO_2 generally contributes to a bathochromic shift of the absorption band, hinders the recombination of electron-hole pairs by transferring the photoexcited electron into the graphene surface, which also enhances the surface area of TiO_2 for better absorptive properties [178], for these reasons, the investigation of graphene-TiO₂ photoactivity under visible light seems to be crucial. The improvement of performance due to the presence of graphene in graphene-TiO₂ photocatalyst is primarily attributed to the extension of the light absorption range, the increase of

absorptivity, and the efficient charge separation and transportation. With graphene-TiO_2 photocatalyst, the rate of electron-hole pairs recombination after light excitation decreases [179], while the charge transfer rate of electrons increases in addition to the surface-adsorption of chemical species thanks to π-π interactions [180].

However, the properties graphene-TiO_2 nanocomposites and different operational parameters, such as the characteristics of substrates, UV-Vis or Vis light irradiation, etc., can affect the photocatalytic efficiency [180].

Graphene-TiO_2 nanocomposites can be generally categorized into three kinds: TiO_2-mounted activated graphene [126], graphene-doped TiO_2, and graphene-coated TiO_2 [181] and each of these types exhibits good photocatalytic activity. In order to improve the efficiency, the surface properties of graphene could be adjusted via chemical modification, which facilitates its use in composite materials [182, 183].

Graphene-TiO_2 nanocomposites can be generally realized in two different ways by "ex situ hybridization" or "in situ crystallization". In Figure 2.11, a schematic representation of ex situ hybridization and in situ crystallization in the synthesis of graphene-TiO_2 nanocomposites is reported. Ex situ hybridization involves the mixing of graphene dispersions with pre-synthesized TiO_2 nanoparticles [170]. To enhance their solubility and improve the quality of graphene-TiO_2 composites, before mixing, TiO_2 nanoparticles and/or graphene sheets can be functionalized by covalent C–C coupling [94, 184] or non-covalent π-π stacking reactions [185]. However, with ex situ hybridization, in some cases it is possible to obtain a low-density and non-uniform coverage of nanostructures by graphene sheets [142, 186, 187].

The most common strategy to synthetize graphene-TiO_2 nanocomposites is represented by in situ crystallization. In this case, graphene oxide or reduced graphene oxide are usually used as starting materials for the presence of oxygen-containing functional groups on their surface. In fact, they act as a nucleation point for grooving and anchoring semiconductor nanocrystals. The successive reduction of graphene oxide generates graphene-TiO_2 nanocomposites with homogeneous distribution on 2D nanosheets, thereby promoting the direct interaction between semiconductor nanocrystals and graphene. For this reason, various methods, such as mixing, hydrothermal/solvothermal methods, sol-gel, electrochemical deposition, combustion, microwave, photo-assisted reduction, and self-assemble approaches, can be applied for the synthesis of graphene-TiO_2 nanocomposites [188, 189].
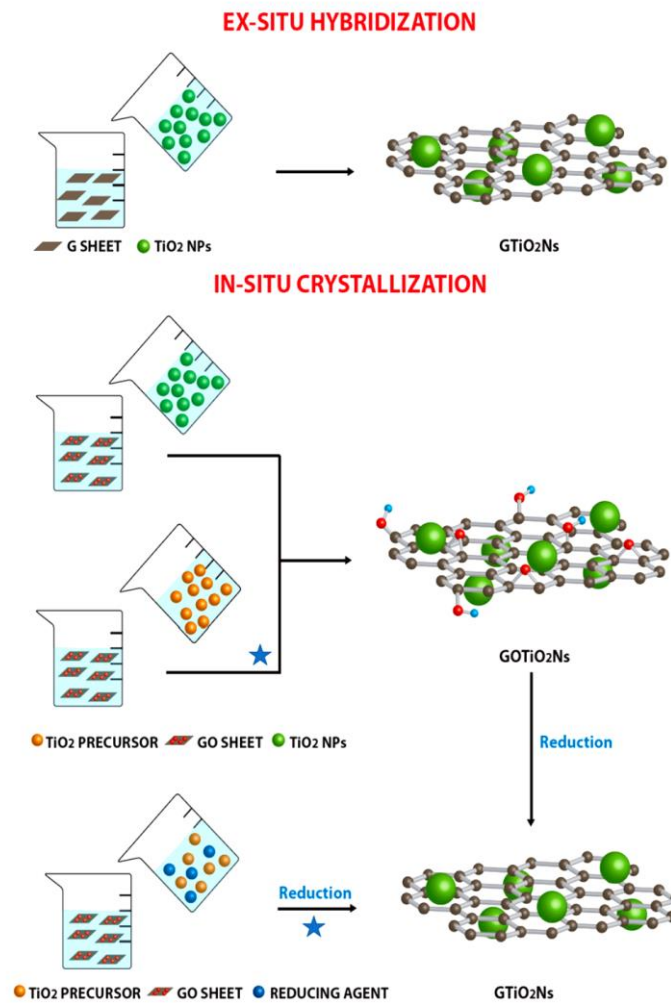
Figure 2.11: *Schematic representation of ex situ hybridization and*
in situ crystallization in the synthesis of graphene-TiO₂ [112].

2.4.2. Characterization Techniques of Graphene-Based Nanocomposites

Graphene characterization can be performed by various advanced instrumental techniques [190 - 192] classified in three categories, summarized in Figure 2.12 [193]:

- **Bulk and surface structure analysis**, carried out with Raman Spectroscopy, X-Ray Photoelectron Spectroscopy (XPS), Fourier Transform Infrared Spectroscopy (FT-IR), X-Ray Diffraction (XRD), X-ray Absorption Near Edge Structure (XANES), Atomic Force Microscopy (AFM), Scanning Electron Microscopy (SEM), Transmission Electron Microscopy (TEM), High-Resolution Transmission Electron Microscopy (HR-TEM),

Ultraviolet-Visible Spectroscopy (UV-Vis), Inductively Coupled Plasma Mass Spectrometry (ICP) and Thermogravimetric Analysis (TGA);

- **Chemisorptions ability determination**, carried out with Diffuse Reflectance Fourier Transform Infrared Spectroscopy (DRIFTS), Temperature Programmed Reduction (TPR) and CO chemisorption;

- **Reaction mechanism investigation**, carried out with Density Functional Theory Computations (DFT)
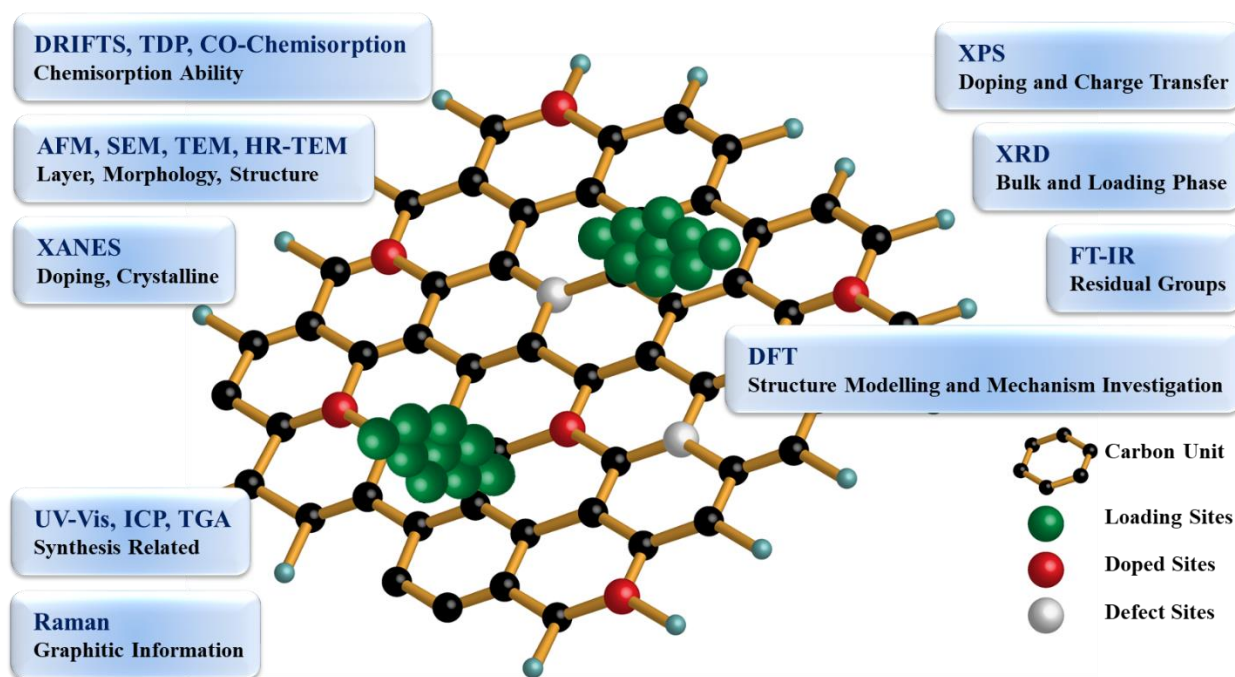
Figure 2.12: *Schematic representation of characterization techniques used in graphene-based nanocomposites characterization.*

Among all these characterization methods, Raman spectroscopy is the most useful for graphene and is used for the investigation of functional groups, surface area, number of layers and structural defects [193].

One of the best techniques used to study the surface, especially modified surface of graphene-based nanomaterials is XPS, while number of layers, crystallinity and size of graphene-based nanomaterials can be determined by XRD analysis [194].

The morphology and the presence of any chemical functionalities on graphene due to doping or to preparation methods can be detected by FT-IR, SEM, TEM, and AFM [194].

References

[1] J. J. Peirce, F. R. Weiner and P. A. Vesilind, *Environmental Pollution and Control*, Elsevier, 1998, ISBN: 978-0-7506-9899-3.

[2] N. Chaukura, C. Edna, E. C. Murimba and W. Gwenzi, Environ. Technol. Innov. 2017, 8, 132–140.

[3] M. Solís, A. Solís, H. Inés Pérez, N. Manjarrez and M. Flores, *Process. Biochem.* 2012, 47, 1723–1748.

[4] Z. Zhang, R. Y. Yang, Y. S. Gao, Y. F. Zhao, J. Y. Wang, L. Huang, J. Guo, T. T Zhou, P. Lu, Z. H. Guo et all. *Sci. Rep.* 2014, 4, 6797–6809.

[5] K. M. Cho, K. H. Kim, H. O. Choi and H. T. Jung, *Green Chem.*, 2015, 17, 3972–3978.

[6] A. O. Ibhadon and P. Fitzpatrick, *Catalysts*, 2013, 3, 189–218.

[7] V. Balzani, P. Ceroni and A. Juris, *Photochemistry and photophysics: concepts, research, applications*, Wiley-VCH, 2014, ISBN: 978-3-527-33479-7.

[8] P. Kumar, R. Boukherroub and K. Shankar, *J. Mater. Chem. A.*, 2018, 6, 12876–12931.

[9] A. Mills and S. Le Hunte, *J. Photochem. Photobiol. A.*, 1997, 108, 1–35.

[10] M. M. Mahlambi, C. J. Ngila and B. B. Mamba, *J. Nanomater.*, 2015, 2015, 790173.

[11] Y. Nosaka and A. Nosaka, *ACS Energy Lett.*, 2016, 1, 356–359.

[12] Y. Zhang, Y. Tan, H. L. Stormer and P. Kim, *Nature*, 2005, 438, 201–204.

[13] W. Wei, D. Liu, Z. Wei and Y. Zhu, *ACS Catal.*, 2017, 7, 652–663.

[14] W. J. Jiang, Y. F. Liu, J. Wang, M. Zhang, W. J. Luo and Y. F. Zhu, *Adv. Mater. Interfaces.*, 2016, 3, 9.

[15] T. Tatsuma, S. Saitoh, Y. Ohko and A. Fujishima, *Chem. Mater.*, 2001, 13, 2838–2842.

[16] C. P. Sajan, S. Wageh, A. A. Al-Ghamdi, J. G. Yu and S. W. Cao, *Nano Res.*, 2016, 9, 3–27.

[17] X. Chen and S. S. Mao, *Chem. Rev.*, 2007, 107, 2891–2959.

[18] H. Tong, S. X. Ouyang, Y. P. Bi, N. Umezawa, M. Oshikiri and J. H. Ye, *Adv. Mater.*, 2012, 24, 229–251.

[19] M. Anpo and M. Tackeuchi, *J. Catal.*, 2003, 216, 505–516.

[20] L. M. Al-Harbi, E. H. El-Mossalamy, H. M. Arafa, A. Al-Owais and M. A. Shah, *Mod. Appl. Sci.*, 2011, 5, 130–135.

[21] R. Giovannetti, C. A. D'Amato, M. Zannotti, E. Rommozzi, R. Gunnella, M. Minicucci and A. Di Cicco, *Sci. Rep.*, 2015, 2, 17801.

[22] V. Augugliaro, M. Bellardita, V. Loddo, G. Palmisano, L. Palmisano and S. Yurdakal, *J. Photochem. Photobiol. C Photochem. Rev.*, 2012, 13, 224–245.

[23] D. Sud and P. Kaur, *Crit. Rev. Environ. Sci. Technol.*, 2012, 42, 2365–2407.

[24] J. L. Wang and L. J. Xu, *Crit. Rev. Environ. Sci. Technol.*, 2012, 42, 251–325.

[25] K. Hashimoto, H. Irie and A. Fujishima, *Jpn. J. Appl. Phys.*, 2005, 12, 8269–8285.

[26] M. U. D. Sheikh, G. A. Naikoo, M. Thomas, M. Bano and F. Khan, *New J. Chem.*, 2016, 40, 5483–5494.

[27] N. Zhang, Y. Zhang and Y. J. Xu, *Nanoscale*, 2012, 4, 5792–5813.

[28] S. Malato, P. Fernández-Ibáñez, M. I. Maldonado, J. Blanco and W. Gernjak, *Catal. Today*, 2009, 147, 1–59.

[29] W. K. Wang, J. J. Chen, M. Gao, Y. X. Huang, X. Zhang and H. Q. Yu, *Appl. Catal. B. Environ.*, 2016, 195, 69–76.

[30] R. R. Hao, G. H. Wang, H. Tang, L. L. Sun, C. Xu and D. Y. Han, *Appl. Catal. B. Environ.*, 2016, 187, 47–58.

[31] Y. Gua, M. Xinga and J. Zhang, *Appl. Surf. Sci.*, 2014, 319, 8–15.

[32] A. Zaleska, *Recent Pat. Eng.*, 2008, 2, 157–164.

[33] H. G. Yang, C. H. Sun, S. Z. Qiao, J. Zou, G. Liu, S. C. Smith, H. M. Cheng and G. Q. Lu, *Nature*, 2008, 453, 638–641.

[34] C. Adán, A. Bahamonde, M. Fernández-García and A. Martínez-Arias, *Appl. Catal. B. Environ.*, 2007, 72, 11–17.

[35] J. Cai, X. Wu, S. Li and F. Zheng, *Appl. Catal. B. Environ.*, 2017, 201, 12–21.

[36] L. Cheng, S. Qiu, J. Chen, J. Shao and S. A. Cao, *Mater. Chem. Phys.*, 2017, 190, 53–61.

[37] Y. Xie, Y. Meng and M. Wu, *Surf. Interface Anal.*, 2016, 48, 334–340.

[38] Z. Xing, X. Zong, Y. Zhu, Z. Chen, Y. Bai, and L. Wang, *Catal. Today*, 2016, 264, 229–235.

[39] S. Hamzezadeh-Nakhjavani, O. Tavakoli, S. P. Akhlaghi, Z. Salehi, P. Esmailnejad-Ahranjani and A. Arpanaei, *Environ. Sci. Pollut. Res.*, 2015, 22, 18859–18873.

[40] K. Qi, R. Selvaraj, T. Al Fahdi, S. Al-Kindy, Y. Kim, G. C. Wang, C. W. Tai and M. Sillanpää, *Appl. Surf. Sci.*, 2016, 387, 750–758.

[41] X. Qin, F. He, L. Chen, Y. Meng, J. Liu, N. Zhao and Y. Huang, *RSC Adv.*, 2016, 6, 10887–10894.

[42] M. Rahbar and M. Behpour, *J. Mater. Sci. Mater. Electron.*, 2016, 27, 8348–8355.

[43] L. Lin, H. Wang and P. Xu, *Chem. Eng. J.*, 2017, 310, 389–398.

[44] M. D. Stoller, S. Park, Y. Zhu, J. An and R. S. Ruoff, *Nano Lett.*, 2008, 8, 3498–3502.

[45] K. S. Novoselov, A. K. Geim, S. V. Morozov, D. Jiang, Y. Zhang, S. V. Dubonos, I. V. Grigorieva and A. A. Firsov, *Science*, 2004, 306, 666–669.

[46] A. A. Balandin, S. Ghosh, W. Bao, I. Calizo, D. Teweldebrhan, F. Miao and C. N. Lau, *Nano Lett.*, 2008, 8, 902–907.

[47] Y. Cheng, S. Zhou, P. Hu, G. Zhao, Y. Li, X. Zhang and W. Han, *Sci. Rep.*, 2017, 7, 1439.

[48] W. Sun, A. Du, G. Gao, J. Shen and G. Wu, *Microporous Mesoporous Mater.*, 2017, 253, 71–79.

[49] V. T. Tran, J. Saint-Martin, P. Dollfus and S. Volz, *Sci. Rep.*, 2017, 7, 2313.

[50] A. Wei, Y. Li, Y. Li and H. Ye, *Comput. Mater. Sci.*, 2017, 138, 192–198.

[51] A. K. Geim and K. S. Novoselov, *Nat. Mater.*, 2007, 6, 183–191.

[52] R. Leary and A. Westwood, *Carbon*, 2011, 49, 741–772.

[53] M. Hamandia, G. Berhault, C. Guillard and H. Kochkara, *Mol. Catal.*, 2017, 432, 125–130.

[54] S. Morales-Torres, L. M. Pastrana-Martínez, J. L. Figueiredo, J. J. Faria and A. M. T. Silva, *Environ. Sci. Pollut. Res.*, 2012, 19, 3676–3687.

[55] H. Adamu, P. Dubey and J. A. Anderson, *Chem. Eng. J.*, 2016, 284, 380–388.

[56] R. Giovannetti, E. Rommozzi, M. Zannotti, C. A. D'Amato, S. Ferraro, M. Cespi, G. Bonacucina, M. Minicucci and A. Di Cicco, *RSC Adv.*, 2016, 6, 93048–93055.

[57] A. Truppi, F. Petronella, T. Placido, M. Striccoli, A. Agostiano, M. L. Curri and R. Comparelli, *Catalysts*, 2017, 7, 100.

[58] Q. Xiang, J. Yu and M. Jaroniec, *Chem. Soc. Rev.*, 2012, 41, 782–796.

[59] Y. Zhang, Z. R. Tang, X. Y. Fu and J. Xu, *ACS Nano*, 2010, 4, 7303–7314.

[60] M. I. Litter, *Appl. Catal. B: Environ.*, 1999, 23, 89-114.

[61] K. Nakata and A. Fujishima, *J. Photochem. Photobiol. C.*, 2012, 13, 169-189.

[62] Y. Liao, W. Que, Q. Jia, Y. He, J. Zhang and P. Zhong, *J. Mater. Chem.*, 2012, 22, 7937.

[63] D. Dambournet, I. Belharouak and K. Amine, *Chem. Mater.*, 2010, 22, 1173–1179.

[64] A. Di Paola, M. Bellardita and L. Palmisano, *Catalysts*, 2013, 3, 36-73.

[65] V. Etacheri, C. Di Valentin, J. Schneider, D. Bahnemann and S. C. Pillai, *J. Photochem. Photobiol. C., Photochem. Rev.*, 2015, 25, 1–29.

[66] R. Asahi, Y. Taga, W. Mannstadt and A. J. Freeman, *Phys. Rev. B: Condens. Matter.*, 2000, 61, 7459.

[67] A. Amtout and R. Leonelli, *Phys. Rev. B: Condens. Matter.*, 1995, 51, 6842.

[68] M. Koelsch, S. Cassaignon, C. T. T. Minh, J. F. Guillemoles and J. P. Jolivet, *Thin. Solid. Films.*, 2004, 451, 86.

[69] V. Augugliaro, V. Loddo, G. Palmisano and L. Palmisano, *Clean by Light Irradiation Practical Applications of Supported TiO2*, RSC, 2010, ISBN: 978-1-84755-870-1.

[70] X. Jiang, M. Manawan, T. Feng, R. Qian, T. Zhao, G. Zhou, F. Kong, Q. Wang, S. Dai and J. H. Pan, *Catal. Today*, 2018, 300, 12–17.

[71] T. Ohno, K. Sarukawa, K. Tokieda and M. Matsumura, *J. Catal.*, 2001, 203, 82-86.

[72] M. Kitano and M. Hara, *J. Mater. Chem.*, 2010, 20, 627-641.

[73] F. Haber and J. Weiss, *Proc. R. Soc. Lond.*, 1934, 147, 332.

[74] I. K. Konstantinou and T. A. Albanis, *Appl. Catal. B.*, 2004, 49, 1-14.

[75] C. Chen, W. Ma and J. Zhao, *Chem. Soc. Rev.*, 2010, 39, 4206–4219.

[76] S. Girish Kumar and L. Gomathi Devi, *J. Phys. Chem. A*, 2011, 115, 13211–13241.

[77] J. M. Herrmann., *Top. Catal.*, 2005, 34, 1-4.

[78] S. Ahmed, M. G. Rasul, R. Brown and M. A. Hashib, *J. Environ. Manage.*, 2011, 92, 311-330.

[79] J. A. Ayllón, A. Figueras, S. Garelik, L. Spirkova, J. Durand and L. Cot, *J. Mater. Sci. Lett.*, 1999, 18, 1319-1321.

[80] J. M. Herrmann, *Catal. Today*, 1999, 53, 115-129.

[81] U. G. Akpan and B. H. Hameed, *J. Hazard. Mater.*, 2009, 170, 520–529.

[82] C. H. Chiou, C.Y. Wu and R. S. Juang, *Chem. Eng. J.*, 2008, 139, 322–329.

[83] S. Sakthivel, B. Neppolianb, M. V. Shankarb, B. Arabindoob, M. Palanichamyb and V. Murugesan, *Sol. Energy Mater. Sol. Cells.*, 2003, 77, 65-82.

[84] B. Neppolian, H. C. Choi, S. Sakthivel, B. Arabindoo and V. Murugesan, *Chemosphere*, 2002, 46, 1173-1181.

[85] C. Guillard, H. Lachheb, A. Houas, M. Ksibi, E. Elaloui and J. M. Herrmann, *J. Photochem. Photobiol. A: Chem.*, 2003, 158, 27-36.

[86] S. Alahiane, S. Qourzal, M. El Ouardi, A. Abaamrane and A. Assabbane, *Am. J. Anal. Chem.*, 2014, 5, 445-454.

[87] A. F. Alkaim, T. A. Kandiel, F. H. Hussein, R. Dillert and D. W. Bahnemann, *Catal. Sci. Technol.*, 2013, 3, 3216.

[88] S. El-Sherbiny, F. Morsy, M. Samir et al., *Appl. Nanosci.*, 2014, 4, 305.

[89] T. Wang, H. Jiang, L. Wan, Q. Zhao, T. Jiang, B. Wang and S. Wang, *Acta Biomaterialia*, 2015, 13, 354–363.

[90] D. G. You, V. G. Deepagan, W. Um, S. Jeon, S. Son, H. Chang, H. I. Yoon, Y. W. Cho, M. Swierczewska, S. Lee, M. G. Pomper, I. C. Kwon, K. Kim and J. Hyung Park, *Sci Rep.*, 2016, 6, 23200.

[91] C. Wang, L. Yin, L. Zhang, D. Xiang and R. Gao, *Sensors*, 2010, 10, 2088-2106.

[92] E. J. Son, J. S. Lee, M. Lee, C. H. T. Vu, H. Lee, K. Won and C. B. Park, *Sens. Actuators B*, 2015, 213, 322–328.

[93] J. Tang, J. R. Durrant and D. R. Klug, *J. Am. Chem. Soc.*, 2008, 130, 13885–13891.

[94] M. Ni, M. K. H. Leung, D. Y. C. Leung and K. Sumathy, *Renew. Sust. Energ. Rev.*, 2007, 11, 401–425.

[95] M. Grätzel, *J. Photochem. Photobiol. C Photochem. Rev.*, 2003, 4, 145-153.

[96] V. Singh, D. Joung, L. Zhai, S. Das, S. I. Khondaker and S. Seal, *Progress Mater. Sci.*, 2011, 56, 1178–1271.

[97] H. P. Cong, J. F. Chena and S. H. Yu, *Chem. Soc. Rev.*, 2014, 43, 7295–7325.

[98] N. Mahmood, C. Zhang, H. Yin and Y. Hou, *J. Mater. Chem. A*, 2014, 2, 15–32.

[99] X. Li, J. Yu, S. Wageh, A. A. Al-Ghamdi and J. Xie, *Small*, 2016, 12, 6640–6696.

[100] C. Xu, J. Zhu, R. Yuan and X. Fu, *Carbon*, 2016, 96, 394–402.

[101] J. Zhu, D. Yang, Z. Yin, Q. Yan and H. Zhang, *Small*, 2014, 10, 3480–3498.

[102] N. Li, G. Liu, C. Zhen, F. Li, L. Zhang and H. M. Cheng, *Adv. Funct. Mater.*, 2011, 21, 1717–1722.

[103] F. Maroni, R. Raccichini, A. Birrozzi, G. Carbonari, R. Tossici, F. Croce, R. Marassi, R. and F. Nobili, *J. Power Sources*, 2014, 269 873–882.

[104] B. Tang, Z. W. Wang, W. Q. Huang, S. Li, T. T. Ma, H. G. Yu and X. F. Li, *Nanoscale Res. Lett.*, 2017, 12, 527–533.

[105] Y. F. Sun, X. B. Wang, B. Tang, J. M. Ban, Y. F. He, W. Q. Huang, C. B. Tao and H. Luo, *Mater. Lett.*, 2017, 189, 54–57.

[106] B. T. H. Chen, H. Peng, Z. Wang and W. Huang, *Nanomaterials*, 2018, 8, 105.

[107] A. H. C. Neto, F. Guinea, N. M. R. Peres, K. S. Novoselov and A. K. Geim, *Rev. Mod. Phys.*, 2009, 81, 109–162.

[108] K. F. Maka, M. Y. Sfeir, J. A. Misewich and T. F. Heinz, *PNAS*, 2010, 107, 14999–15004.

[109] Z. X. Xu, H. Y. Gao and G. X. Hu, *Carbon*, 2011, 49, 4731–4738.

[110] T. Kaplas and P. Kuzhir, *Nanoscale Res. Lett.*, 2016, 11, 54.

[111] A. Allagui, M. A. Abdelkareem, H. Alawadhi and A. S. Elwakil, *Sci. Rep.*, 2016, 6, 21282.

[112] R. Giovannetti, E. Rommozzi, M. Zannotti and C. A. D'Amato, *Catalysts*, 2017, 7, 305.

[113] Y. Cui, H. Zhang, W. Chen, Z. Yang and Q. Cai, *J. Phys. Chem. C*, 2017, 121, 15282–15287.

[114] L. A. Galves, J. M. Wofford, G. V. Soares, U. Jahn, C. Pfüller, H. Riechert and J. M. J. Lopes, *Carbon*, 2017, 115, 162–168.

[115] P. Ramnani, M. R. Neupane, S. Ge, A. A. Balandin, R. K. Lake and A. Mulchandani, *Carbon*, 2017, 123, 302–306.

[116] M. Lukosius, J. Dabrowski, J. Kitzmann, O. Fursenko, F. Akhtar, M. Lisker, G. Lippert, S. Schulze, Y. Yamamoto, M. A. Schubert, et all. *ACS Appl. Mater. Interfaces*, 2016, 8, 33786–33793.

[117] H. Zhang, X. Zhang, X. Sun and Y. Ma, *Sci. Rep.*, 2013, 3, 3534.

[118] M. Hajian, M. Zareie, D. Hashemiana and M. Bahrami, *RSC Adv.*, 2016, 6, 73331–73335.

[119] B. Qin, T. Zhang, H. Chen and Y. Ma, *Carbon*, 2016, 102, 494–498.

[120] M. S. Poorali and M. M. Bagheri-Mohagheghi, *J. Mater. Sci. Mater. Electron.*, 2017, 28, 6186–6193.

[121] M. S. A. Bhuyan, M. N. Uddin, M. M. Islam, F. A. Bipasha and S. S. Hossain, *Int. Nano Lett.*, 2016, 6, 65–83.

[122] B. Xiao, X. Li, X. Li, B. Wang, C. Langford, R. Li and X. Sun, *J. Phys. Chem. C.*, 2014, 118, 881–890.

[123] X. Yang, X. Dou, A. Rouhanipour, L. Zhi, H. J. Räder and K. Mülle, *J. Am. Chem. Soc.*, 2008, 130, 4216–4217.

[124] B. Zou, X. X. Wang, X. X. Huang and J. N. Wang, *Chem. Commun.*, 2015, 51, 741–744.

[125] R. Jabari-Seresht, M. Jahanshahi, A. Rashidi and A. A. Ghoreyshi, *Chem. Eng. Technol.*, 2013, 36, 1550–1558.

[126] M. Khan, M. N. Tahir, S. F. Adil, H. U. Khan, M. R. H. Siddiqui, A. A. Al-Warthan and W. Tremel, *J. Mater. Chem. A.*, 2015, 3, 18753–18808.

[127] H. Kim, A. A. Abdala and C. W. Macosko, *Macromolecules*, 2010, 43, 6515–6530.

[128] M. Yi and Z. Shen, *J. Mater. Chem. A.*, 2015, 3, 11700–11715.

[129] U. Coscia, M. Palomba, G. Ambrosone, G. Barucca, M. Cabibbo, P. Mengucci, R. de Asmundis and G. Carotenuto, *Nanotechnology*, 2017, 28, 19.

[130] Y. R. Leroux, J. F. Bergamini, S. Ababou, J. C. Le Breton and P. Hapiot, *J. Electroanal. Chem.*, 2015, 753, 42–46.

[131] S. T. Hossaina and R. Wanga, *Electrochim. Acta*, 2016, 216, 253–260.

[132] M. J. McAllister, J. L. Li, D. H. Adamson, H. C. Schniepp, A. A. Abdala, J. Liu, M. Herrera-Alonso, D. L. Milius, R. Car, R. K. Prudhomme, et all. *Chem. Mater.*, 2007, 19, 4396–4404.

[133] M. Beidaghi, Z. Wang, L. Gu and C. Wang, *J. Solid State Electrochem.*, 2012, 16, 3341–3348.

[134] M. J. Allen, V. C. Tung and R. B. Kaner, *Chem. Rev.*, 2010, 110, 132–145.

[135] S. Park and R. S. Ruoff, *Nat. Nanotechnol.*, 2009, 4, 217–224.

[136] L. Y. Jiao, X. R. Wang, G. Diankov, H. L. Wang and H. J. Dai, *Nat. Nanotechnol.*, 2010, 5, 321–325.

[137] D. V. Kosynkin, A. L. Higginbotham, A. Sinitskii, J. R. Lomeda, A. Dimiev, B. K. Price and J. M. Tour, *Nature*, 2009, 458, 872–876.

[138] T. Lin, Z. Liu, M. Zhou, H. Bi, K. Zhang, F. Huang, D. Wan and Y. Zhong, *ACS Appl. Mater. Interfaces*, 2014, 6, 3088–3092.

[139] G. Q. Xin, W. Hwang, N. Kim, S. M. Cho and H. Chae, *Nanotechnology*, 2010, 21, 40.

[140] Y. Shen, T. Jing, W. Ren, J. Zhang, Z. G. Jiang, Z. Z. Yu and A. Dasari, *Compos. Sci. Technol.*, 2012, 72, 1430–1435.

[141] L. J. Cote, F. Kim and J. Huang, *J. Am. Chem. Soc.*, 2009, 131, 1043–1049.

[142] K. P. Loh, Q. L. Bao, P. K. Ang and J. X. Yang, *J. Mater. Chem.*, 2010, 20, 2277–2289.

[143] I. K. Moon and J. Lee, *Chem. Commun.*, 2011, 47, 9681–9683.

[144] C. K. Chua and M. Pumera, *Chem. Soc. Rev.*, 2014, 43, 291–312.

[145] L. Chen, Y. Hernandez, X. Feng and K. Mullen, *Angew. Chem. Int. Ed. Engl.*, 2012, 51, 7640–7654.

[146] S. Barg, F. M. Perez, N. Ni, P. V. Pereira, R. C. Maher, E. Garcia-Tunon, S. Eslava, S. Agnoli, C. Mattevi and E. Saiz, *Nat. Commun.*, 2014, 5, 4328.

[147] R. Ruoff, *Nat. Nano*, 2008, 3, 10–11.

[148] A. Bianco, H. M. Cheng, T. Enoki, Y. Gogotsi, R. H. Hurt, N. Koratkar, T. Kyotani, M. Monthioux, C. R. Park, J. M. D. Tascon, et all. *Carbon*, 2013, 65, 1–6.

[149] H. L. Poh, F. Sanek, A. Ambrosi, G. Zhao, Z. Sofer and M. Pumera, *Nanoscale*, 2012, 4, 3515–3522.

[150] O. C. Compton and S. T. Nguyen, *Small*, 2010, 6, 711–723.

[151] B. C. Brodie, *Philos. Trans. R. Soc. Lond.*, 1859, 149, 249–259.

[152] L. Staudenmaier, *Ber. Dtsch. Chem. Ges.*, 1898, 31, 1481–1487.

[153] W. S. Hummers Jr. and R. E. Offeman, *J. Am. Chem. Soc.*, 1958, 80, 1339–1339.

[154] H. C. Schniepp, J. L. Li, M. J. McAllister, H. Sai, M. Herrera-Alonso, D. H. Adamson, R. K. Prud'homme, R. Car, D. A. Saville and I. A. Aksay, *J. Phys. Chem. B.*, 2006, 110, 8535–8539.

[155] X. F. Gao, J. Jang and S. Nagase, *J. Phys. Chem. C.*, 2010, 114, 832–842.

[156] G. K. Ramesha and S. Sampath, *J. Phys. Chem. C.*, 2009, 113, 7985–7989.

[157] V. Abdelsayed, S. Moussa, H. M. Hassan, H. S. Aluri, M. M. Collinson and M. S. El-Shall, *J. Phys. Chem. Lett.*, 2010, 1, 2804–2809.

[158] Y. H. Ng, I. V. Lightcap, K. Goodwin, M. Matsumura and P. V. Kamat, *J. Phys. Chem. Lett.*, 2010, 1, 2222–2227.

[159] A. M. Golsheikh, H. N. Lim, R. Zakaria and N. M. Huang, *RSC Adv.*, 2015, 5, 12726–12735.

[160] K. Vinodgopal, B. Neppolian, I. V. Lightcap, F. Grieser, M. Ashokkumar and P. V. Kamat, *J. Phys. Chem. Lett.*, 2010, 1, 1987–1993.

[161] D. Voiry, J. Yang, J. Kupferberg, R. Fullon, C. Lee, H. Y. Jeong, H. S. Shin and M. Chhowalla, *Science*, 2016, 353, 1413–1416.

[162] C. M. Teh and A. R. Mohamed, *J. Alloys Compd.*, 2011, 509, 1648–1660.

[163] S. Hager and R. Bauer, *Chemosphere*, 1999, 38, 1549–1559.

[164] M. Faraldos and A. Bahamonde, *Catal. Today*, 2017, 285, 13–28.

[165] R. K. Upadhyay, N. Soin and S. S. Ro, *RSC Adv.*, 2014, 4, 3823–3851.

[166] A. Fujishima, T. N. Rao and D. A. Tryk, *J. Photochem. Photobiol. C Photochem. Rev.*, 2000, 1, 1–21.

[167] G. Hu and B. Tang, *Mater. Chem. Phys.*, 2013, 138, 608–614.

[168] M. Cruz, C. Gomez, C. J. Duran-Valle, L. M. Pastrana-Martínez, J. L. Faria, A. M. T. Silva, M. Faraldosa and A. Bahamondea, *Appl. Surf. Sci.*, 2017, 416, 1013–1021.

[169] C. Wang, M. Cao, P. Wang, Y. Ao, J. Hou and J. Qian, *Appl. Catal. A. Gen.*, 2014, 473, 83–89.

[170] L. M. Pastrana-Martínez, S. Morales-Torres, V. Likodimos, L. José, J. L. Figueiredo, J. L. Faria, P. Falaras and A. M. T. Silva, *Appl. Catal. B.*, 2012, 123, 241–256.

[171] S. Liu, H. Sun, S. Liu and S. Wang, *Chem. Eng. J.*, 2013, 214, 298–303.

[172] L. W. Zhang, H. B. Fu and Y. F. Zhu, *Adv. Funct. Mater.*, 2008, 18, 2180–2189.

[173] L. Ren, X. Qi, Y. Liu, Z. Huang, X. Wei, J. Li, L. Yang and J. Zhong, *J. Mater. Chem.*, 2012, 22, 11765–11771.

[174] R. Long, N. J. English and O. V. Prezhdo, *J. Am. Chem. Soc.*, 2012, 134, 14238–14248.

[175] S. Rehman, R. Ullah, A. M. Butt and N. D. Gohar, *J. Hazard. Mater.*, 2009, 170, 560–569.

[176] H. Wu, X. L. Wu, Z. M. Wang, H. Aoki, S. Kutsuna, K. Keiko Jimura and S. Hayashi, *Appl. Catal. B. Environ.*, 2017, 207, 255–266.

[177] S. K. Warkhade, G. S. Gaikwad, S. P. Zodape, U. Pratap, A. V. Maldhure and A.V. Wankhade, *Mater. Sci. Semicond. Process.*, 2017, 63, 18–24.

[178] W. J. Jiang, Y. F. Zhu, G. X. Zhu, Z. J. Zhang, X. J. Chen and W. Q. Yao, *J. Mater. Chem. A.*, 2017, 5, 5661–5679.

[179] G. Williams, B. Seger and P. V. Kamat, *ACS Nano*, 2008, 2, 1487–1491.

[180] X. Pan, M. Q. Yang, Z. R. Tang and Y. J. Xu, *J. Phys. Chem. C.*, 2014, 118, 27325–27335.

[181] T. Kamegawa, D. Yamahana and H. Yamashita, *J. Phys. Chem. C.*, 2010, 114, 15049–15053.

[182] E. Bekyarova, M. E. Itkis, P. Ramesh, C. Berger, M. Sprinkle, W. A. de Heer and R. C. Haddon, *J. Am. Chem. Soc.*, 2009, 131, 1336–1337.

[183] Q. Zhang, N. Bao, X. Wang, X. Hu, X. Miao, M. Chaker and D. Ma, *Sci. Rep.*, 2016, 6, 38066.

[184] Y. Yao, G. Jie, F. Bao, S. Jiang, X. Zhang and R. Ma, *RSC Adv.*, 2015, 5, 42754–42761.

[185] F. He, J. Fan, D. Ma, L. Zhang, C. Leung and H. L. Chan, *Carbon*, 2010, 48, 3139–3144.

[186] T. Kuila, S. Bose, A. K. Mishra, P. Kharna, N. H. Kim and J. H. Lee, *Progress. Mater. Sci.*, 2012, 57, 1061–1105.

[187] T. S. Sreeprasad and V. Berry, *Small.*, 2013, 9, 341–350.

[188] X. Pan, Y. Zhao, S. Liu, C. L. Korzeniewski, S. Wang and Z. Fan, *ACS Appl. Mater. Interfaces.*, 2012, 4, 3944–3950.

[189] J. S. Lee, K. H. You and C. B. Park, *Adv. Mater.*, 2012, 24, 1084–1088.

[190] M. Hu, Z. Yao and X. Wang, *Ind. Eng. Chem. Res.* 2017, 56(13), 3477–3502.

[191] H. C. Lee, W. W. Liu, S. P. Chai, A. R. Mohamed, A. Aziz, C. S. Khe, N. M. S. Hidayah and U. Hashim, *RSC Adv.*, 2017, 7(26), 15644–15693.

[192] D. R. Cooper, B. D'Anjou, N. Ghattamaneni, B. Harack, M. Hilke, A. Horth, N. Majlis, M. Massicotte, L. Vandsburger, E. Whiteway and V. Yu, *ISRN Condens. Matter Phys.*, 2012, 2012, 1–56.

[193] M. Hu, Z. Yao and X. Wang, *AIMS Mater. Sci.*, 2017, 4(3), 755–788

[194] S. B. Singh and C. M. Hussain, *Chemistry Select*, 2018, 3, 9533–9544

CHAPTER 3. EXFOLIATION OF GRAPHITE INTO GRAPHENE IN AQUEOUS SOLUTION: AN APPLICATION AS GRAPHENE-TiO₂ NANOCOMPOSITE TO IMPROVE VISIBLE LIGHT PHOTOCATALYTIC ACTIVITY

Abstract

The preparation of a graphene-TiO$_2$ heterogeneous catalyst supported on polypropylene for visible light photocatalysis was carried out. Aqueous graphene dispersions were prepared by liquid phase exfoliation of graphite in the presence of a non-ionic surfactant, Triton X-100. The obtained graphene dispersion was characterized by X-Ray Diffraction, Dynamic Light Scattering and UV-Visible spectroscopy and was subsequently used for the preparation of graphene-TiO$_2$ photocatalyst. As prepared photocatalysts were tested for the photocatalytic degradation of a refractory dye, Alizarin Red S, in water solutions as target pollutant. Graphene-TiO$_2$ nanocomposites showed higher adsorption of Alizarin Red S on the catalyst surface and higher photocatalytic activity for its degradation under visible light irradiation, respect to those obtained with pure TiO$_2$.

3.1. Introduction

The production of graphene in large quantities is an ongoing challenge for large-scale applications. Different processes are used to produce graphene from graphene oxide and need strong oxidizing and reducing agents. However, graphene fabricated under these chemical conditions tends to have a certain number of structural defects [1]. For that purpose, top-down methods, such as the exfoliation of graphite powder in liquid phase by sonication, are very promising routes due to their simplicity, versatility and low-cost [2]; besides this, ultrasound treatment offers a suitable option to create high-quality graphene in great quantity [1].

The exfoliation of graphite is a process in which graphite expands by up to hundreds of times along the c axis [3], resulting into single- or few-layer graphene, in a solvent with a surface tension close to

40 mJ m^{-2} which favours an increase of the graphite crystallites total area [4]. Exfoliation method is not oxidative and not require high temperature processes or post chemical treatments. In addition, it should be compatible with safe, user-friendly and low boiling-point solvents, like water [5].

The direct exfoliation of graphite and a good dispersion of the resulting graphene sheets need to use stabilizers to prevent their stacking. Various stabilizers have been proposed, in both organic and aqueous media, such as ionic and non-ionic surfactants [6], ionic liquids [7], polymers [8], organic salts [9] and aromatic molecules [10].

3.1.1. Aim of the Work

In our previous study [11] we have successfully used polypropylene (PP) coated TiO$_2$ in the visible light photodegradation of Alizarin Red S (ARS) obtaining efficient dye degradation, with additional advantage of easy separation of photocatalyst and possibility of reuse.

In this work, in order to obtain higher efficiently material, graphene-TiO$_2$ heterogeneous catalysts supported on PP were prepared and investigated for the first time as visible light photocatalysts in water. To reach this aim, an aqueous solution of Triton X-100 has been used for the direct exfoliation of graphite by sonication to obtain graphene (GR) dispersion. Triton X-100 is a non-ionic surfactant able to work as dispersing agent and as stabilizer to prevent layer stacking. Graphene-TiO$_2$ heterogeneous catalysts supported on polypropylene (PP@GR–TiO$_2$) were prepared from the GR dispersion. PP@GR–TiO$_2$ nanocomposites were used to treat water with ARS as target pollutant by photocatalytic reaction under visible light.

3.2. Experimental

3.2.1. Reagents and Materials

Timcal Timrex SFG 44 Special Graphite (particle size: 5 – 75 mm) was purchased from Imerys Graphite & Carbon. Triton X-100 was supplied by Merck. Titanium (IV) dioxide Anatase nano powdered (code 718467, size <25 nm), Alizarin Red S, hydrochloric acid volumetric standard 1.0 N, acetylacetone and ethanol were bought from Sigma Aldrich. All of chemicals were of analytical

grade. Polycarbonate filter (25 mm, 0.2 mm) was a Whatman Nuclepore Track-Etched membrane (WHA110606). Photocatalytic support is constituted by polypropylene 2500 material obtained from 3 M. Deionized water was freshly prepared by a laboratory deionizer (Osmo Lab UPW 2).

3.2.2. Graphene Dispersions Preparation

A series of GR dispersions were prepared by exfoliation of graphite in aqueous solution of 4% v/v Triton X-100 with ultrasonic cleaner Soltec Sonica 1200M (50 Hz – 80 W) and ultrasonic probe Hielscher UP100H (30 kHz – 100 W). Experimental conditions were reported in Table 3.1.

Table 3.1: *Experimental conditions used for graphite exfoliation.*

Number Test	Graphite (g)	Solvent (mL)	Ultrasonic Bath (h)	Ultrasonic Probe (h)
1	0.5	50	4	1
2	0.2	100	5	–
3	0.2	100	9	–

After ultrasonic treatments, dispersions were first centrifuged with a centrifuge Hermlez 323 K for 30 min at 3150 rpm and then for 30 min at 5150 rpm to sediment non-exfoliate graphite and to collect the GR dispersion. To obtain the concentration data, a precisely measured volume of dispersion was filtered under high vacuum onto a polycarbonate membrane of known mass. The resulting film was washed with 25 mL of water, dried at room temperature and the mass was then determined using a microbalance.

3.2.3. Graphene Characterization

GR dispersion was filtered under high vacuum onto a polycarbonate membrane for X-ray diffraction (XRD) measurements. XRD measurements were performed on a Debye – Scherrer diffractometer with an INEL CPS 180 position sensitive detector that allows reducing drastically the acquisition time for each pattern. As X-ray source was used a Mo K_α radiation ($\lambda = 0.7093$ Å),

generated by a Philips sealed X-ray tube and monochromatized through a graphite crystal along the 002 plane.

Different samples were prepared by H_2O dilution and by addition of various amounts of Triton X-100 to obtain the same surfactant concentrations and analysed by Dynamic Light Scattering (DLS) and UV-Vis. DLS analysis was performed using Malvern Zetasizer nano S (Malvern instrument Worcestershire, UK) equipped with a back-scattered light detector operating at 173°. UV-Vis characterization was carried out with a Cary 8454 Diode Array System spectrophotometer (Agilent Technologies Measurements).

3.2.4. Photocatalysts Preparation

In order to obtain PP@GR–TiO$_2$ photocatalysts, different amounts of graphene dispersion (containing 0.03, 0.06, 0.12 and 0.18 mg of GR) were added to TiO$_2$ during paste preparation by using TiO$_2$ Anatase diluted with water, acetylacetone and Triton X-100 as described in literature [11, 12]. In particular, to create the paste, 6 g of TiO$_2$ Anatase powder was ground in a porcelain mortar and mixed with GR dispersion and 2 mL of distilled water containing 10% v/v of acetyl acetone. Acetyl acetone was used in order to prevent the coagulation of TiO$_2$ nanoparticles. The paste was further diluted with 8 mL of distilled water with a continuous grinding for 3 minutes; after that, few drops of Triton X-100 were added in order to facilitate the spreading of the GR–TiO$_2$ paste on PP substrate. Finally, 30 mL of water were added in order to control the viscosity and the final concentration of paste. Successively, photocatalysts were supported on PP strips through dip coating technique, dried and clean with diluted HCl [11, 12]. PP strips (size: 2 cm in width and 10 cm in length) were prepared and cleaned with EtOH. GR–TiO$_2$ paste was added in a cylindrical glass until reaching a fixed level (30 mL) and the paste was stratified on PP strips. After each immersion of 1 minute, strips were extracted, dried at room temperature and further dried in the stove at 110°C for 30 minutes. Finally, strips were clean up with diluted HCl solution to remove the excess of TiO$_2$ particles. This procedure was repeated 3 times in order to obtain PP@GR–TiO$_2$ photocatalysts with an adequate thickness. The obtained surface area of each strip was of 18 cm^2.

3.2.5. Dye Adsorption and Photodegradation Tests

ARS adsorption and photodegradation were investigated at 25°C and at acidic pH by using a thermostated photo reactor. Initially, nine PP@GR–TiO$_2$ strips were immersed into solutions of ARS at concentrations ranging from 2.92 x 10^{-5} to 8.77 x 10^{-5} mol L^{-1}. Adsorption phase was performed for 2 h in dark conditions and successively, the system was exposed to visible light (tubular JD lamp, 80 W, 1375 Lumen) in order to start the photodegradation step.

Adsorption and photodegradation processes were monitored by UV-Vis, in real-time mode every 7 minutes, using a quartz cuvette in continuous flux (Hellma Analytics, 178.710-QS, light path 10 mm) connected through a peristaltic pump Gilson miniplus 3 to the photo reactor. Kinetic study was carried out monitoring over time the decrease of absorbance at the maximum ARS wavelength of 424 nm.

3.3. Results and Discussions

3.3.1. Characterization of Graphene Dispersion

Water is usually considered as the better solvent, but it is inappropriate to exfoliate graphite or to disperse graphene. Thus, the maximum amount of water should be determined to guarantee the maximum production of graphene in aqueous solution.
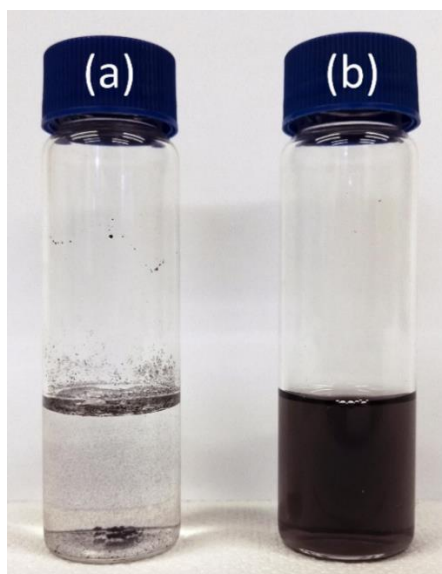
Figure 3.1: Graphite (a) and GR (b) dispersions in H$_2$O/Triton X-100 [13].

Water solution of Triton X-100 surfactant as co-solvent was used by two reasons: the first is because it is present in the catalyst paste formulation and the second is because this non-ionic surfactant was described as active water dispersant of GR [6]. Obtained dispersions of GR were characterized by a dark grey colour. Images of graphite (a) and GR (b) dispersions in H_2O/Triton X-100 as solvent are reported in Figure 3.1 [13].

In order to obtain a structural characterization of GR, the dispersion was filtered and XRD measurements were carried out. In Figure 3.2, XRD patterns of SFG 44 graphite, SFG 44 exfoliated graphite and its smoothed pattern were reported.
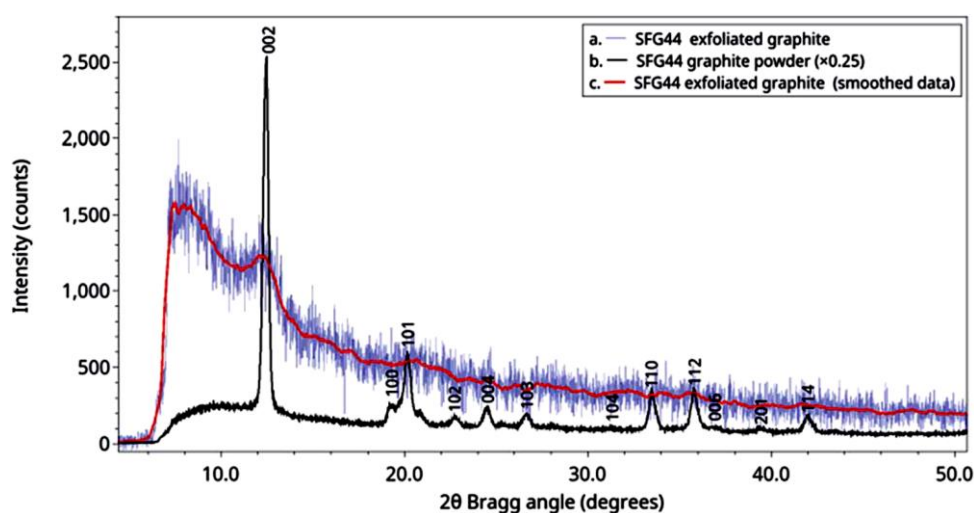
Figure 3.2: *XRD patterns of SFG 44 exfoliated graphite (a, blue shaded line), SFG 44 graphite powder (b, black line), and smoothed data of SFG 44 exfoliated graphite (c, red line).*

In Figure 3.2 is visible a broad 002 peak related to the periodic lamellar structure of graphite, that suggests a strong reduction of the long-range periodicity associated with the c-axis of graphite. However, after the exfoliation treatment, other peaks of SFG 44 graphite decreased significantly or disappeared. This behaviour confirms the loss of crystallinity of graphite structure after the ultrasound treatment and a random packing of graphene sheets.

In order to identify the best condition for the preparation of GR dispersions, DLS analysis was performed. In Figure 3.3 are reported DLS spectra of GR dispersions obtained as a function of different preparation conditions (Table 3.1), with different GR concentrations, from 3.00 to 30.00 mg L^{-1} as reported in map legend, and with the same surfactant concentrations in all samples. All traces show the presence of three peaks. The peak at around 10 nm is associated to Triton X-100, that centred at about 220 nm is associated to GR, while the peak at around 5.56 mm is associated to non-exfoliate

graphite remained at the end of the exfoliation process. GR dispersion obtained by the test number 1 showed different DLS spectra where the Triton X-100 and GR are characterized by peaks with different positions, width and, in same case, also shape; this is probably due to the high initial concentration of graphite and to the short ultrasonic time. GR dispersions obtained by test numbers 2 and 3 instead showed DLS spectra characterized by reproducible size distributions for Triton X-100 and GR. In addition, spectra of GR dispersions obtained by test number 2 were characterized by peaks of GR having a higher intensity compared to those obtained by the test number 3. This indicates that the condition applied in the test number 2 provided more concentrated GR dispersion in aqueous medium. For this reason, GR obtained at these conditions was further characterized and then applied in photocatalytic experiments.
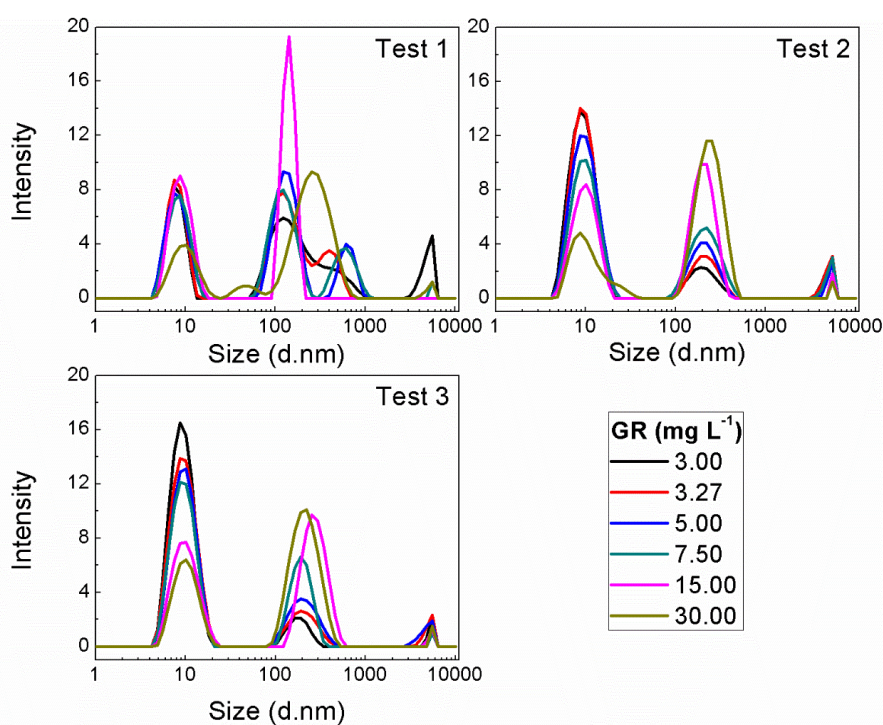
Figure 3.3: DLS spectra of GR dispersions obtained by test number 1, 2 and 3 respectively; in the map legend GR concentrations in mg L^{-1} of all samples are reported.

The GR concentration obtained by high vacuum filtration of a precisely measured volume of this dispersion was 30 mg L^{-1}.

Figure 3.4 illustrates UV-Vis absorption spectra obtained by various dilutions with water up to 10 mL of as prepared exfoliated GR dispersion (in the map legend were reported dilution factors of all samples). Triton X-100 concentration varied from 1.284 to 0.032 g L^{-1} while GR concentration varied

from 0.300 to 0.008 mg L^{-1}. As it may be observed in the Figure 3.4, spectra showed three different groups of bands in the region 190–290 nm (signed as λ_1, λ_2 and λ_3) with changes in wavelength and intensity for any specific Triton X-100 and GR concentration.
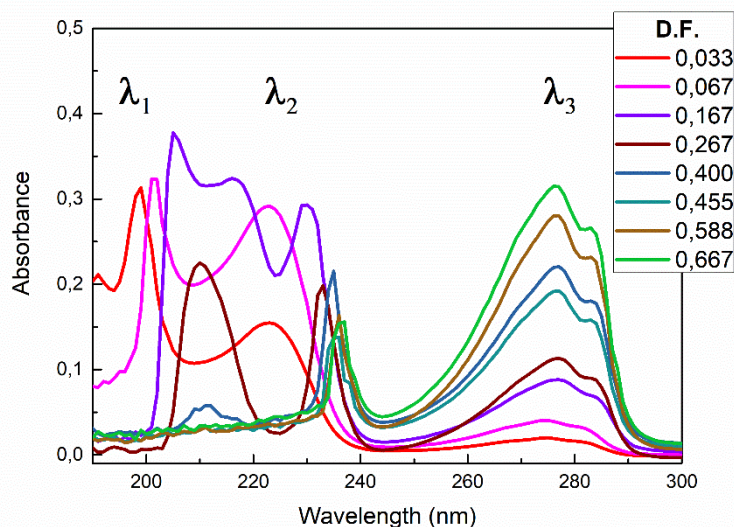
Figure 3.4: UV-Vis absorption spectra of different amounts of GR dispersion obtained by dilution with water; in the map legend dilution factors (D.F.) of all samples are reported.

A detailed analysis of λ_2 showed a wavelength shift of the different dilutions of GR dispersion as function of Triton X-100 concentration (Figure 3.5).
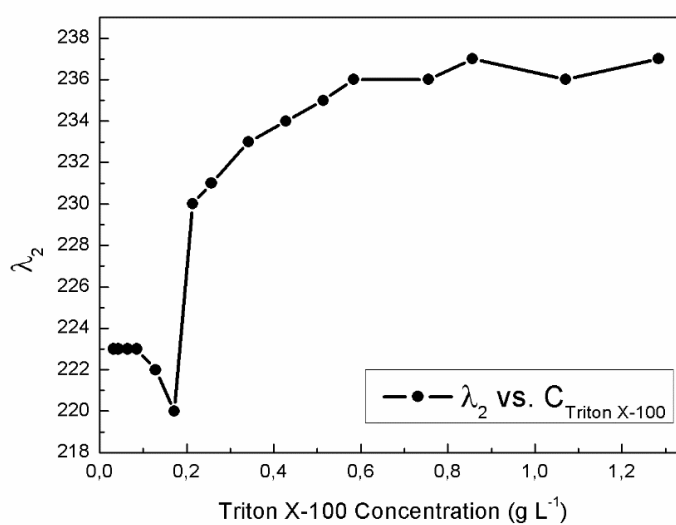
Figure 3.5: λ_2 (nm) versus Triton X-100 concentration (g L^{-1}) after dilution.

In particular, a blue shift from 237 nm to 220 nm was firstly obtained when Triton X-100 concentration moved from 1.284 to 0.214 g L^{-1}, while a red shift from 220 nm to 223 nm was then observed at lower Triton X-100 concentration. In the spectrum of Figure 3.4 absorption bands at around 270 nm (λ_3), owing to π-π* transitions of graphene [14], for all dispersions were observed; the intensity of these bands depends on the GR amount and decreases according to the increase of dilution with water. It is possible to establish a linear Pearson relationship (adjusted R^2 = 0.99122) between the concentration of GR in H$_2$O/Triton X-100 solvent and the intensity of the corresponding absorbance spectrum at 270 nm as reported in Figure 3.6.
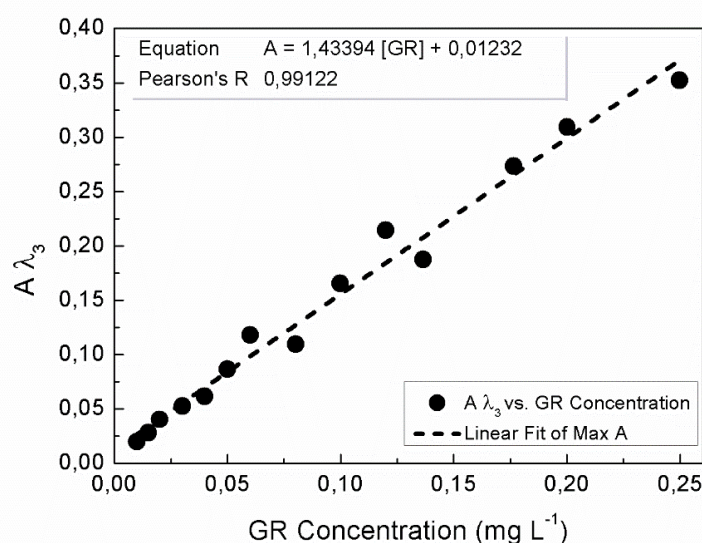
Figure 3.6: *Pearson correlation between GR concentration (mg L^{-1}) and the intensity of the corresponding absorbance at 270 nm.*

To better understand the observed behaviour, the GR amount was keep constant varying only the Triton X-100 concentration. Figure 3.7 illustrates UV-Vis absorption spectra obtained by dispersion of 0.008 mg of as prepared exfoliated GR with different amounts of Triton X-100 (in the map legend were reported the Triton X-100 concentration in g L^{-1} of all samples). In this case, the obtained spectra showed that, although the amount of GR is the same, the intensity of absorption band at around 270 nm increases with the increase of amount of Triton X-100. In addition, changes in wavelength and intensity were observed in bands at around 190 and 240 nm at specific Triton X-100 concentrations.
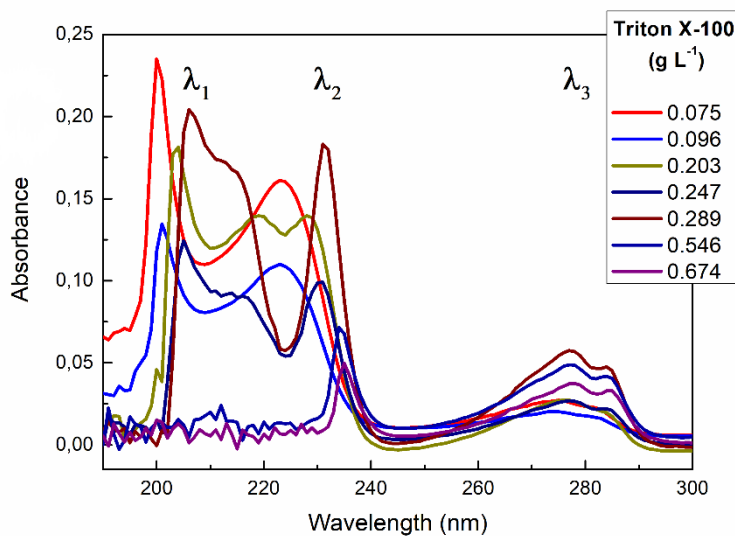
Figure 3.7: *UV-Vis absorption spectra obtained by 0.008 mg of GR with different amounts of Triton X-100; in the map legend Triton X-100 concentration in g L^{-1} of all samples are reported.*

A detailed analysis of λ_2 showed the change of wavelength as function of Triton X-100 concentration as reported in Figure 3.8.
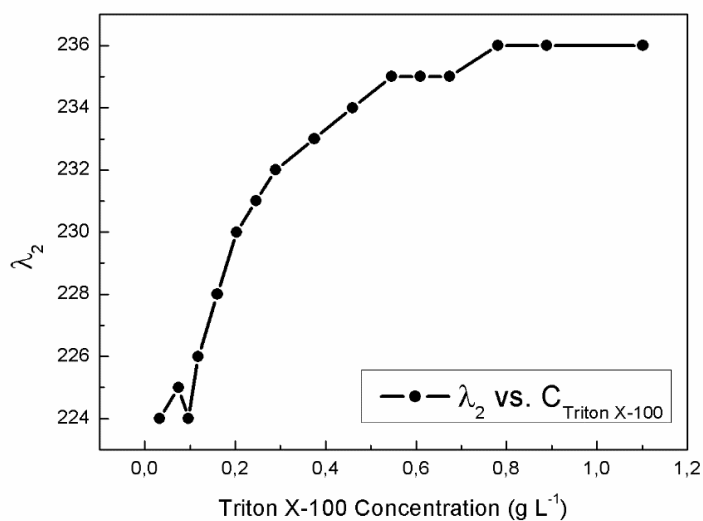
Figure 3.8: *λ_2 shift of GR dispersion as a function of Triton X-100 concentration (g L^{-1}).*

A red shift from 224 nm to 236 nm was obtained with the increase of Triton X-100 concentration, probably due to different interaction of Triton X-100 on exfoliated GR planes.

From the analysis of wavelength shifts, it is possible to deduce that the increase of surfactant concentration gives a red shift, while a blue shift is observed by increasing water. This behaviour is probably due to the variation of aggregation degree of graphene layers, depending to solvent composition. In particular, surfactant molecules balance the inter-sheet attractive forces of graphene flakes.

To confirm this hypothesis, DLS analysis was performed on samples prepared by various H_2O dilutions in which GR concentration varies from 3.0 to 30.0 mg L^{-1} while Triton X-100 concentration varies from 0.128 to 1.284 g L^{-1}. Obtained spectra are reported in Figure 3.9 (a). Analysing the central peak, it is possible to note a rightward shift (towards greater sizes) when the amount of water increases. Plotting the size change versus surfactant concentration, as reported in Figure 3.9 (b), it is clearly visible a GR size increase although the total amount of GR decreases with the dilution.
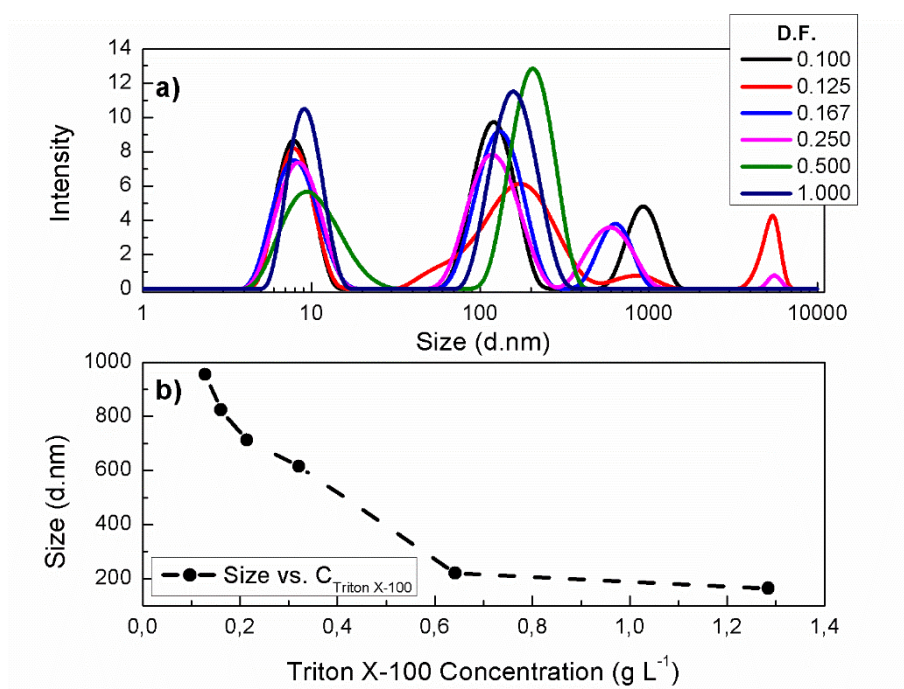
Figure 3.9: DLS spectra of samples prepared by various H_2O dilutions (a); size (nm) versus Triton X-100 concentration (g L^{-1}) (b). In the map legend dilution factors (D.F.) of all samples are reported.

This behaviour can be explained considering that to a minor size correspond a higher Triton X-100 concentration.

DLS was also performed on GR dispersion with a GR concentration from 3.0 to 30.0 mg L^{-1} at constant Triton X-100 concentration (Figure 3.10). The different percentage of the intensity of both

Triton X-100 and GR peaks is associated to the different amount of GR in samples. In fact, the increase in the GR concentration is related to the increase in the peak at 220 nm (associated with GR) without any variation of size, and a simultaneous decrease in the peak at 10 nm (associated with Triton X-100). This effect is shown in Figure 3.10 (b).
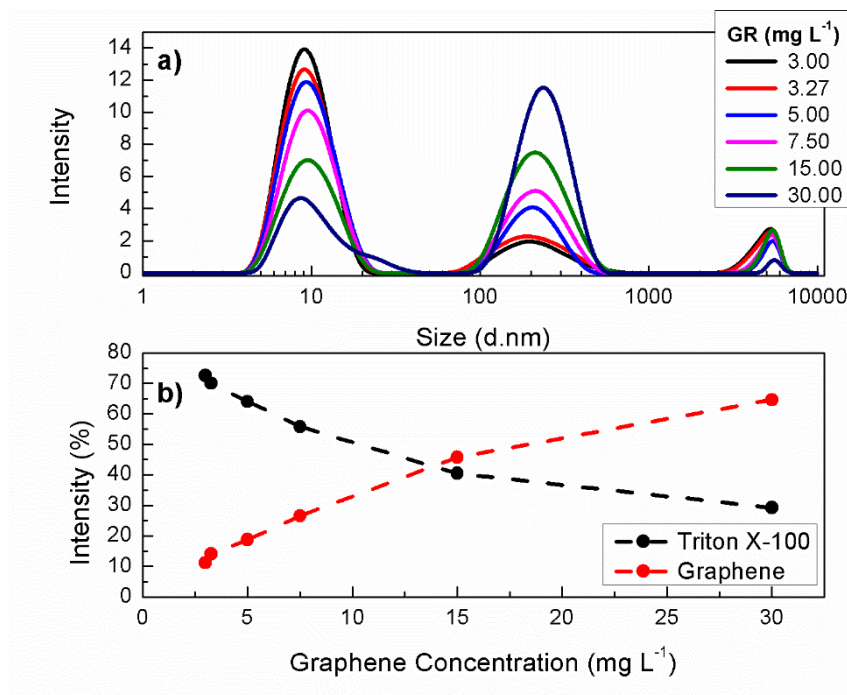
Figure 3.10: *Effect of GR concentrations (mg L^{-1}) on DLS spectra (a); intensity percentage of both GR and Triton X-100 versus GR concentration (mg L^{-1}) (b).*

Obtained results show that the exfoliated GR sheets have a size in the range 164–255 nm as a function of the Triton X-100 amount. Specifically, higher concentration of surfactant was found to be necessary to reduce the graphene layers aggregation.

3.3.2. PP@GR–TiO$_2$ Photocatalytic Application

In the first step, in order to obtain information about dye adsorption process and equilibrium data, different starting ARS concentrations, from 2.92 x 10^{-5} to 8.77 x 10^{-5} mol L^{-1}, were used. The resulting absorbance changes were monitored at 424 nm for different ARS concentrations and analysed by linear forms of Freundlich (3.1) and Langmuir (3.2) Isotherms models [11].

$$Q_e = k_F C_e^{1/n} \qquad (3.1)$$

$$Q_e = \frac{k_L C_e}{1 + \alpha_L C_e} \qquad (3.2)$$

In these Equations, C_e is the ARS concentration in solution, Q_e is the concentration of ARS adsorbed on PP@GR–TiO$_2$ at the equilibrium, k_F is a constant value that represents the capability of adsorption, and $1/n$ is the adsorption intensity; k_L and α_L are the Langmuir constants.

The relationship of adsorption data of PP@GR–TiO$_2$ with Freundlich and Langmuir Isotherms are reported in Figure 3.11.
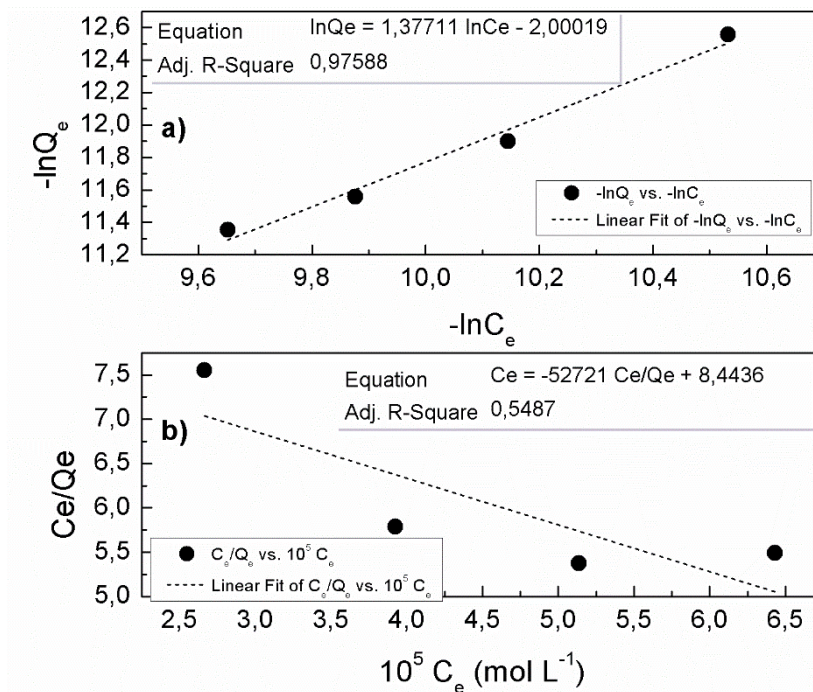
Figure 3.11: *Linear regression analysis of data using the Freundlich (a) and Langmuir (b) isotherms models.*

The experimental data fit well with the Freundlich Isotherm model (adjusted $R^2 = 0.976$) generating a k_F of 2.00 and $1/n$ of 1.38, confirming that, in the adsorption process of ARS on PP@GR–TiO$_2$, multilayer adsorption mechanism can occur as in the case of pure PP@TiO$_2$ [11].

Successively, to obtain information about the photocatalytic performance of PP@GR–TiO$_2$ photocatalysts containing different GR amounts, kinetic measurements of ARS adsorption and photodegradation by using ARS concentration of 5.84×10^{-5} mol L^{-1} were performed. The adsorbed

concentration change of ARS on different PP@GR–TiO$_2$, is reported in Figure 3.12 as function of time.
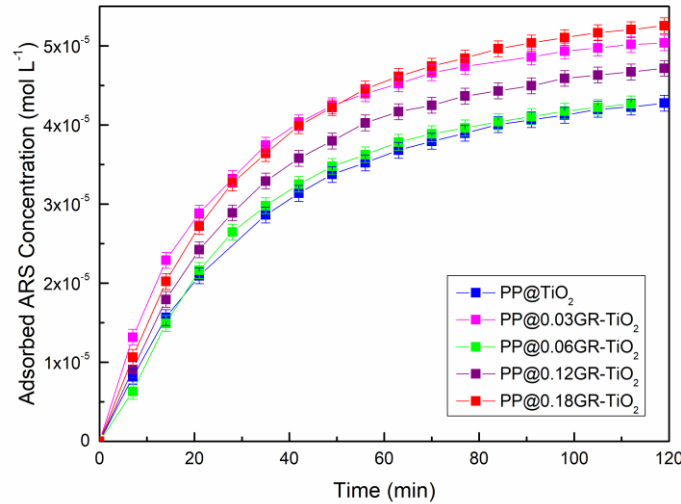
Figure 3.12: *Adsorbed concentration of ARS during time on different PP@GR–TiO$_2$ supports.*

The analysed results underwent a pseudo first order kinetic as expressed by Equation (3.3) [11]:

$$\ln\frac{Q_e - Q_t}{Q_e} = -k_{ads}t \qquad\qquad\qquad (3.3)$$

where Q$_t$ is the amount of adsorbed ARS at time t, Q$_e$ is the equilibrium concentration and k_{ads} is the pseudo first order adsorption rate constant. The plot of the first term of Equation (3.3) versus time for the different PP@GR–TiO$_2$ catalysts, provide k_{ads} and adjusted R^2 values reported in Table 3.2.

Table 3.2: *k_{ads} and k_{photo} with various catalysts.*

Catalyst name mgGR@TiO$_2$	k_{ads} x 10^2 (min^{-1})	Adj. R$_{ads}^2$	k_{photo} x 10^3 (min^{-1})	Adj. R$_{photo}^2$
PP@TiO$_2$	2.54	0.9967	7.70	0.9960
PP@0.03GR-TiO$_2$	3.28	0.9981	970	0.9949
PP@0.06GR-TiO$_2$	3.31	0.9966	11.50	0.9920
PP@0.12GR-TiO$_2$	3.30	0.9986	11.20	0.9924
PP@0.18GR-TiO$_2$	3.31	0.9996	12.50	0.9939

Trends of the adsorbed ARS concentration (C_{ads}) at the end of process and k_{ads} versus mg of GR were reported in Figure 3.13.
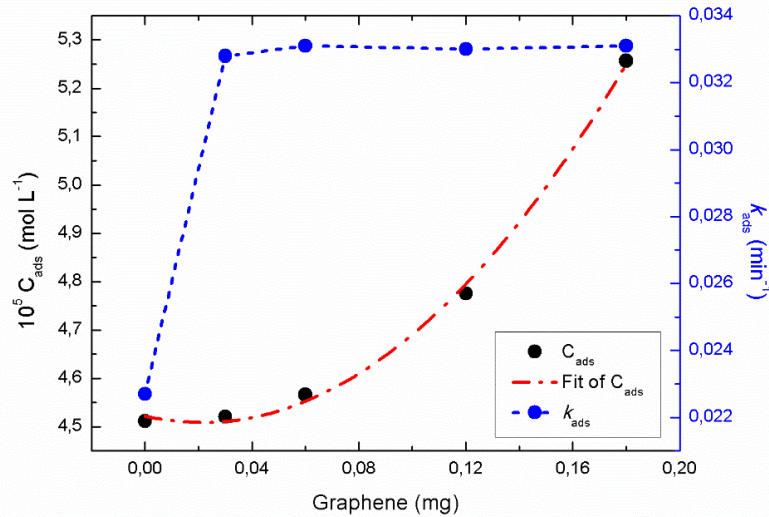
***Figure 3.13:** C_{ads} and k_{ads} versus mg of GR.*

All results showed that the presence of GR in TiO_2 influenced positively the adsorption kinetics of ARS respect to pure PP@TiO_2 but in the range from 0.03 to 0.18 mg of GR, k_{ads} values were similar for all catalysts. On the contrary, with the increases of GR, in PP@GR–TiO_2, an increase of C_{ads} were observed for the concomitant GR adsorption due to π- π interactions and to increasing of absorption surface area. These nanocomposites showed higher adsorption performances of ARS respect to pure PP@TiO_2 and the relationship between C_{ads} and the amount of graphene into catalysts can be described as a second order polynomial equation $C_{ads} = 3 \times 10^{-7}$ mgGR^2 + 4×10^{-7} mgGR + 5×10^{-5} with an adjusted determination coefficient of 0.998.

After ARS adsorption in dark conditions, in the second step, PP@GR–TiO_2 catalysts were utilized for photocatalytic degradation of ARS as a model reaction under visible-light. In Figure 3.14 are reported the photodegradation of ARS during time for different PP@GR–TiO_2 photocatalysts, showing the positive effects of the presence of GR.

Kinetic evaluation of the photodegradation process of ARS showed that all as prepared PP@GR–TiO_2 catalysts follows first order model according to the Equation (3.4) [11]:

$$\ln\frac{C}{C_0} = -k_{photo}t \qquad\qquad (3.4)$$

where k_{photo} is related rate constants, C_0 is the initial concentration of ARS and C is the concentration of ARS at time t. The plot of the first term of Equation (3.4) versus photodegradation time gives k_{photo} and adjusted R^2 values reported in Table 3.2. All results showed that, also in the photodegradation process, the presence of GR in TiO_2 influences positively photodegradation kinetics respect to pure PP@TiO_2 as demonstrated by the increase of k_{photo} values. While k_{ads} values were similar for all catalysts, the enhance of photocatalytic performance can be attributed to productive interaction between GR nano-sheets and TiO_2 in which the photogenerated electrons of TiO_2 are transferred on GR that act as electron acceptor inhibiting the electron–hole recombination [15].
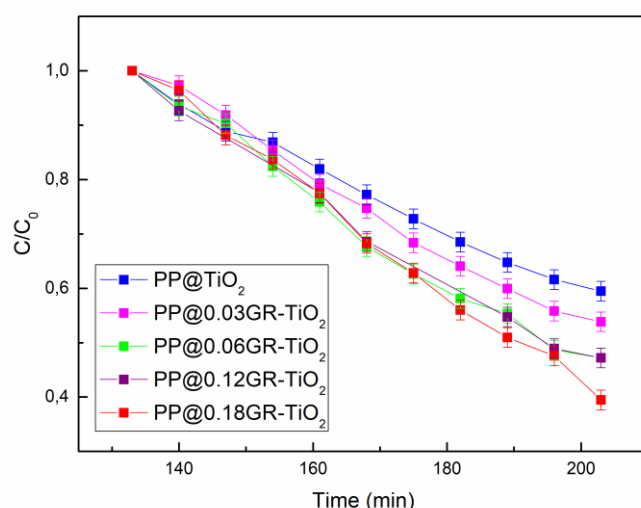
Figure 3.14: *Photodegradation of ARS as function of time with different PP@GR–TiO₂ as photocatalysts.*

Obtained results prove that the addition of GR dispersion in the formulation of TiO_2 paste promotes, thanks to the favourable interaction with Triton X-100, the homogeneity of GR and TiO_2 with consequent positive effect in efficacy of PP@GR–TiO_2 photocatalyst. By modulation of GR concentration in the paste formulation is therefore possible to increase the ARS absorption and the rate of photodegradation.

In previous study, by using PP@TiO_2 [11], photodegradation constant values were inversely proportional to the initial ARS concentration, showing that the increase of adsorbed dye on the photocatalyst decelerates the rate of the process. In this case, although the adsorbed ARS concentration increases on the PP@GR–TiO_2 due to positive effect of graphene, the obtained k_{photo} values showed the improvement of performance of this new photocatalyst.

A schematic representation of the mechanism of graphene-TiO$_2$ photocatalysis for ARS degradation is reported in Figure 3.15 [13].
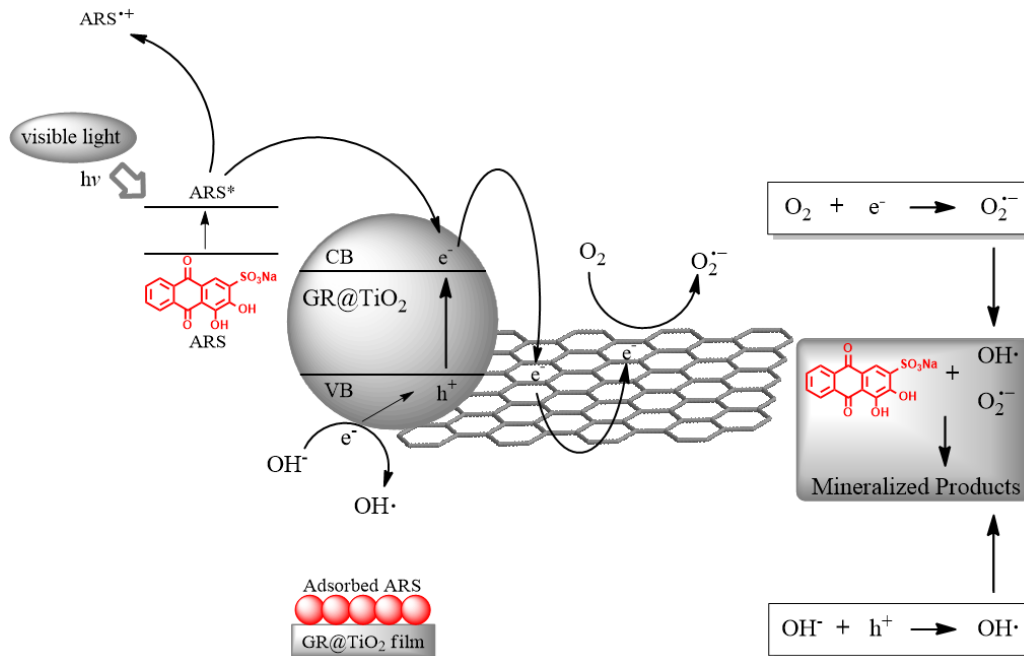
Figure 3.15: *Schematic representation of graphene-TiO$_2$ photocatalysis [13].*

Conclusions

Graphene dispersions were prepared using a simple and efficient exfoliation of graphite by liquid-phase sonication using an aqueous solution of Triton X-100 as co-solvent. The best preparation conditions were evaluated using XRD, DLS and UV-Vis analysis.

XRD confirm the loss of crystallinity of graphite structure after the ultrasound treatment and a random packing of graphene sheets.

DLS analysis proved that GR dispersions obtained by test numbers 2 and 3 were characterized by reproducible size distributions for Triton X-100 and GR. In addition, spectra of GR dispersions obtained by test number 2 were characterized by peaks of GR having a higher intensity compared to those obtained by the test number 3. This indicates that the condition applied in the test number 2 provided more concentrated GR dispersion.

From UV-Vis analysis, it is possible to deduce that the variation of aggregation degree of graphene layers depends on the solvent composition. In particular, surfactant molecules balance the inter-sheet attractive forces of graphene flakes. To confirm this, analysing the central peak of DLS spectra, it is possible to note a shift towards greater sizes when the amount of water increases; so to a minor size correspond a higher Triton X-100 concentration. Specifically, higher concentration of surfactant is necessary to reduce the graphene layers aggregation.

After characterization, the obtained GR dispersion was used to prepare graphene-TiO_2 nanocomposite that was for the first time supported on polypropylene. The obtained PP@GR–TiO_2 strips were used as photocatalytic materials for the ARS degradation in water solutions.

The adsorption process fit with the Freundlich Isotherm model confirming that multilayer adsorption mechanism occur as in the case of pure PP@TiO_2.

All results showed that the presence of GR in TiO_2 influenced positively the adsorption kinetics of ARS respect to pure PP@TiO_2 but, while k_{ads} values were similar for all catalysts, an increase of C_{ads} with the increases of GR is observed. This is due to π–π interactions and to increasing of absorption surface area.

Also in the photodegradation process, the presence of GR in TiO_2 influences positively photodegradation kinetics with respect to pure PP@TiO_2 as demonstrated by the increase of k_{photo} values. While k_{ads} values were similar for all catalysts, the enhance of photocatalytic performance can be attributed to productive interaction between GR nano-sheets and TiO_2 in which the photogenerated

electrons of TiO_2 are transferred on GR that act as electron acceptor inhibiting the electron–hole recombination.

Obtained results prove that the addition of GR dispersion in the formulation of TiO_2 paste promote, thanks to the favourable interaction with Triton X-100, the homogeneity of GR and TiO_2 with consequent positive effect in the efficacy of PP@GR–TiO_2 photocatalyst. By modulation of GR concentration in the paste formulation is therefore possible to increase the ARS adsorption and the rate of photodegradation.

References

[1] A. M. Dimiev and J. M. Tour, *ACS Nano*, 2014, 8, 3060–3068.

[2] A. Ciesielski and P. Samorì, *Chem. Soc. Rev.*, 2014, 43, 381–398.

[3] D. D. L. Chung, *J. Mater. Sci.*, 1987, 22, 4190–4198.

[4] S. Haar, M. Bruna, J. X. Lian, F. Tomarchio, Y. Olivier, R. Mazzaro, V. Morandi, J. Moran, A. C. Ferrari, D. Beljonne, A. Ciesielski and P. Samorì, *J. Phys. Chem. Lett.*,2016, 7, 2714–2721.

[5] M. Lotya, Y. Hernandez, P. J. King, R. J. Smith, V. Nicolosi, L. S. Karlsson, F. M. Blighe, S. De, Z. Wang, I. T. McGovern, G. S. Duesberg and J. N. Coleman, *J. Am. Chem. Soc.*, 2009 131, 3611–3620.

[6] L. Guardia, M. J. Fernàndez-Merino, J. I. Paredes, P. Solìs-Fernàndez, S. Villar-Rodil, A. Martìnez-Alonso and J. M. D. Tascòn, *Carbon*, 2011, 49, 1653–1662.

[7] A. T. Najafabadi and E. Gyenge, *Carbon*, 2014, 71, 58–69.

[8] Z. Sun, S. Poller, X. Huang, D. Guschin, C. Taetz, P. Ebbinghaus, J. Masa, A. Erbe, A. Kilzer, W. Schuhmann and M. Muhler, *Carbon*, 2013, 64, 288–294.

[9] W. Du, J. Lu, P. Sun, Y. Zhu and X. Jiang, *Chem. Phys. Lett.*, 2013, 568–569, 198–201.

[10] X. Dong, Y. Shi, Y. Zhao, D. Chen, J. Ye, Y. Yao, F. Gao, Z. Ni, T. Yu, Z. Shen, Y. Huang, P. Chen and L. J. Li, *Phys. Rev. Lett.*, 2009, 102, 135501.

[11] R. Giovannetti, C. A. D'Amato, M. Zannotti, E. Rommozzi, R. Gunnella, M. Minicucci and A. Di Cicco, *Sci. Rep.*, 2015, 5, 17801.

[12] R. Giovannetti, E. Rommozzi, C. A. D'Amato and M. Zannotti, *Catalysts*, 2016, 6, 84.

[13] R. Giovannetti, E. Rommozzi, M. Zannotti, C. A. D'Amato, S. Ferraro, M. Cespi, G. Bonacucina, M. Minicucci and A. Di Cicco, *RSC Adv.*, 2016, 6, 93048.

[14] Y. Zhang, S. Liu, L. Wang, X. Qin, J. Tian, W. Lu, G. Changa and X. Sun, *RSC Adv.*, 2012, 2, 538–545.

[15] X. Bai, X. Zhang, Z. Hua, W. Ma, Z. Dai, X. Huang and H. Gu, *J. Alloys Compd.*, 2014, 599, 10–18.

CHAPTER 4. REDUCED GRAPHENE OXIDE-TiO₂ NANOCOMPOSITES: FROM SYNTHESIS TO CHARACTERIZATION FOR EFFICIENT VISIBLE LIGHT PHOTOCATALYSIS

Abstract

A green and easy thermal reduction of graphene oxide using an eco-friendly system of D-(+)-Glucose and NH_4OH for the preparation of reduced graphene oxide was described. The obtained reduced graphene oxide dispersion was characterized by Dynamic Light Scattering, Raman, X-Ray Photoelectron Spectroscopy and Scanning Electron Microscopy. TiO_2 nanoparticles and reduced graphene oxide nanocomposites were successively used in the preparation of heterogeneous photocatalysts that were characterized by Atomic Force Microscopy and Photoluminescence Spectroscopy and subsequently tested as visible light photocatalysts for the photodegradation of Alizarin Red S in water as target pollutant. Obtained results demonstrated that the use of reduced graphene oxide in combination with TiO_2 led to a significant improvement for both adsorption of Alizarin Red S on the catalyst surface and photodegradation efficiency when compared to those obtained with pure TiO_2.

4.1. Introduction

In recent years, the production of graphene is an ongoing challenge in scientific community due to its remarkable properties and its great promising application in devices or composites [1]. Various procedures have been developed for graphene preparation, such as mechanical or ultrasonic exfoliation of graphite [2, 3], chemical vapor deposition [4], epitaxial growth [5] and chemical or thermal reduction of graphene oxide [6]. Among all these methods, graphene oxide reduction has become a promising route for large-scale graphene preparation. Despite this, chemical methods require reducing agents like hydrazine or sodium borohydride, that are toxic and of hazardous nature

[7]. This approach often involves highly toxic chemicals, requires long reduction time or requires high temperature treatment and produces rGO with a relatively high oxygen content to give rise to high sheet resistance [8]. It is therefore highly desired to develop new chemical reduction methods that involve less- or non-toxic chemicals for the production of rGO with low oxygen content. Therefore, new and eco-friendly approaches for graphene synthesis are required [9]. During last years, environmentally friendly methods to produce reduced graphene oxide from graphene oxide have been reported using various biomolecules [10, 11].

4.1.1. Aim of the Work

In this work, the synthesis of reduced graphene oxide (rGO) was performed applying the thermal reduction method to graphene oxide (GO) using, as reducing agent, an eco-friendly system of D-(+)-Glucose and NH_4OH solutions. Once prepared, rGO dispersion was used to produce rGO-TiO_2 nanocomposites supported on polypropylene (PP@rGO-TiO_2). These nanocomposites were tested as visible light photocatalysts for the photodegradation of Alizarin Red S (ARS) in water as target pollutant. Obtained results were discussed and compared with those derived from our previous study [12] in which we have successfully used PP@TiO_2 in the visible light photocatalytic degradation of ARS, obtaining efficient dye degradation, with additional advantage of easy separation of photocatalyst. The use of PP@rGO-TiO_2 demonstrated that the presence of rGO led to a significant improvement in terms of photocatalytic performances.

4.2. Experimental

4.2.1. Reagents and Materials

Graphene Oxide powder, D-(+)-Glucose powder, Titanium (IV) dioxide Anatase nano powdered (code 718467, size <25 nm), Alizarin Red S, NH_4OH solution 28%, hydrochloric acid volumetric standard 1.0 N and acetyl acetone were Sigma Aldrich products. Triton X-100 was purchased from Merck. All of chemicals used were of analytical grade. Catalyst support is

polypropylene 2500 material obtained from 3 M. Deionized water was prepared by Osmo Lab UPW 2 laboratory deionizer.

4.2.2. Reduced Graphene Oxide Synthesis

rGO was synthesized by GO thermal reduction. Three different procedures were performed for the reduction of GO: using only NH_4OH (1), using only D-(+)-Glucose (2) or with the use of glucose-NH_4OH (3). In all cases, GO dispersion with a concentration of 0.25 g L^{-1} was prepared and sonicated for 30 minutes with ultrasonic cleaner Ney 300 Ultrasonik in order to obtain a homogenous dispersion. In the procedure (1) and (2) in an open flask with GO dispersion, NH_4OH solution or D-(+)-Glucose was respectively added drop by drop and stirred at 80°C for 6 hours. In the procedure (3) NH_4OH solution was added to GO dispersion in order to rise the pH value to 11 and the dispersion was made to rest for one night. After that a D-(+)-Glucose solution with concentration of 8 g L^{-1} was added and the GO dispersion and stirred for 30 minutes. Therefore, the temperature was increased up to 80°C and stirred for other 3 hours; in this case the reduction was performed with a condensation column which hinders the evaporation of water and NH_4OH solutions. The thermal reduction progress was monitored by UV-Vis spectroscopy with a Cary 8454 Diode Array System spectrophotometer (Agilent Technologies Measurements). A schematic representation of glucose- NH_4OH thermal reduction is reported in Figure 4.1.
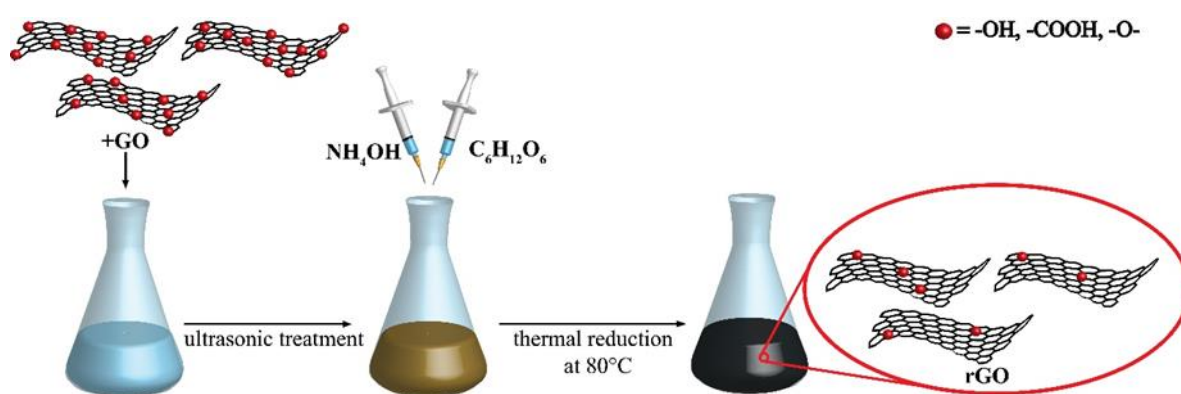
Figure 4.1: *Schematic representation of glucose-NH4OH thermal reduction of GO to rGO.*

4.2.3. Reduced Graphene Oxide Characterization

GO and rGO dispersions were characterized by Dynamic Light Scattering (DLS) measurements performed using a Malvern Zetasizer nano S (Malvern instrument Worcestershire, UK) equipped with a back-scattered light detector operating at 173°.

Raman spectra of GO and rGO dispersions were recorded using iHR320 micro-Raman spectrometer (Horiba). Samples were excited with a green laser ($\lambda = 532$ nm) emitting at room temperature and the objective outlet was 50X.

rGO dispersion was filtered under high vacuum onto a polycarbonate membrane, washed and dried in a vacuum oven (Vismara, 65) at 40°C, in order to perform the sample characterization.

X-Ray Photoelectron Spectroscopy (XPS) of GO and obtained rGO material was performed by using a unmonochromatized X-ray source (Al K_{α}) and CLAM IV hemispherical spectrometer (VG Scientific Ltd., East Grinstead, UK) with passing energy of 50 eV for an overall lower than 1 eV HWHM. The deconvolution study of the XPS spectrum was carried out by Fityk software using Voigt functions.

The filtered dried rGO was deposited on aluminum stabs using self-adhesive carbon and the morphology of the obtained rGO was examined by Field Emission Scanning Electron Microscopy (FE-SEM, Sigma Family, Zeiss) operated at 2 kV.

4.2.4. Photocatalysts Preparation and Characterization

Different amounts of rGO dispersion, containing 0.060, 0.125, 0.150, 0.188 and 0.250 mg of rGO, were added to TiO_2 during photocatalyst preparation by using TiO_2 Anatase, water, acetylacetone and Triton X-100. Obtained pastes were supported on polypropylene strips of 18 cm^2 through dip coating technique, dried and cleaned with HCl obtaining PP@rGO-TiO_2 photocatalysts, as previously described in Chapter 3 [12].

After preparation, PP@rGO-TiO_2 photocatalysts were characterized by Atomic Force Microscopy (AFM) and Photoluminescence spectroscopy (PL).

AFM images were obtained with an AFM Veeco 5000 Dimension working in tapping mode.

PL spectra were carried out with a Perkin-Elmer LS 45 luminescence spectrometer equipped with a pulsed Xe flash lamp using an excitation wavelength of 320 nm in the range from 300-900 nm.

4.2.5. Dye Adsorption and Photodegradation Tests

ARS adsorption and its photodegradation were investigated as previously described in Chapter 3 [12]. Briefly, nine PP@rGO-TiO$_2$ photocatalysts were immersed into acidic ARS solution with concentration of 5.84×10^{-5} mol L^{-1}. Adsorption phase was performed for 2 h in dark conditions and successively, the system was exposed to visible light (tubular JD lamp, 80 W, 1375 Lumen) for the photodegradation phase. Adsorption and photodegradation processes were monitored at 25°C in real time mode by a Cary 8454 Diode Array System UV-Vis spectrophotometer (Agilent Technologies Measurements) using a quartz cuvette in continuous flux (Hellma Analytics, 178.710-QS, light path 10 mm) connected to the photo reactor through a Gilson miniplus 3 peristaltic pump. Kinetic studies for adsorption and photodegradation processes of ARS were carried out monitoring during time the decrease of absorbance at a maximum wavelength of 424 nm.

4.3. Results and Discussions

4.3.1. Synthesis of Reduced Graphene Oxide

The GO dispersion in water was clear and homogeneous, with a yellow-brown colour. The obtained rGO dispersion appeared different because of its distinct structural and physicochemical properties [13, 14]. The aqueous rGO dispersion shown a distinct colour changing from yellow-brown to black after thermal reduction. After the visibility check, the progress of GO reduction was monitored measuring over time the change of UV-Vis spectrum. As reported in Figure 4.2, water GO dispersion presents a maximum at around 230 nm, attributed to $\pi\rightarrow\pi^*$ transitions of aromatic $C = C$ bonds and a shoulder at around 300 nm ascribed to $n\rightarrow\pi^*$ transition of aromatic $C = O$ bonds [15]. During the reduction, in the rGO spectrum the shoulder at 300 nm gradually disappeared, due to the progressive oxygen removal, while the maximum peak at 230 nm gradually redshifts to around 270 nm for the formation of rGO with the increase of absorbance during time [15], suggesting the restoration of the electronic conjugation within the graphene sheets.
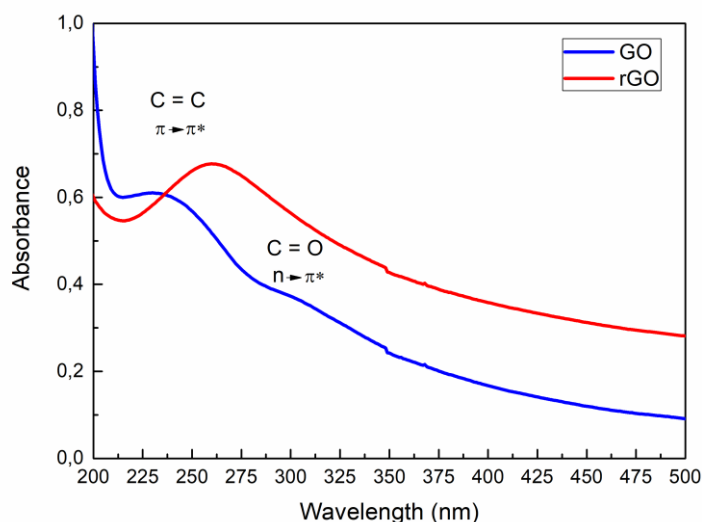
Figure 4.2: *UV-Vis Spectra of GO and rGO.*

The thermal reduction operated only with D-(+)-Glucose or NH_4OH solution in air showed only a partially reduced GO and the reduction proceeded very slowly and failed to reach completion. The alternative use of glucose-NH_4OH system in air recirculation with a condensation column, that hinders the evaporation of water and NH_4OH solutions, the change of pH value and, at the same time, allowed an efficient and speedy reduction, provided an increase in the reaction rate in the GO deoxygenation.
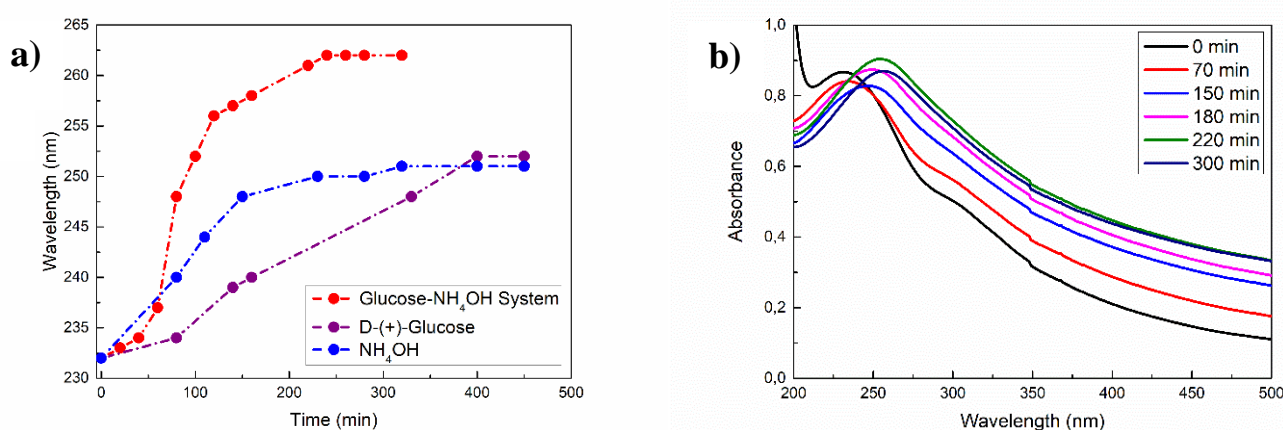
Figure 4.3: *Wavelength change of the maximum peak in the three different operative conditions (a) and UV-Vis spectral change during the reduction of Graphene Oxide in the glucose-NH_4OH system, as function of time (min) (b).*

In particular, Figure 4.3 (a) shown the change of wavelength as function of time comparing the reduction progress for all investigated operative conditions. From the plots is possible to observe that in both processes with only glucose and only NH_4OH the reduction was not complete with a wavelength shift from 232 nm to around 251 nm even after 450 min. On the other hand, with the glucose-NH_4OH system the shift was from 232 nm to around 262 nm and the reaction was completed after around 250 min. Figure 4.3 (b) shown the spectral changes during rGO formation with the glucose-NH_4OH system.

4.3.2. Characterization of Reduced Graphene Oxide

DLS, Raman and XPS analysis were very useful to investigate the efficiency of the thermal reduction by glucose-NH_4OH system.

Differences on particle sizes between GO and rGO were determined by DLS analysis and in Figure 4.4 are reported the size distributions of GO and rGO dispersions. From spectra, it is possible to observe that GO showed bigger diameter with respect to the reduced form. In particular, the spherical approximated dimensions of GO are in the range of 198 – 265.5 nm with a maximum intensity at 229.3 nm, while those relative to rGO are in the range of 110.1 – 198 nm with a maximum intensity at 147.7 nm. The decrease in size is therefore attributed to the progressive deoxygenation of GO during the reduction process, further confirming the effective reduction by the glucose-NH_4OH system.
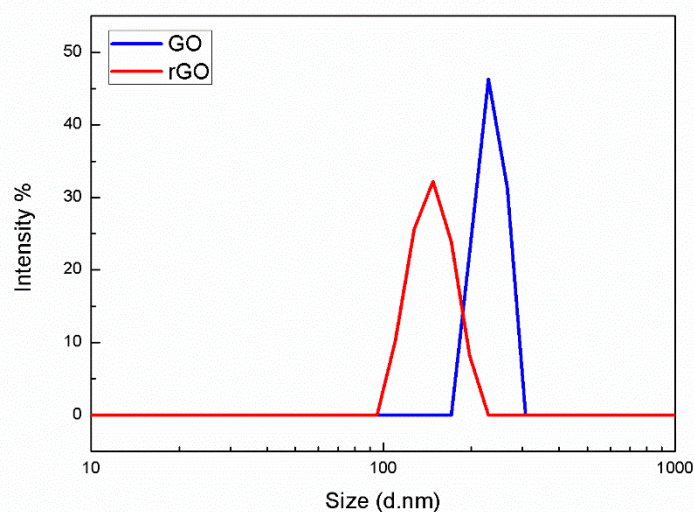
Figure 4.4: *DLS analysis of GO and rGO dispersions.*

Crystal structure, disorder and defects in GO and rGO were monitored by Raman measurements, reported in Figure 4.5, where the reduction process of GO is manifested by relative intensity changes of two main peaks: D and G peaks, located at 1327.53 and 1582.79 cm^{-1} respectively.

The G peak is attributable to the in plane stretching modes between the sp^2 carbons, while the D band is identified as the disordered band due to the structural defects, edge effects and dangling sp^2 carbon bonds that break the symmetry [16].
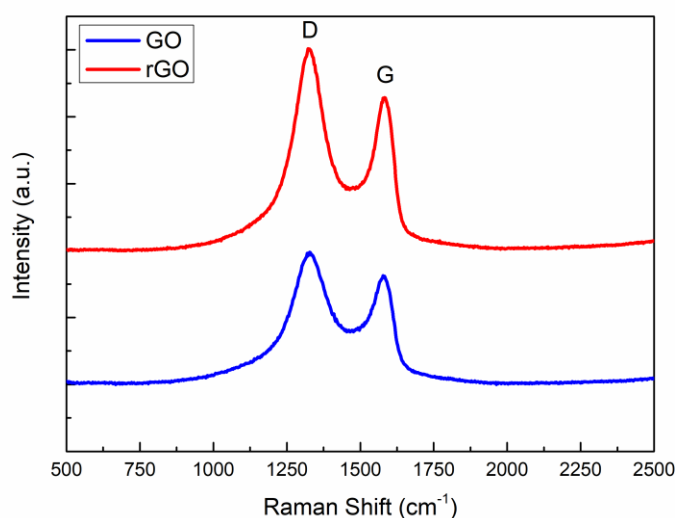
Figure 4.5: Raman spectra of GO and rGO dispersions.

From the spectra is possible to calculate the intensity ratio I_D/I_G that measures the disorder degree and is inversely proportional to the average size of the sp^2 domains [17]. The experimentally calculated I_D/I_G ratio was 1.22 for GO and 1.31 for rGO; the increase in value of this parameter confirmed the successful oxidation of the GO. The higher value of I_D/I_G intensity ratio is due to an increase in D band intensity due to the oxygen removal and to the formation of new or more graphitic domains with subsequent increasing in the sp^2 clusters number after the reduction process [18], proving an effective GO reduction using a glucose-NH$_4$OH system.

After filtration of the obtained dispersion, the rGO film was dried in vacuum and structurally characterized with XPS and SEM analysis.

XPS gives important information about the chemical and electronic state of the element present on surface and, in that case, is useful to investigate the efficiency of the thermal reduction by glucose-NH$_4$OH system; in Figure 4.6 are reported the C1s XPS spectra of GO and rGO. From the XPS spectrum of GO, a high degree of oxidation is clearly visible. Four components relative to different

functional groups can be detected: the sp^2 carbon at 284.4 eV, the carbon in the single C-O bond at 286.4 eV of epoxide and hydroxyl moieties, the C in carbonyl group (C=O) at 287.9 eV and finally the carbon relative to the carboxylate group (O-C=O) at 289.3 eV [19, 20]. On the other hand, the C1s spectrum of rGO shows the same peaks, but in this case, the intensity peaks relative to the oxygen functional groups are very weaker, demonstrating the efficient oxygen removal by thermal reduction with D-(+)-Glucose as reducing agent in presence of NH$_4$OH.
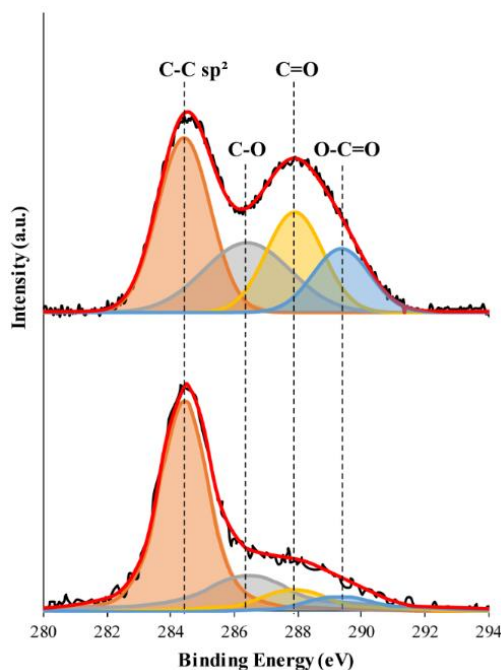
Figure 4.6: XPS spectra of GO and rGO.

SEM images in Figure 4.7 shows rGO folded sheets with distinct edges, thin and aggregated with each other in a random way forming a structured irregular conformation; this analysis confirms the efficiency in the reduction of GO.
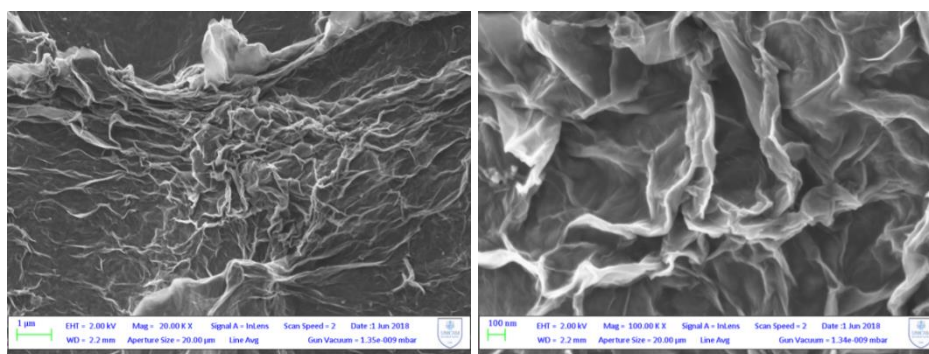
Figure 4.7: SEM images with different magnifications of rGO sheets.

4.3.3. Characterization of PP@rGO-TiO$_2$ Photocatalyst

In order to obtain more information about topography and morphological structure of PP@TiO$_2$ and PP@rGO-TiO$_2$ and to define variations in their structure as result of rGO addition, several studies were carried out by AFM and PL analysis.

AFM analysis permits to investigate the surface topography of both catalysts to check the morphological aspects of layers. For this purpose, surface roughness analysis was evaluated by mean roughness (R_a) and height of undulating (W_{max}) in order to observe the different topography and morphology with and without the presence of rGO. In Figure 4.8 (a) and (b) are showed 3D images of PP@TiO$_2$ and PP@rGO-TiO$_2$ strips respectively, while in Table 4.1 are reported R_a and W_{max} values obtained for both photocatalysts.

a)

0,97 μm

-0,04 μm

y: 5,1 μm   x: 5,1 μm

b)

0,0 μm

-1,2 μm

x: 5,0 μm   y: 5,0 μm
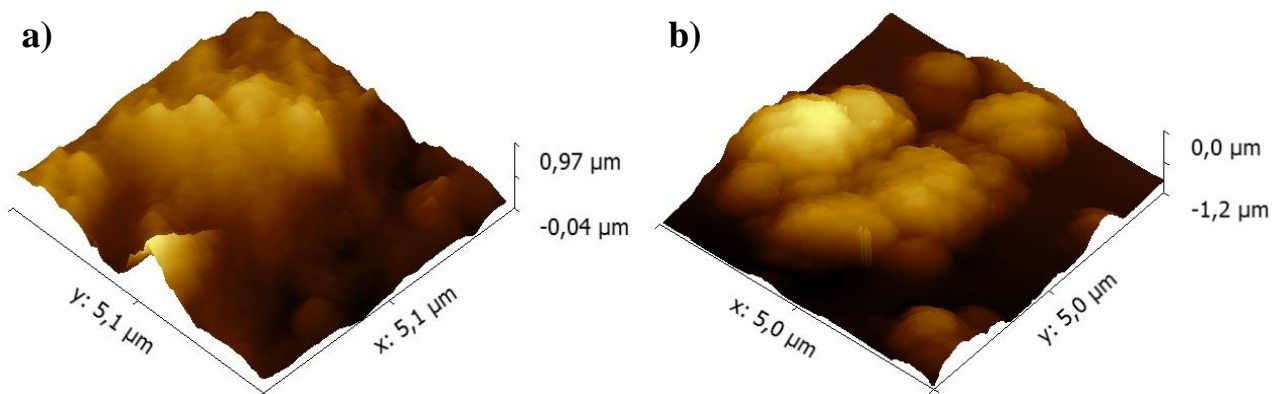
Figure 4.8: *3D images of PP@TiO$_2$ (a) and PP@rGO-TiO$_2$ (b) photocatalysts.*

Table 4.1: *R_a and W_{max} values for PP@TiO$_2$ and PP@rGO-TiO$_2$ photocatalysts.*

Catalyst name	R_a (nm)	W_{max} (nm)
PP@TiO$_2$	33.80	99.11
PP@rGO-TiO$_2$	41.40	136.40

AFM images shown important differences between PP@TiO$_2$ and PP@rGO-TiO$_2$ that was also noticeable comparing R_a and W_{max} values of Table 4.1. In the presence of rGO, photocatalyst presented a greater granular structure and a greater undulating surface respect to PP@TiO$_2$ and, at

the same time, R_a and W_{max} values increased, demonstrating that the addition of rGO led to a higher surface area for PP@rGO-TiO$_2$ photocatalyst. From this behavior it is possible to suppose that PP@rGO-TiO$_2$ layer could exhibit a higher adsorption capacity compared to PP@TiO$_2$.

A powerful demonstration of enhanced charge transposition and separation properties derived from the recombination of photoinduced charge transportation can be obtained from the study of PL signals. PL emission represents the recombination between holes and the excited electrons, and lower PL intensity emission is probably due to a lower recombination rate under the light irradiation [21]. For this reason, PL analysis was used to characterize and, at the same time, to compare PP@TiO$_2$ and PP@rGO-TiO$_2$ photocatalysts. In Figure 4.9 are reported PL spectra under excitation at 320 nm, where it is possible to observe that both photocatalyst shown a PL peak at 387 nm with a shoulder at 370 nm that are attributed to the band gap transitions [21]. PP@rGO-TiO$_2$ showed an intensity emission considerably decreased respect to the PP@TiO$_2$, demonstrating that in presence of rGO the electron–hole pairs recombination is effectively reduced on PP@rGO-TiO$_2$ surface.
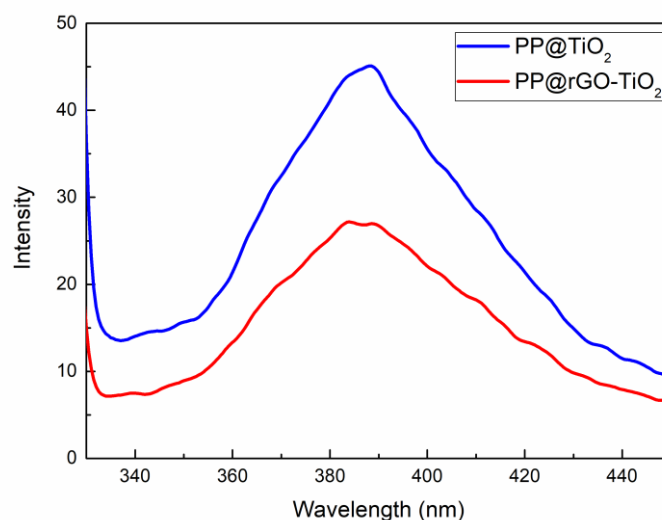
Figure 4.9: *PL spectra of PP@TiO$_2$ and PP@rGO-TiO$_2$ photocatalysts.*

In particular, the PL emission quenching observed in the PL spectrum of PP@rGO-TiO$_2$ can be explained by the transfer of photogenerated electrons from the excited TiO$_2$ to rGO sheets with effective separation of the charge carriers. Under light irradiation, electrons are excited to the conduction band of TiO$_2$, leaving positive holes in the valence band. At the same time, these electrons will undergo a fast transition to the valence band owing to the instability of excited states, resulting

in a low photocatalytic activity. In the case of PP@rGO-TiO₂, there is a formation of a heterojunction at the interface in a space-charge separation region and electrons tend to flow from the higher to the lower Fermi level to adjust energy levels. Since the work function of graphene is 4.42 eV and the conduction band position of TiO₂ is around 4.21 eV, rGO can accept photo-excited electrons from the conduction band of TiO₂ [22, 23]; this hinders the electron-hole pairs recombination that can therefore lead to an increase of the photocatalytic activity.

4.3.4. PP@rGO-TiO₂ Photocatalytic Application

In order to obtain information about dye adsorption process and equilibrium data, different starting ARS concentrations, from 2.92×10^{-5} to 8.77×10^{-5} mol L⁻¹, were used. The absorbance changes during the ARS adsorption process in dark conditions, monitored at 424 nm, showed that this process occurred according to Freundlich Adsorption Isotherm described by Equation (4.1) [12]:

$$Q_e = k_F C_e^{1/n} \qquad\qquad (4.1)$$

where C_e is the ARS concentration in solution, Q_e is the adsorbed ARS concentration on PP@rGO–TiO₂ at the equilibrium, k_F is a constant value that represents the ability of adsorption and $1/n$ is the adsorption intensity.
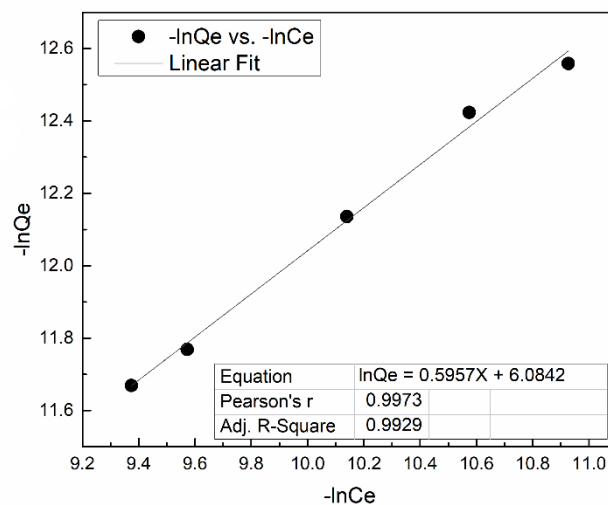
Figure 4.10: Linear regression analysis of data using the Freundlich adsorption isotherm.

The plot in Figure 4.10 confirms that PP@rGO–TiO$_2$ photocatalyst fit very well with the Freundlich Adsorption Isotherm (Pearson's r = 0.9973, adjusted R^2 = 0.9929, k$_F$ = 6.0842 and 1/n = 0.5957) and demonstrates that, in the ARS adsorption process on PP@rGO–TiO$_2$, a multilayer adsorption mechanism, due to a highly rough surface, can occur, like in the case of PP@TiO$_2$ [12] and PP@GR-TiO$_2$ [2].

Successively, to obtain information about the adsorption and photocatalytic performance of PP@rGO-TiO$_2$ photocatalysts containing different rGO amounts, kinetic measurements of ARS adsorption and photodegradation by using ARS concentration of 5.84×10^{-5} mol L^{-1} were performed. For this purpose, to characterize the adsorption kinetic, experimental data were compared with different kinetic models and it has been found that a pseudo first order kinetic, expressed by Equation (4.2), well describe obtained results [2, 12].

$$\ln\frac{Q_e - Q_t}{Q_e} = -k_{ads}t \qquad\qquad (4.2)$$

In Equation (4.2), Q$_t$ is the amount of adsorbed ARS at time t and Q$_e$ is the equilibrium concentration while k_{ads} is the pseudo first order adsorption rate constant. The k_{ads} values were obtained by the slopes of optimal straight lines derived from the plot of the logarithm term versus time of the pseudo first order kinetic equation. The graphical calculation of k_{ads} and the respective values for all studied PP@rGO-TiO$_2$ photocatalysts are reported in Figure 4.11 (a) and Table 4.2 respectively.

Comparing obtained k_{ads} values, is possible to observe that the presence of rGO in TiO$_2$ influenced positively the ARS adsorption kinetics with an increase in k_{ads} values; this phenomenon is probably due to a concomitant rGO adsorption thanks to its π-π interactions that favourably increase the adsorption surface area of photocatalysts.

Table 4.2: k_{ads} *and* k_{photo} *with various catalysts.*

Catalyst name mgrGO@TiO$_2$	k_{ads} x 10^2 (min^{-1})	Adj. R$_{ads}^2$	k_{photo} x 10^3 (min^{-1})	Adj. R$_{photo}^2$
PP@TiO$_2$	2.54	0.9967	7.70	0.9960
PP@0.060rGO-TiO$_2$	3.93	0.9965	10.10	0.9889
PP@0.125rGO-TiO$_2$	3.78	0.9978	11.20	0.9971
PP@0.150rGO-TiO$_2$	3.74	0.9979	8.89	0.9994
PP@0.188rGO-TiO$_2$	3.86	0.9940	7.73	0.9939
PP@0.250rGO-TiO$_2$	3.66	0.9964	8.41	0.9937
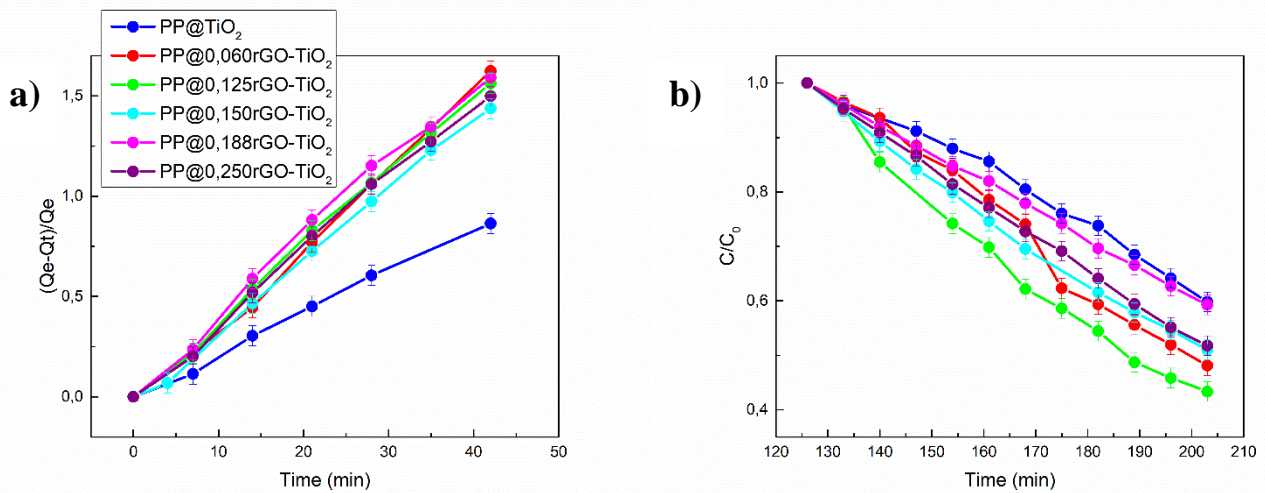
Figure 4.11: *Graphical calculation of* k_{ads} *(a) effect of time in the ARS photodegradation (b).*

Similarly, in the kinetic of the ARS photodegradation process, experimental data were compared with different kinetic models and it has been found that a first order kinetic, according to Equation (4.3), well describes obtained results [2, 12].

$$\ln\frac{C}{C_0} = -k_{photo}t \qquad\qquad (4.3)$$

In Equation (4.3), C_0 and C are the initial concentration of ARS and that at time t in solution respectively, while k_{photo} is the related first order rate constant. In Table 4.2 are reported the calculated values of k_{photo} for all PP@rGO-TiO$_2$ photocatalysts. In Figure 4.11 (b) are reported the ARS photodegradation versus time for the different PP@rGOTiO$_2$ photocatalysts; from plots is possible to deduce that the presence of rGO positively influences the photodegradation kinetics, with the best performance obtained by using PP@0.125rGO-TiO$_2$. The enhance in photocatalytic activity can be attributed to the interaction between rGO sheets and TiO$_2$ in which photogenerated electrons in the conduction band of TiO$_2$ are easily transferred on rGO, inhibiting the electron–hole pairs recombination. Using higher amounts of rGO, from 0.150 to 0.250 mg, there are only slight improvements of k_{photo} that are close to the value of PP@TiO$_2$. This behaviour may be due to an excessive rGO amounts that could go to occupy active sites of TiO$_2$ without causing positive effects in the photocatalytic activity.

A schematic representation of the mechanism of reduced graphene oxide-TiO₂ photocatalysis for ARS degradation is reported in Figure 4.12.
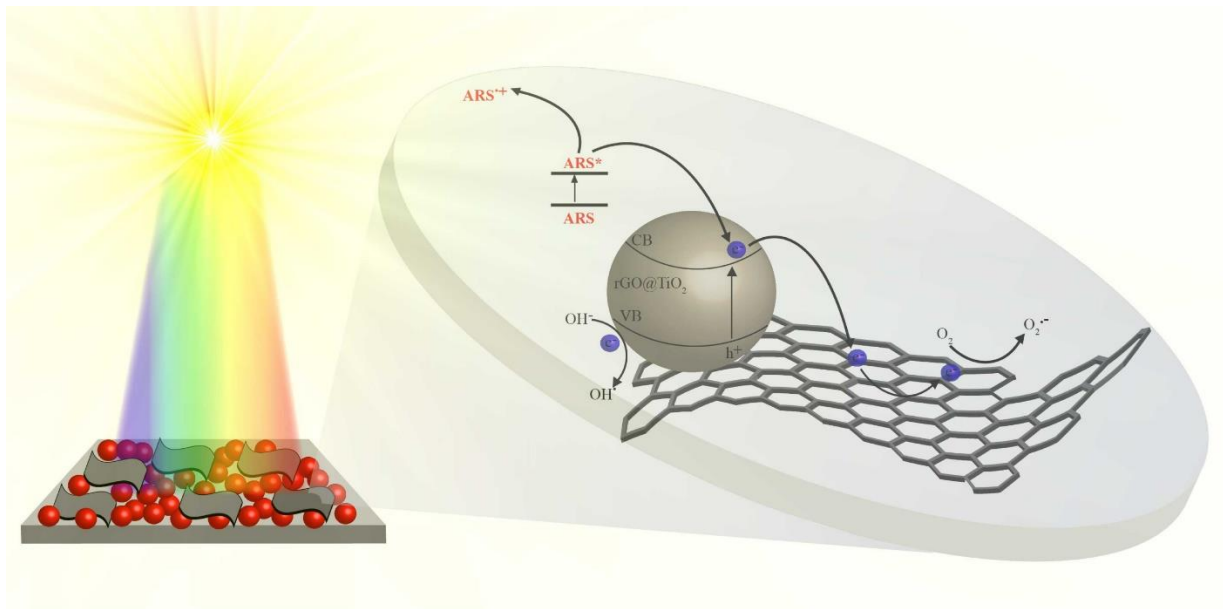
Figure 4.12: *Schematic representation of reduced graphene oxide-TiO₂ photocatalysis.*

Conclusions

Reduced graphene oxide dispersions were prepared by using three different eco-friendly thermal reduction procedures: with only D-(+)-Glucose, with only NH_4OH, and by the glucose-NH_4OH system utilizing GO as starting material. The thermal reduction of GO was monitored over time by UV-Vis spectroscopy and the best reduction method is one that use the glucose with NH_4OH. Obtained rGO were characterized using DLS, Raman, XPS and SEM analysis.

DLS analysis showed that the rGO diameter was smaller than that of GO confirming the progressive removal of oxygen content during the reduction process with consequently decrease in size.

Similarly, the I_D/I_G ratio obtained from Raman spectra increased for rGO respect to GO, probably because new or more graphitic domains were formed and the sp^2 clusters number increased after the reduction process, showing a good reduction efficiency of GO to rGO using the glucose-NH_4OH system as reducing agent.

Likewise, XPS measurements confirmed the efficient oxygen removal by thermal reduction with the glucose-NH_4OH system as reducing agent through the decrease of the intensity peaks relative to the oxygen functional groups in the C1s spectrum of rGO respect to that of GO.

Finally, morphological studies of obtained rGO film performed by SEM images revealing the characteristic layer structured, irregular and folding of an individual rGO sheet, confirming the good reduction of GO.

After characterization, the obtained rGO dispersion was used to prepare reduced graphene oxide-TiO_2 nanocomposites that were characterized by AFM and PL spectroscopy.

AFM images shown that in the presence of rGO, photocatalyst presented a greater granular structure and a greater undulating surface respect to PP@TiO_2, demonstrating that the addition of rGO in TiO_2 catalyst surface led to a higher surface area for PP@rGO-TiO_2 photocatalyst.

PL analysis shown peaks attributed to the radiative recombination of the photogenerated electron-hole pairs with a lower value for PP@rGO-TiO_2 respect to PP@TiO_2. The emission quenching observed in the PL spectrum of PP@rGO-TiO_2 was due to the formation of a heterojunction at the interface in a space-charge separation region and photogenerated electrons tend to flow from excited TiO_2 to rGO sheets with effective separation of the charge carriers that can therefore conduce to an increase of the photocatalytic activity.

After photocatalyst characterization, PP@rGO–TiO_2 strips were used as photocatalytic materials for the ARS degradation in water solutions showing that, for both adsorption and photodegradation

processes, the presence of rGO in TiO_2 nanoparticles influences positively the kinetics respect to PP@TiO_2. The increase in the adsorption kinetics was due to rGO π– π interactions that led to an increase in the absorption surface area of PP@rGO-TiO_2 photocatalyst. The higher photocatalytic performances can be explained by the interaction between rGO sheets and TiO_2 in which the photogenerated electrons in the conduction band of TiO_2 are transferred on rGO that act as electron acceptor inhibiting the electron–hole pairs recombination.

By modulating the rGO concentration in the photocatalyst paste preparation is therefore possible to increase the ARS absorption and the rate of photodegradation.

References

[1] Y. Wang, Z. X. Shi and J. Yin, *ACS Appl. Mater. Interfaces* 2011, 3, 1127–1133.

[2] R. Giovannetti, E. Rommozzi, M. Zannotti, C. A. D'Amato, S. Ferraro, M. Cespi, G. Bonacucina, M. Minicucci and A. Di Cicco, *RSC Adv.* 2016, 6, 93048–93055.

[3] M. Yi and Z. Shen, *J. Mater. Chem. A* 2015, 3, 11700–11715.

[4] Y. Zhang, L. Zhang and C. Zhou, *Acc. Chem. Res.* 2013, 46, 2329–2339.

[5] H. Tetlow, J. P. de Boer, I. J. Ford, D. D. Vvedensky, J. Coraux and L. Kantorovich, *Phys. Rep.* 2014, 542, 195–295.

[6] T. Ghosh and W. C. Oh, *J. Photocatal. Scien.* 2012, 3, 17–23.

[7] W. S. Hummers Jr and R. E. Offeman, *J. Am. Chem. Soc.* 1958, 80, 6, 1339–1339.

[8] D. R. Dreyer, S. Park, C. W. Bielawski and R. S. Ruoff, *Chem. Soc. Rev.* 2010, 39, 228–240.

[9] S. B. Maddinedi, B. K. Mandal, R. Vankayala, P. Kalluru and S. R. Pamanji, *Spectrochim. Acta, Part A* 2015, 145, 117–124.

[10] C. Zhu, S. Guo, Y. Fang and S. Dong, *ACS Nano* 2010, 4, 2429–2437.

[11] X. Fan, W. Peng, Y. Li, X. Li, S. Wang, G. Zhang and F. Zhang, *Adv. Mater.* 2008, 20, 4490–4493.

[12] R. Giovannetti, C. A. D' Amato, M. Zannotti, E. Rommozzi, R. Gunnella, M. Minicucci and A. Di Cicco, *Sci. Rep.* 2015, 5, 17801.

[13] S. Stankovich, D. A. Dikin, R. D. Piner, K. A. Kohlhaas, A. Kleinhammes, Y. Jia, Y. Wu, S. B. T. Nguyen and R. S. Ruoff, *Carbon* 2007, 45, 1558–1565.

[14] S. Liu, T. H. Zeng, M. Hofmann, E. Burcombe, J. Wei and R. Jiang, *ACS Nano* 2011, 5, 96971–96980.

[15] S. Saxena, T. A. Tyson, S. Shukla, E. Negusse, H. Chen and J. Bai, *Appl. Phys. Lett.*, 2011, 99, 013104.

[16] A. A. Dubale, W. N. Su, A. G. Tamirat, C. J. Pan, B. A. Aragaw, H. M. Chen, C. H. Chen and B. J. Hwang, *J. Mater. Chem. A*, 2014, 2, 18383-18397.

[17] G. Sobon, J. Sotor, J. Jagiello, R. Kozinski, M. Zdrojek, M. Holdynski, P. Paletko, J. Boguslawski, L. Lipinska and K. M. Abramski, *Opt. Express* 2012, 20, 19463–19473.

[18] S. Sadhukhan, T. K. Ghosh, D. Rana, I. Roy, A. Bhattacharyya, G. Sarkar, M. Chakraborty and D. Chattopadhyay, *Mater. Res. Bull.*, 2016, 79, 41–51.

[19] C. Fu, G. Zhao, H. Zhang and S. Li, *Int. J. Electrochem. Sci.*, 2013, 8, 6269–6280.

[20] S. Pei and H. M. Cheng, *Carbon*, 2012, 50, 3210–3228.

[21] Y. Wu, H. Liu, J. Zhang and F. Chen, *J. Phys. Chem. C*, 2009, 113, 14689–14695.

[22] P. K. Dubey, P. Tripathi, R. S. Tiwari, A. S. K. Sinha and O. N. Srivastava, *Int J Hydrogen Energy* 2014, 39, 16282–16292.

[23] K. Woan, G. Pyrgiotakis and W. Sigmund, *Adv. Mater.*, 2009, 21, 2233–2239.

SECTION 2

SOLAR DISINFECTION AND PHOTO-FENTON PROCESSES FOR BACTERIA INACTIVATION IN WATER

CHAPTER 5. INTRODUCTION

Pathogens causing waterborne infectious diseases constitute one of the health risks associated with urban wastewater and they have been identified as the principal cause of contamination in streams, rivers and estuaries. An appropriate treatment of wastewater and drinking water disinfection are required in order to overcome this problem [1] and, for this reason, water disinfection is a very important process to prevent the microbial contamination of water resources. Over last decades, treatment strategies like filtration, chlorination or UV-radiation for microbial inactivation have been developed and their efficiency against bacteria [2], viruses [3, 4] and parasites [5, 6] has been reported in many studies. However, because these methods generate highly toxic products, such as trihalomethanes (THM) and other carcinogenic compounds, treatment strategies are turning towards more green, low cost, easy to use and sustainable techniques, such as Advanced Oxidation Processes (AOPs) [7].

The use of solar radiation to disinfect water has been gained popularity over the past 20 years and has been successfully evaluated by several authors [8, 9] under the Solar Disinfection process (SODIS). In particular, the enhancement of the SODIS efficiency [10, 11] is meant to develop a low-cost process able to decrease the disinfection time [12]. Similarly, the increase of kinetic performances of SODIS treatments with the addition of H_2O_2 in water or the same in the Photo-Fenton process has been largely studied [13]. In SODIS treatment, H_2O_2 directly attack the cellular membrane increasing its permeability and affecting the survival of cells while, the Photo-Fenton system involve reactions of H_2O_2 with Fe^{2+} ions leading to the formation of Reactive Oxygen Species (ROS) and reactive radical species, like OH radicals, that are highly oxidant species for the inactivation of bacteria and viruses [14].

5.1. Solar Disinfection

At least one-third of developing countries population has no access to safe drinking water. The lack of adequate water supply and sanitation facilities causes a serious health hazard and exposes many to the risk of waterborne diseases [15]. Solar Disinfection (SODIS) is an efficient method against the vegetative cells of a number of emerging waterborne pathogens and is defined as an

appropriate short-term emergency intervention against bacterial species that are spore forming and may survive to this treatment [16].

The use of SODIS treatment, in which the sunlight is used to inactivate pathogens in contaminated drinking water, is an interesting approach [17]; the process was first studied and reported in scientific literature by Downes and Blunt in 1877 [18] and was effectively re-discovered as a low cost water disinfection method by Acra et al. in 1980 [19, 20]. In this application, transparent reactors are filled with contaminated water and placed in direct sunlight for at least 6 h; after exposure, water is safe to drink. A graphical description of SODIS water treatment [2] is reported in Figure 5.1.

SODIS reactors can be glass or plastic, commonly polyethylene terephthalate (PET) [21, 22] and it is recommended that water disinfected by SODIS should be consumed within 24 h to avoid the possibility of post exposure regrowth.
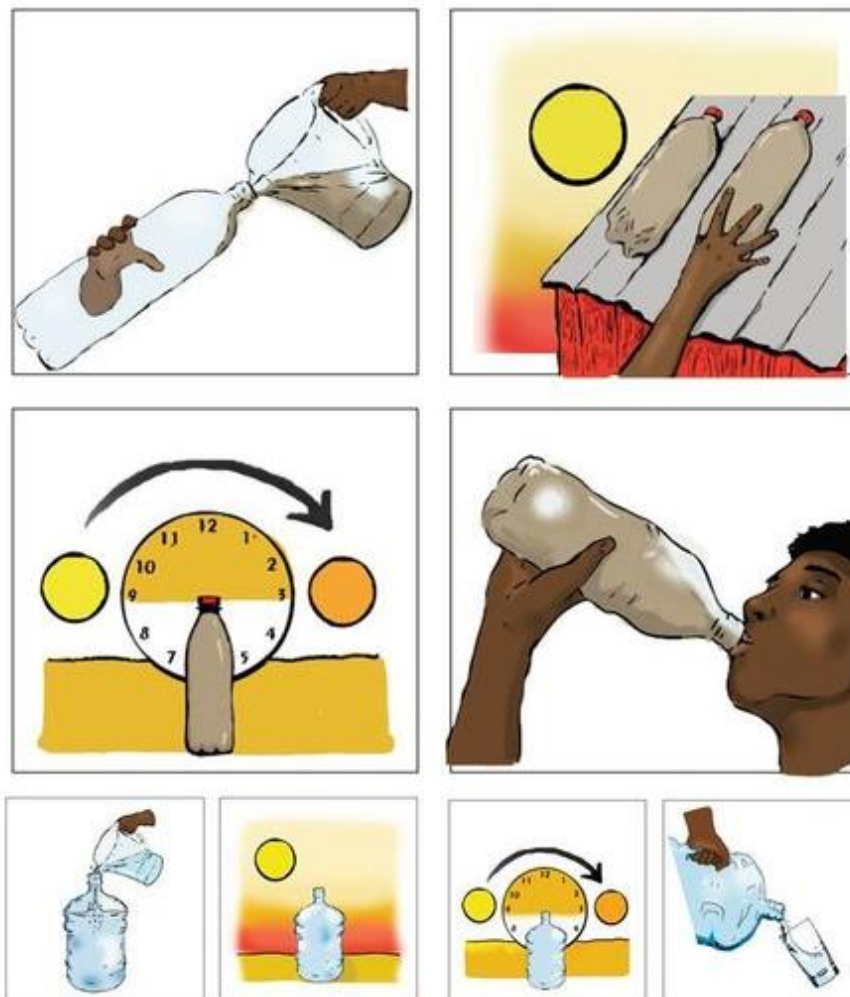
Figure 5.1: *Graphical description of SODIS water treatment [2].*

The efficiency of this protocol can be enhanced by additional steps, like:

- Put filled bottles on reflective surfaces to increase the amount of sunlight absorbed by reactor [23, 24];
- Paint with black the bottom of reactor to improve solar heating [25];
- Shake vigorously the reactor before the start of process to increase initial levels of dissolved oxygen for solar induced oxidative inactivation processes [26, 27];
- Filter water before the start of process [26].

5.1.1. Impact of Solar Radiation on DNA of Bacteria

Sunlight produces a broad spectrum of radiation; a part of this spectrum that reach the surface of Earth, as shown in Figure 5.2, is composed by UV radiation, visible light and infrared; UV radiation is classified in UV-A (320 – 400 nm), UV-B (280 – 320 nm) and UV-C (200 – 280 nm) [28].
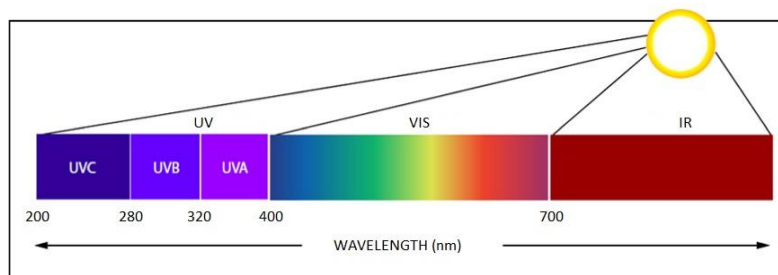
Figure 5.2: Electromagnetic Spectrum.

The exposure of microorganisms to solar radiation leads to direct and indirect damage to the cell and for this reason, pathogenic waterborne bacteria and pathogen indicators formed the focus of studies of solar disinfection efficacy.

When DNA of these microorganisms is irradiated with sunlight, some of that light is absorbed inducing cellular damage. In fact, DNA, or deoxyribonucleic acid, that is the hereditary material in almost all organisms, consists of a backbone of alternating phosphate groups and sugars covalently binding four bases: adenine, guanine, cytosine and thymine. The sugar and phosphate groups are essentially saturated molecules that absorb only in the far UV. The bases, however, absorb in the UV-B and UV-C spectral region that is effectively filtered out by the ozone layer in the stratosphere. Nevertheless, the residual radiation that reaches the Earth's surface, which increase with the depletion

of the ozone layer, is absorbed by the DNA bases and can cause serious damage by chemical modification of DNA [16]. In particular, the UV-B fraction induces dimerization of two adjacent thymines or cytosines, leading to severe damage on DNA such as single or double strand breaks and base modifications [29 - 31]. On the other end, upon UV-A and visible light irradiation, quinones, flavines and other not yet identified biological chromophores, can lead to oxidative stress generating Reactive Oxygen Species (ROS), like singlet oxygen, superoxide, hydrogen peroxide, and hydroxyl radical; these species interact with DNA, proteins and lipids, which, in turn, can cause oxidative damage to DNA bases [32]. From these absorption properties, the resulting DNA lesions generated by ROS include base and sugar lesions, strand breaks, DNA-protein cross-links and base-free sites [33, 34].

The post-exposure effects and mechanisms acting on pathogens is a matter of study since complete inactivation of microorganisms does not always happen for various reasons, usually involving poor weather or poor turbidity conditions [2]. Moreover, other microbiological parameters have been shown to have important effects on the action mechanism of sunlight on bacteria. For example, their sensitivity to the solar treatment strongly depends on the growth rate and on the physiological stage [35].

Due to its genome mapping and its status as a faecal indicator organism, Escherichia Coli is the most frequently studied bacterial in disinfection experiments [23, 36 - 38]. The inactivation of this species by SODIS is caused by the destruction of a sequence of normal cellular functions as a consequence of an arrest of ATP synthesis and efflux pump activity after the start of light exposure. These steps are followed by a gradual loss of membrane potential and a reduction in glucose uptake, ending with a change of the permeability of cytoplasmic membrane of bacterial [2].

Besides to be dependent on DNA damage caused by solar radiation, Escherichia Coli inactivation rates can be highly dependent on wavelength of used light [37, 39], dissolved oxygen [26], salts concentration in water [40] and post-irradiation growth conditions [41]. To date, all pathogenic bacteria commonly found in water are easily subjected to solar disinfection after at least 6 hours under suitable conditions [2]. Obviously, the research activity is aimed to improve this disinfection technique in order to improve its efficiency and reduce reaction times [12, 50].

5.1.2. Effect of Water Composition on Solar Disinfection

The sensitivity of bacteria to the SODIS treatment depends on the nature of the water source and on the organic and inorganic matter naturally present or introduced in natural cycles by agricultural, domestic and industrial activities that have an important effect on kinetics and on final disinfection results. For SODIS, the presence of these kind of compounds generally lead to a reduction in the rate of disinfection in comparison to that observed in distilled water [42, 43]. In particular, it is known that the organic matter can acts sometimes as photosensitizer for a large variety of chemical reactions that are produced by energy transfer, singlet oxygen and radical species generation, leading to the production of reactive oxygen species and increasing the efficiency disinfection process [44]. Other times instead, organic matter can competes with reactive oxygen species formation and with photon absorption, leading to a decrease in the disinfection efficiency [28]. On the other side, inorganic matter can give reactions that lead to the formation of OH radicals, increasing the disinfection efficiency [12], or could have a scavenging effect on OH radicals causing a reduction in efficiency either by absorption of light or by competition with reactive oxygen species formation [28]. For these reasons, depending on their concentrations, disinfection processes are inhibited or promoted in varying degrees by inorganic and organic matter [12, 53].

5.1.3. Improvement Technologies for Solar Disinfection

There are several disadvantages of SODIS treatments: the use of polyethylene terephthalate bottles allows treating only small volumes of water and the process efficiency is dependent on a range of environmental parameters including the solar irradiance, the initial water quality and the nature of the bacterial contamination [28].

There are several ways to improve the SODIS efficiency, like the design of SODIS bags [45], the use of UV dosimeter sensors [46, 47], the design of compound parabolic collectors [48] and the use of photocatalysts or chemical additive [10, 11].

The SODIS bags maximise the area for photon collection and minimise the path length for light penetration through the water to be treated. Furthermore, they could be deployed in emergencies where access to drinking water is an immediate issue, like in the case of flooding or earthquake; moreover, these bags can easily be transported and stored in large quantities [45].

UV dosimeter sensors are intelligent inks photocatalytic systems which function via photo-induced reactions that lead to the colour variation of the compounds used as indicators [49]. There are many dyes or inks, like methylene blue, that could be utilized in these systems to provide simple dosimeter sensors for corresponding to UV doses required for SODIS. These sensors could be utilized to provide some quality assurance for the SODIS treatments [46, 47].

Compound parabolic collectors are systems that collect diffuse radiation in which the collected energy is homogeneously distributed across the absorber surface. They are not based exclusively on the absorption of direct solar radiation and are therefore effective even on cloudy days. In addition, they collect radiation independently of the direction of sunlight and do not require sun tracking. The major advantage of compound parabolic collector technology is that the concentration factor remains constant for all values of sun zenith angle within the acceptance angle limit; therefore, it is theoretically possible to design larger volume reactors for SODIS treatments [28, 48].

Finally, SODIS efficiency can be enhanced by the addition of various chemicals additives or, more importantly, by using processes such as solar-assisted Advanced Oxidation Processes (AOPs). The AOPs use chemical oxidant species that through a series of electron transfer reactions lead to different reactive oxygen species (especially hydroxyl radicals), to disinfect water by inactivating potentially pathogenic species and degrading various harmful organic contaminants [2].

A widely studied AOP is the Photo-Fenton process in which hydroxyl radicals are generated using light, iron and hydrogen peroxide and acts as oxidant species in the treatment of water. Photo-Fenton process can be carried out using solar light, enhancing the efficiency of SODIS, given that iron is almost omnipresent in natural waters and hydrogen peroxide can be added and/or is in situ-generated [50].

5.2. Photo-Fenton Process

5.2.1. Chemistry of Fenton Reagents

The Fenton's process has its origin in the discovery reported by H. J. H Fenton in 1984 in which ferrous ion strongly promotes the oxidation of tartaric acid by hydrogen peroxide [51]. However, only later this oxidation activity has been attributed to hydroxyl radicals [52], that with an energy of 2.8 V, are one of the strongest oxidants species in the Fenton process [51]. The Fenton reaction is based

on an electron transfer between H_2O_2 and a metal ion such as ferrous iron, which acts as a catalyst; in particular, Fenton and related reactions are convenient ways to generate oxidizing species for bacterial inactivation and for pollutant degradation [53]. The mixture of H_2O_2 and Fe^{2+} produces hydroxyl radicals which destroyed organic pollutants and bacteria leading to the formation of carbon dioxide, water and inorganic salts as end-products [51].

The classical Fenton process involves the sequence of following reactions (Equations 5.1 – 5.7) [53 - 59].

$$Fe^{2+} + H_2O_2 \rightarrow Fe^{3+} + \cdot OH + OH^- \qquad k_1=70 \text{ M}^{-1}\text{s}^{-1} \qquad (5.1)$$

$$Fe^{3+} + H_2O_2 \rightarrow Fe^{2+} + \cdot OH_2 + H^+ \qquad k_2=0.001\text{-}0.01 \text{ M}^{-1}\text{s}^{-1} \qquad (5.2)$$

$$\cdot OH + H_2O_2 \rightarrow \cdot OH_2 + H_2O \qquad k_3=3.3 \times 10^7 \text{ M}^{-1}\text{s}^{-1} \qquad (5.3)$$

$$\cdot OH + Fe^{2+} \rightarrow Fe^{3+} + OH^- \qquad k_4=3.2 \times 10^8 \text{ M}^{-1}\text{s}^{-1} \qquad (5.4)$$

$$Fe^{3+} + \cdot OH_2 \rightarrow Fe^{2+} + O_2H^+ \qquad k_5=<2 \times 10^3 \text{ M}^{-1}\text{s}^{-1} \qquad (5.5)$$

$$Fe^{2+} + \cdot OH_2 + H^+ \rightarrow Fe^{3+} + H_2O_2 \qquad k_6=1.2 \times 10^6 \text{ M}^{-1}\text{s}^{-1} \qquad (5.6)$$

$$2\, OH_2 \cdot \rightarrow H_2O_2 + O_2 \qquad k_7=8.3 \times 10^5 \text{ M}^{-1}\text{s}^{-1} \qquad (5.7)$$

The mechanism of the Fenton process is quite complex, however it can be summarized by Equation (5.8), which represents the dissociation of H_2O_2 in the presence of iron as catalyst under acidic conditions [51].

$$2Fe^{2+} + H_2O_2 + 2H^+ \rightarrow 2Fe^{3+} + 2H_2O \qquad (5.8)$$
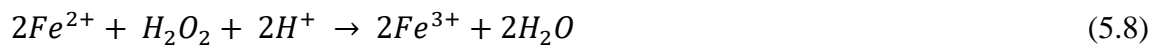
The formation of hydroxyl radicals by Equation (5.1) is very fast, the acidic condition is fundamental because the presence of H^+ ions guarantee the decomposition of H_2O_2 and iron plays the role of catalyst by changing form between Fe^{2+} and Fe^{3+}. Nevertheless, the rate of Fe^{2+} consumption, expressed by k_1, is faster than the rate of their generation, expressed by k_2; this results in the production of a large amount of ferric hydroxide sludge during the process [51].

Oxidation using Fenton's chemistry has proved to be effective and promising for the destruction of several organic compounds and for the inactivation of several kind of microorganisms, and consequently for the water treatment [60 - 62].

Besides iron, other transition metals can catalyse the process, like copper. The reaction system with copper as Fenton catalyst follow a similar scheme of reaction as that of iron and is referred to as Fenton-like reaction [63].

In last years, much attention has be paid on Fenton and Fenton-like processes, paying attention on heterogeneous process due to the disadvantages associated with homogeneous process [64]. The main drawback is the formation of a large amount of ferric hydroxide sludge at pH greater than 4 [65], that causes environmental and waste disposal issues. In addition, regeneration of catalyst is difficult because a large amount of catalytic metal is lost in the sludge. These limitations can be overcome by using heterogeneous catalysts [66] that has gained special attentions in Fenton process because its efficacy is maintained for a wider range of pH. Iron is stabilized within the catalyst structure in heterogeneous catalysis and can effectively activate the disinfection without generation of ferric hydroxide precipitation [66]. However, heterogeneous catalysis has a slower oxidation rate compared to that of homogeneous reaction [67] due to the presence of a small amount of iron on the catalyst surface. For this, recent investigations have focused on the development of new heterocatalysts with larger surface area and higher activities in degradation processes. Three possible mechanisms have been proposed for heterocatalysts action in Fenton processes [66 - 68]:

1. Iron leaching to the reaction solution and activating hydrogen peroxide through homogeneous pathway,
2. Decomposition of H_2O_2 to OH radicals by binding of H_2O_2 with iron species on the surface of catalyst,
3. Chemisorption of probe molecule on the catalyst surface.

Many heterogeneous catalysts have been used in Fenton reactions such as iron minerals, iron oxides, ferrites, clays, zeolite, alumina, fly ash based catalysts and several other [69 - 71].

5.2.2. Photo-Fenton Treatment

Photo Fenton process is rather similar to Fenton one; in particular, it is a combination of Fenton reagents (H_2O_2 and Fe^{2+}) and UV-Vis radiation ($\lambda < 580$ nm) that gives rise to additional OH radicals by two supplemental reaction [52, 66].

The first is the photolysis of Fe^{3+} to give Fe^{2+} in acidic media, shown in Equation (5.9), the second is the photolysis of H_2O_2 through shorter wavelengths, shown in Equation (5.10) [66, 72].

$$Fe(OH)^{2+} + hv \ \rightarrow \ Fe^{2+} + \ \cdot OH \qquad\qquad \lambda < 580 \text{ nm} \qquad\qquad (5.9)$$

$$H_2O_2 + hv \ \rightarrow 2OH \cdot \qquad\qquad\qquad \lambda < 310 \text{ nm} \qquad\qquad (5.10)$$

The Fe^{2+} ions photo-generated by Equation 5.9 enter in Fenton reaction (Equation 5.1) to produce supplementary hydroxyl radicals leading to an oxidation rate of Photo-Fenton Process greater than that of Fenton one. In addition, there is a considerable decrease in the total iron utilization and in the sludge generation in Photo-Fenton compared to Fenton reaction [65].

Furthermore, it has been established that Photo-Fenton using both solar or UV light, has significant effects on inactivation of microorganisms in polluted water bodies, as show in Figure 5.3, for sustainable reuse for drinking and/or irrigation purpose. However, the efficiency of the process is greatly dependent on the microorganism present [73, 74] and on the type of the water treatment [75, 76].
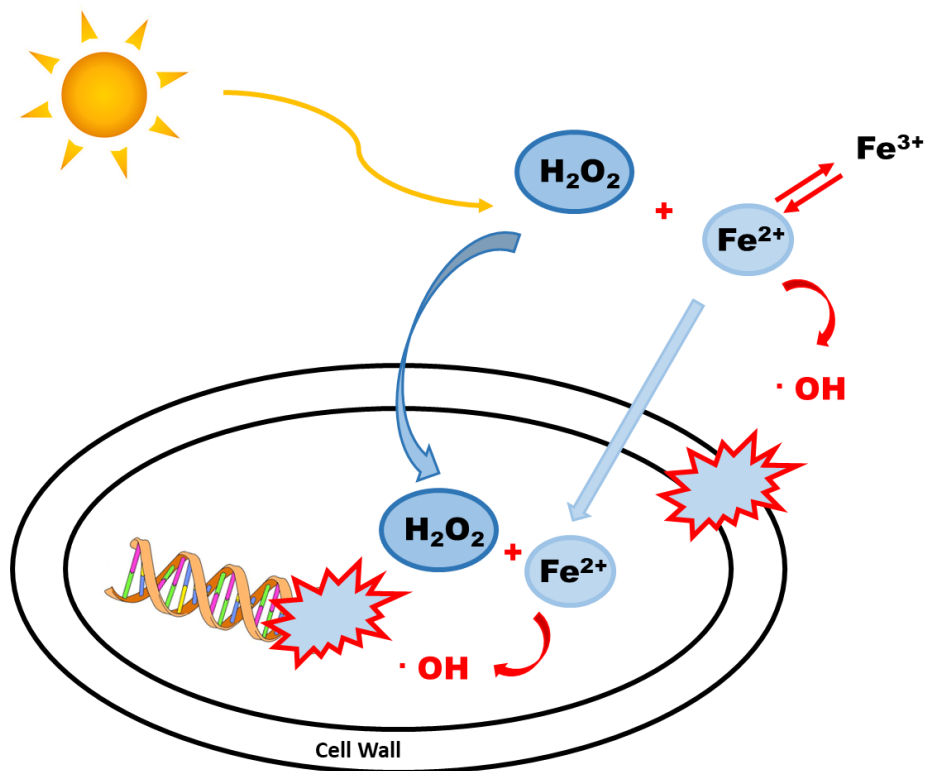
Figure 5.3: *Inactivation of microorganism with Photo-Fenton process.*

5.2.3. Effect of the Main Operating Conditions

Photo-Fenton process is affected by several parameters but, among various factors that influence the disinfection treatment, wavelength and power of the radiation source, Fenton reagents concentrations, pH, temperature and reaction medium composition are the most important. In order to obtain the optimization of Photo-Fenton, effects of the main operating conditions are described along following paragraphs.

5.2.3.1. Effect of Wavelength and Power of the Radiation Source

The type of light source and its power may affect significantly the performance in the Photo-Fenton treatment [52].

UV light wavelength can significantly influence the direct formation of OH radicals species as well as the photo-reduction rate of Fe^{3+} to Fe^{2+}, as shown by Equation (5.9). In particular, the quantum yield of the photo-reduction expressed by Equation (5.9) significantly increases with the decrease of the UV light wavelength [77]. In addition, H_2O_2 does not absorb at all above 320 nm, therefore, using shorter wavelengths is also favoured the dissociation reaction of H_2O_2, expressed by Equation (5.10); this leads to the production of additional OH radicals that promote the total process [64].

In addition to wavelengths, it is also important to consider the power of the radiation used. An increase in the power of the radiation source leads to an increase in disinfection efficiency [77]; in fact, with the increase of light power a faster photo-reduction of Fe^{3+} to Fe^{2+} (Equation 5.9) was obtained, therefore the regeneration rate of Fe^{2+} ions increases. Accordingly with Equations (5.9) and (5.1), the amount of formed OH radicals substantially increases, also giving rise to a higher efficiency of process.

5.2.3.2. Effect of Fenton Reagents Concentration

One of the main step in the Photo-Fenton process is the optimization of the amount of hydrogen peroxide and iron due to their direct effects on disinfection efficiency and operating cost [78, 79]; optimum values are chosen to achieve higher disinfection with lower cost [66].

The presence of both Fenton reagents at their optimal concentration is essential because hydrogen peroxide concentration is directly related to the number of OH radicals generated and the iron amount is directly related to reaction kinetics [80].

In absence of H_2O_2, OH radicals or other reactive oxygen species are not generated; therefore, the application of the only solar radiation or the only addition of iron is inefficient in Photo-Fenton process [81, 82].

On the other end, too high H_2O_2 concentrations reduce the efficiency of Photo-Fenton process [66] due to the decomposition of H_2O_2 in oxygen and water, as shown in Equation (5.11), and to the OH radicals scavenging by H_2O_2 [60] that produces, across Equation (5.12), less reactive O_2H radicals. Subsequently, these radicals react with OH radicals through Equation (5.13), reducing the reaction rate.

$$2H_2O_2 \ \rightarrow \ 2H_2O + \ O_2 \qquad\qquad (5.11)$$

$$H_2O_2 + \cdot OH \rightarrow \ \cdot O_2H \ + \ H_2O \qquad\qquad (5.12)$$

$$\cdot O_2H \ + \cdot OH \ \rightarrow H_2O + \ O_2 \qquad\qquad (5.13)$$
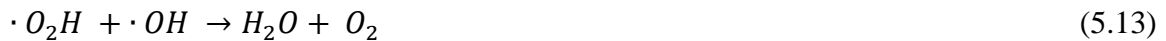
Similarly, the increase in iron concentration contributes to higher disinfection kinetics [52, 83]; this is because iron increases the rate of H_2O_2 decomposition producing an increase in OH radicals formation [52]. However, excess amount of iron lead to some disadvantages, such as scavenging of OH radicals on the base of Equation (5.4), iron sludge formation [84] and turbidity of reaction system causing the lost via scattering of the incident radiation [85], decreasing the efficiency of Photo-Fenton process.

In order to obtain higher disinfection efficiency, optimal ratio of Fenton reagents is fundamental, further to their absolute amounts [66]. The best oxidation efficiency is obtained when both H_2O_2 and Fe^{2+} is overdosed in order to make maximum hydroxyl radicals available for the oxidation of pollutants. This is because excess or shortage of any of these two reagents results in the occurrence of scavenging reactions through Equations (5.3) and (5.4) [51]. The optimal ratio of H_2O_2 and Fe^{2+} is attributed to the type of pollutants present, to matrix effect in complex wastewaters [86] and to the varying determination method for the optimal dosage [54]. The H_2O_2/Fe^{2+}ratio is required to be kept as low as possible to avoid recombination of OH radicals and reduce the final sludge volume [87].

5.2.3.3. Effect of pH

pH is one of the major factors that limits the performance of homogeneous Photo-Fenton processes [88]. There is a general agreement in literature about the optimal pH being close to 3, that is a typical value for the homogeneous Photo-Fenton treatment [89]. The reason why the optimal pH for the Photo-Fenton process is in the range from 2.8 to 3.5 is that generation of species with larger light absorption coefficient and quantum yield for OH radicals production, like $Fe(OH)^{2+}$, are obtained at these pH values [66].

At pH values lower that 2.8 there is a considerable decrease of OH radicals amount due to the scavenger effect by H^+ ions [90] and to the stability of H_2O_2 [91]. In addition, at low pH there is a decrease in the interaction between Fe^{3+} and H_2O_2 [92] that leads to a decrease in the iron catalyst regeneration rate.

Meanwhile, pH values higher than 4 negatively affect the efficiency of the process by a decrease in oxidation potential of OH radicals (that decrement from 2.8 to 1.96 V) [93]. There is also an acceleration of H_2O_2 decomposition in water and oxygen, limiting the OH radicals formation and a deactivation of iron catalyst that precipitated as ferric hydroxide, leading to a decrease in radiation transmission in the process [72].

5.2.3.4. Effect of Temperature

On the base of Arrhenius theory, it is expected that an increase in temperature leads to higher formation rate of OH radicals [94]. Although temperature has a positive effect on Photo-Fenton efficiency because, based on Arrhenius theory of rate constants in relation to temperature, the increase of decontamination due to temperature is relatively small compared to other factors [51]; the optimal temperature for Photo-Fenton process is usually between 20 and 30°C [52]. This is due to the fact that low temperatures result in slower kinetics, while high temperatures promote the thermal decomposition of H_2O_2, causing scavenger effect on OH radicals [63].

5.2.3.5. *Effect of Composition of Reaction Medium*

Besides main operational conditions, there are several other factors that affect the efficiency of Photo-Fenton process as the composition of treated water.

Inorganic ions such as carbonates and bicarbonates, chlorides, fluoride, bromide, phosphate, sulfate and nitrogen compounds like nitrate, nitrite and ammonia may be present in water or generated via degradation process. Some of these ions may affect the oxidation rate of Photo-Fenton reaction.

The entity of the change in reaction kinetic depends on the type of ion and its concentration through one or combination of following effects [66]:

- Formation of Fe^{3+} complexes and decrease in the abundance and the activity of iron species;
- OH radicals scavenging and generation of less reactive radicals;
- Reaction of generated radicals with H_2O_2 that decreases its availability;
- Generation of by-products containing these ions that are in some cases more toxic and recalcitrant.

Several studies were conducted to check the effect of different matrices on Photo-Fenton efficiency. For instance, the presence of carbonates and bicarbonates ions should decrease the process efficiency by their quenching effect on OH radicals through Equations (5.14) and (5.15) [12].

$$\cdot OH + HCO_3^- \rightarrow \cdot CO_3^- + H_2O \qquad (5.14)$$

$$\cdot OH + CO_3^{2-} \rightarrow \cdot CO_3^- + OH^- \qquad (5.15)$$

Similarly, high concentrations of chlorine ions should decrease the Photo-Fenton efficiency through the formation of chlorine-iron complexes and through the scavenger effect on OH radicals, based on Equation (5.16) [95, 96]. The presence of chlorine ions can lead also to the formation of other radical species with a lower oxidation potential than OH radicals, accordingly with Equations (5.17)-(5.20) [97], increasing the Photo-Fenton efficiency due to the active participation of these additional radical species in disinfection [98, 99].

$$\cdot OH + Cl^- \rightarrow \cdot ClOH^- \qquad (5.16)$$

$$\cdot ClOH^- + H^+ \rightarrow \cdot Cl + H_2O \qquad (5.17)$$

$$\cdot Cl + Cl^- \rightarrow \cdot Cl_2^- \qquad (5.18)$$

$$\cdot Cl \ + H_2O_2 \ \rightarrow \ \cdot O_2H \ + \ Cl^- \ + \ H^+ \tag{5.19}$$

$$\cdot Cl_2^- \ + \ \cdot O_2H \ \ \rightarrow \ O_2 + H^+ + 2Cl^- \tag{5.20}$$
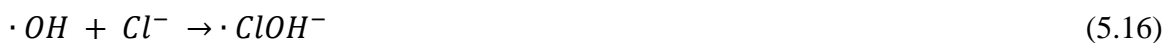
Also the presence of sulphate ions generally causes a quenching effect, as reported in Equation (5.21). Despite sulphate ions act as scavenger for OH radicals, in water and in presence of H_2O_2, the SO_4^- radicals formed by Equation (5.21) lead to the additional generation of OH radicals and SO_4^{2-} ions, as shown in Equations (5.22) and (5.23) increasing the Photo-Fenton efficiency.[100].

$$SO_4^{2-} + \cdot OH \ \rightarrow \cdot SO_4^- \ + \ OH^- \tag{5.21}$$

$$\cdot SO_4^- \ + \ H_2O \ \rightarrow \ H^+ + \ SO_4^{2-} + \ \cdot OH \tag{5.22}$$

$$\cdot SO_4^- \ + \ H_2O_2 \ \rightarrow \ H^+ + \ SO_4^{2-} + \ \cdot OH_2 \tag{5.23}$$

The presence of nitrogen compounds, on the other hand, generally leads to an increase in the efficiency of the process. The composition of nitrogen compounds is a dynamic process, changing during the photo-Fenton process, as it was reported by Equation (5.24) [101]:

$$NH_4^+ \ \leftrightarrow \ NH_3 + \cdot OH \ \rightarrow \ NH_2OH \ \rightarrow NOH \ \rightarrow NO \ \rightarrow \ NO_2^- \ \leftrightarrow \ NO_3^- \tag{5.24}$$
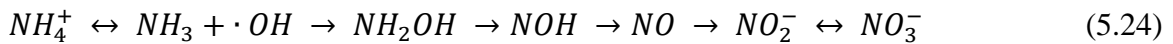
NO_3^- and NO_2^- ions formed by Equation 5.24 play a significant role in Photo-Fenton process because they are able to form additional OH radicals that can contribute to disinfection [102]. Reactions of these ions in aqueous solution under the effect of solar radiation are reported in Equations (5.25) and (5.26) [103].

$$NO_3^- \ + \ H_2O + hv \ \rightarrow \ NO_2^- \ + \ OH^- + \cdot OH \tag{5.25}$$

$$NO_2^- \ + \ H_2O + hv \ \rightarrow NO + \ OH^- + \cdot OH \tag{5.26}$$

Finally, the presence of high concentrations of Dissolved Organic Matter (DOM) decreases the degradation efficacy of Photo-Fenton, especially if contaminants are at lower concentrations than DOM [53, 104]. This is because DOM acts as OH radicals scavenger and reduces the amount of light penetration in the solution [66].

However, at low concentration, UV light absorption by DOM promote the triplet state which can be deactivated in several ways, including a reaction with oxygen to form singlet oxygen, as shown by Equations (5.27) and (5.28).

$$DOM + hv \ \rightarrow \ ^1DOM \ \rightarrow \ ^3DOM^* \tag{5.27}$$

$$^3DOM^* + \ O_2 \ \rightarrow DOM + \ ^1O_2 \tag{5.28}$$

Singlet oxygen can react forming peroxidation products that interact with water contaminants increasing the efficiency of Photo-Fenton process [105]. In presence of iron in water containing DOM, the generation of Fe^{3+}–DOM species occurred showing higher light absorbance and quantum yields due to ligand to metal charge transfer as shows in Equation (5.29), contributing in bacteria inactivation [106].

$$Fe^{3+} - DOM + hv \ \rightarrow \ Fe^{2+} + \ DOM_{OX}^+ \tag{5.29}$$

References

[1] M. Agulló-Barceló, M. I. Polo-López, F. Lucena, J. Jofre and P. Fernández-Ibanez, *Appl. Catal. B: Environ.*, 2013, 136–137, 341–350.

[2] K. G. McGuigan, R. M. Conroy, H. J. Mosler, M. du Preez, E. Ubomba-Jaswa and P. Fernandez-Ibanez, *J. Hazard. Mater.*, 2012, 235–236, 29–46.

[3] A. Carratalà, A. D. Calado, M. J. Mattle, R. Meierhofer, S. Luzi and T. Kohn, *Appl. Environ. Microbiol.*, 2016, 82, 279–288.

[4] C. V. Chrysikopoulos, I. D. Manariotis and V. I. Syngouna, *Colloids Surf., B*, 2013, 107, 174–179.

[5] H. Gómez-Couso, F. Méndez-Hermida, J. A. Castro-Hermida and E. Ares-Mazás, *Vet. Parasitol.*, 2005, 133, 13–18.

[6] S.C. Weir, N. J. Pokorny, R. A. Carreno, J. T. Trevors and H. Lee, *Appl. Environ. Microbiol.*, 2002, 68, 2576–2579.

[7] S. Giannakis, S. Liu, A. Carratalà, S. Rtimi, M. Bensimon and C. Pulgarin, *Appl. Catal. B: Environ.*, 2017, 204, 156–166.

[8] M. Boyle, C. Sichel, P. Fernandez-Ibanez, G. B. Arias-Quiroz, M. Iriarte-Puna, A. Mercado, E. Ubomba-Jaswa and K. G. McGuigan, *Appl. Environ. Microbiol.*, 2008, 74, 2997–3001.

[9] S. Giannakis, A. I. Merino Gamo, E. Darakas, A. Escalas-Cañellas and C. Pulgarin, *Chem. Eng. J.*, 2014, 253, 366–376.

[10] A. G. Rincón and C. Pulgarin, *Appl. Catal. B: Environ.*, 2006, 63, 222–231.

[11] E. Ubomba-Jaswa, P. Fernandez-Ibanez, C. Navntoft, M. I. Polo-Lopez and K. G. McGuigan, *J. Chem. Technol. Biotechnol.*, 2010, 85, 1028–1037.

[12] J. Ndounla and C. Pulgarin, *Environ. Sci. Pollut. Res.*, 2015, 22, 17082–17094.

[13] D. Spuhler, J. A. Rengifo-Herrera and C. Pulgarin, *Appl. Catal. B: Environ.*, 2010, 96, 126–141.

[14] G. Ruppert, R. Bauer and G. Heisler, *J. Photochem. Photobiol., A: Chem.*, 1993, 73, 75–18.

[15] J. Mwabi, F. Adeyemo, T. Mahlangu, B. Mamba, B. Brouckaert, C. Swartz, G. Offringa, L. Mpenyana-Monyatsi and M. Momba, *Phys. Chem. Earth Parts A/B/C*, 2011, 36, 1120–1128.

[16] V. Balzani, P. Ceroni and A. Juris, *Photochemistry and photophysics: concepts, research, applications*, Wiley-VCH, 2014, ISBN: 978-3-527-33479-7.

[17] M. B. Fisher, M. Iriarte and K. L. Nelson, *Water Res.*, 2012, 46, 1745–1754.

[18] A. Downes and T. P. Blunt, *Nature*, 1877, 16, 402–418.

[19] A. Acra, Y. Karahagopian, Z. Raffoul, and R. Dajani, *The Lancet*, 1980, 2, 1257–1258.

[20] A. Acra, Z. Raffoul, and Y. Karahagopian, *Solar Disinfection of Drinking Water and Oral Rehydration Solutions*, UNICEF, Paris, France, 1984.

[21] P. S. M. Dunlop, M. Ciavola, L. Rizzo and J. A. Byrne, *Chemosphere*, 2011, 85, 1160–1166.

[22] D. C. Walker, S. V. Len and B. Sheehan, *Appl. Environ. Microbiol.*, 2004, 70, 2545–2550.

[23] S. C. Kehoe, T. M. Joyce, P. Ibrahim, J. B. Gillespie, R. A. Shahar and K. G. McGuigan, *Water Res.*, 2001, 35, 1061–1065.

[24] S. K. Mani, R. Kanjur, I. S. Bright Singh and R. H. Reed, *Water Res.*, 2006, 40, 721–727.

[25] B. Sommer, A. Marino, Y. Solarte, M. L. Salas, C. Dierolf, C. Valiente, D. Mora, R. Rechsteiner, P. Setter, W. Wirojanagud, H. Ajarmeh, A. AlHassan and M. Wegelin, *J. Water SRT – Aqua*, 1997, 46, 127–137.

[26] R.H. Reed, *Lett. Appl. Microbiol.*, 1997, 24, 276–280.

[27] R.H. Reed, *Adv. Appl. Microbiol.*, 2004, 54, 333–365.

[28] J. A. Byrne, P. A. Fernandez-Ibanez, P. S. M. Dunlop, D. M. A. Alrousan and J. W. J. *Int. J. Photoenergy.*, 2011, 12, 798051.

[29] E. C. Friedberg, *Nature*, 2003, 421, 436–440.

[30] E. J. Wurtmann and S. L. Wolin, *Crit. Rev. Biochem. Mol. Biol.*, 2009, 44, 34–49.

[31] C. Fimognari, P. Sestili, M. Lenzi, A. Bucchini, G. Cantelli-Forti and P. Hrelia, *Mut. Res.*, 2008, 648, 15–22.

[32] S. Matallana-Surget and R. Wattiez, *Proteomes.*, 2013, 1, 70–86.

[33] J. Cadet, E. Sage and T. Douki, *Mut. Res.*, 2005, 571, 3–17.

[34] T. Douki, *Photochem. Photobiol. Sci.* 2013, 12, 1286–1302.

[35] M. Berney, H. U. Weilenmann, J. Ihssen, C. Bassin and T. Egli, *Appl. Environ. Microbiol.*, 2006, 72, 2586–2593.

[36] K. G. McGuigan, T. M. Joyce, R. M. Conroy, J. B. Gillespie and M. Elmore-Meegan, *J. Appl. Microbiol.*, 1998, 84,1138–1148.

[37] M. Wegelin, S. Canonica, K. Mechsner, T. Fleischmann, F. Pesaro and A. Metzler, *J. Water SRT – Aqua*, 1994, 43, 154–169.

[38] E. F. Duffy, F. Al Touati, S. C. Kehoe, O. A. McLoughlin, L. W. Gill, W. Gernjak, I. Oller, M. I. Maldonado, S. Malato, J. Cassidy, R. H. Reed and K. G. McGuigan, *Sol. Energy*, 2004, 77, 649–655.

[39] R. B. Webb and M. S. Brown, *Photochem. Photobiol.*, 1979, 29, 407–409.

[40] S. H. Moss and K. C. Smith, *Photochem. Photobiol.*, 1981, 33, 203–210.

[41] R. Khaengraeng and R.H. Reed, *J. Appl. Microbiol.*, 2005, 99, 39–50.

[42] C. Sichel, J. Blanco, S. Malato and P. Fernández-Ibánez, *J. Photochem. Photobiol. A.*, 2007, 189, 139–246.

[43] M. I. Polo-López, I. García-Fernández, I. Oller and P. Fernández-Ibánez, *Photochem. Photobiol. Sci.*, 2011, 10, 381–388.

[44] A. G. Rincón and C. Pulgarin, *Appl. Catal. B: Environ.*, 2004, 51, 283–302.

[45] S. Gutiérrez-Alfaro, A. Acevedo, M. Figueredo, M. Saladin and M. A Manzano, *J. Chem. Technol. Biotechnol.*,2017, 92, 298–304

[46] S. K. Lee, M. Sheridan and A. Mills, *Chem. Mater.*, 2005, 17, 2744–2751.

[47] A. Mills, S. K. Lee and M. Sheridan, *Analyst*, 2005, 130, 1046–1051.

[48] M. Tanveer and G. T. Guyer, *J. Renew. Sustain. Energy*, 2013, 24, 534–543.

[49] K. Lawrie, A. Mills, M. Figueredo-Fernández, S. Gutiérrez-Alfaro, M. Manzano and M. Saladin, *Sens. Actuators. B. Chem.*, 2015, 208, 608–615.

[50] M. Marjanovic, S. Giannakis, D. Grandjean, L. F. de Alencastro and C. Pulgarin, *Water Res.*,2018, 140, 220–231.

[51] M. Umar, H. A. Aziz and M. S. Yusoff, *Waste Manage.*, 2010, 30, 2113–2121.

[52] F. Haber and J. Weiss, *Proc. R. Soc. Lond.*, 1934, 147, 332.

[53] J. J. Pignatello, E. Oliveros and A. MacKay, *Crit. Rev. Environ. Sci. Technol.*, 2006, 36, 1–84.

[54] Y. Deng and J. D. Englehardt, *Water Res.*, 2006, 40, 3683–3694.

[55] T. Rigg, W. Taylor and J. Weiss, *J. Chem. Phys.*, 1954, 22, 575–577.

[56] C. Walling and A. Goosen, *J. Am. Chem. Soc.*, 1973, 95, 2987–2991.

[57] G. V. Buxton and C. L. Greenstock, *J. Phys. Chem. Ref. Data*, 1988, 17, 513–886.

[58] J. De Laat and H. Gallard, *Environ.Sci. Technol.*,1999, 33, 2726–2732.

[59] B. H. J. Bielski, D. E. Cabelli, R. L. Arudi and A. B. Ross, *J. Phys. Chem. Ref. Data*, 1985, 14, 1041–1051.

[60] R. Andreozzi, V. Caprio, A. Insola and R. Marotta, *Catal. Today*, 1999, 53, 51.

[61] M. Pera-Titus, V. García-Molina, M.A. Banos, J. Giménez and S. Espulgas, *Appl. Catal. B: Environ.*, 2004, 47, 219.

[62] E. G. Garrido-Ramírez, B. K. G. Theng and M. L. Mora, *Appl. Clay Sci.*, 2010, 47,182.

[63] A. C. K. Yip, F. L. Y. Lam and X. Hu, *Ind. Eng. Chem. Res.*, 2005, 44, 7983.

[64] O. S. N. Sum, J. Feng, X. Hu and P. L. Yue, *Top. Catal.*, 2005, 33, 233.

[65] D. Hermosilla, M. Cortijo and C.P. Huang, *Sci. Total Environ.*, 2009, 407, 3473.

[66] S. R. Pouran, A. R. A. Aziz and W. M. A. Wan Daud, *J. Ind. Eng. Chem.*, 2015, 21, 53–69.

[67] M. Punzi, B. Mattiasson and M. Jonstrup, *J. Photochem. Photobiol., A. Chem.*, 2012, 248, 30.

[68] F. Mendez-Arriaga, S. Esplugas and J. Gimenez, *Water Res.*, 2010, 44, 589.

[69] R. Gonzalez-Olmos, M. J. Martin, A. Georgi, F. D. Kopinke, I. Oller and S. Malato, *Appl. Catal., B.: Env.*, 2012, 125, 51.

[70] S. R. Pouran, A. R. A. Aziz and W. M. A. Wan Daud, *J. Clean. Prod.*, 2014, 64, 24.

[71] E. Casbeer, V. K. Sharma and X. Z. Li, *Sep. Purif. Technol.*, 2012, 87, 1.

[72] B. C. Faust and J. Hoigne, *Atmos. Environ.*, 1990, 24, 79.

[73] I. Garcıa-Fernandez, M. I. Polo-Lopez, I. Oller and P. Fernandez-Ibanez, *Appl. Catal., B.: Env.*, 2012, 20, 121–122.

[74] M. I. Polo-Lopez, I. Garcıa-Fernandez, T. Velegraki, A. Katsoni, I. Oller, D. Mantzavinos and P. Fernandez-Ibanez, *Appl. Catal., B.: Env.*, 2012, 545, 111–112.

[75] E. Ortega-Gomez, B. E. Garcıa, M. M. Ballesteros Martın, P. Fernandez Ibanez and J. A. Sanchez Perez, *Catal. Today.*, 2013, 209, 195.

[76] P. Karaolia, I. Michael, I. Garcıa-Fernandez, A. Aguera, S. Malato, P. Fernandez-Ibanez and D. Fatta-Kassinos, *Sci. Total Environ.*, 2014, 19, 468–469.

[77] J. Feng, X. Hu, P. L. Yue, H. Y. Zhu and G. Q. Lu, *Water Res.*, 2003, 37, 3776.

[78] O. Primo, M. J. Rivero and I. Ortiz, *J. Hazard. Mater.*, 2008, 153, 834.

[79] G. C. Heng, E. S. Elmolla and M. Chaudhuri, *J. Nat. Env. Poll. Techn.*, 2012, 11, 65.

[80] E. Chamarro, A. Marco and S. Espulgas, *Water Res.*, 2000, 35, 1047.

[81] J. M. Monteagudo, A. Duran, M. Aguirre and I. San Martın, *J. Hazard. Mater.*, 2011, 185, 131.

[82] J. M. Monteagudo, A. Duran, I. S. Martin and M. Aguirre, *Appl. Catal., B.: Env.*, 2010, 96, 486.

[83] C. Zaror, C. Segura, H. Mansilla, M. Mondaca and P. Gonzalez, *Water Sci. Technol.*, 2008, 58, 259.

[84] P. R. Gogate and A. B. Pandit, *Adv. Environ. Res.*, 2004, 8, 501.

[85] B. Iurascu, I. Siminiceanu, D. Vione, M. A. Vicente and A. Gil, *Water Res.*, 2009, 43, 1313.

[86] W. Z. Tang and C. P. Huang, *Environ. Technol.*, 1997, 18, 13–23.

[87] Y. K. Kim and I. R. Huh, *Environ. Eng. Sci.*, 1997, 14, 73–79.

[88] H. Katsumata, S. Kaneco, T. Suzuki, K. Ohta and Y. Yobiko, *Chem. Eng. J.*, 2005, 108, 269.

[89] J. Feng, X. Hu and P. L. Yue, *Water Res.*, 2006, 40, 641.

[90] W. Z. Tang and C. P. Huang, *Environ. Technol.*, 1996, 17, 1371.

[91] C. Y. Chen, P. S. Wu and Y. C. Chung, *Bioresour. Technol.*, 2009, 100, 4531.

[92] J. J. Pignatello, *Environ. Sci. Technol.*, 1992, 26, 944.

[93] S. M. Kim and A. Vogelpohl, *Chem. Eng. Technol.*, 1998, 21, 187.

[94] A. Zapata, I. Oller, L. Rizzo, S. Hilgert, M. I. Maldonado, J. A. Sanchez-Perez and S. Malato, *Appl. Catal., B.: Env.*, 2010, 97, 292.

[95] A. Machulek Jr., J. F. Moraes, C. Vautier-Giongo, C. A. Silverio, L. C. Friedrich, C. A. O. Nascimento, M. C. Gonzalez and F. Quina, *Environ. Sci. Technol.*, 2007, 41, 8459–8463.

[96] C. Sirtori, A. Zapata, W. Gernjak, S. Malato, A. Lopez and A. Aguera, *Water Res.*, 2011, 45, 1736.

[97] L. Prieto-Rodrıguez, I. Oller, A. Zapata, A. Aguera and S. Malato, *Catal. Today.*, 2011, 161, 247.

[98] L. Gomathi Devi, C. Munikrishnappa, B. Nagaraj and K. Eraiah Rajashekhar, *J. Mol. Catal. A: Chem.*, 2013, 374–375, 125–131.

[99] M. M. Mico, J. Bacardit, J. Malfeito and C. Sans, *Appl. Catal., B.: Env.*, 2013, 162, 132–133.

[100] F. Ghanbari and M. Moradi, *Chem. Eng. J.*, 2017, 310, 41–62.

[101] S. Giannakis, M. I. Polo López, D. Spuhler, J. A. Sánchez Pérez, P. Fernández Ibánez and C. Pulgarin, *Appl. Catal., B.: Env.*, 2016, 199, 199–223.

[102] L. A. Tercero Espinoza, M. Neamtu and F. H. Frimmel, *Water Res.*, 2007, 41, 4479–4487.

[103] J. C. Fanning, *Coord. Chem. Rev.*, 2000, 199, 159–179.

[104] I. Michael, E. Hapeshi, C. Michael, A. R. Varela, S. Kyriakou, C. M. Manaia and D. Fatta-Kassinos, *Water Res.*, 2012, 46, 5621.

[105] D. Rubio, E. Nebot, J. F. Casanueva and C. Pulgarin, *Water Res.*, 2013, 47, 6367–6379.

[106] S. Giannakis, *Environ. Sci. Pollut. Res. Int.*, 2018, 25, 27676–27692.

CHAPTER 6. WHICH IONS HOLD PHOTOCHEMICAL IMPLICATIONS DURING SODIS AND PHOTO-FENTON INACTIVATION OF BACTERIA IN NATURAL WATER? A SYSTEMATIC ASSESSMENT

Abstract

The effect of the presence of various inorganic ions, like HCO_3^-, NO_3^-, NO_2^-, Cl^-, SO_4^{2-} and NH_4^+, in different concentrations and at near neutral pH on inactivation of E. Coli K12 with SODIS and Photo-Fenton processes is discussed in detail.

These inorganic ions, individually or in combination with each other, can act as scavenger of OH radicals, otherwise can produce additional OH radicals or other active radical species, decreasing or improving the efficiency of both SODIS and Photo-Fenton processes.

In addition, these ions in presence of natural organic matter should lead to an increase in disinfection kinetics for both processes because natural organic matter act as photosensitizer leading to the production of reactive oxygen species; for this, the combination of various inorganic ions and natural organic matter is subsequently studied.

In all experiment, the evolution of some physicochemical parameters of water, like HCO_3^-, NO_3^-, NO_2^-, Cl^-, SO_4^{2-} and NH_4^+ concentration and pH evolution was monitored during treatments.

6.1. Introduction

Water sources contain a large amount of Natural Organic Matter (NOM) and inorganic ions, like HCO_3^-, NO_3^-, NO_2^-, Cl^-, SO_4^{2-} and NH_4^+ ions, naturally present in water sources or introduced in natural cycles by agricultural, domestic and industrial activities. The mean chemical composition of water sources is reported in Table 6.1 [1 - 4].

Table 6.1: *Mean chemical composition of water sources.*

Ions	Lake Water (mg L^{-1})	River Water (mg L^{-1})	Groundwater (mg L^{-1})	Harvested rainwater (mg L-1)
HCO_3^-	$10 - 110$	$20 - 100$	$20 - 800$	$5 - 150$
NO_3^-	$0.1 - 4$	$0.05 - 4$	$0.05 - 60$	$5 - 800$
NO_2^-	< 0.4	< 0.4	< 1	< 0.15
Cl^-	$2 - 15$	$4 - 12$	$2 - 700$	$10 - 4000$
SO_4^{2-}	$2 - 250$	$0 - 230$	$0 - 630$	$10 - 5000$
NH_4^+	$0.003 - 0.8$	< 0.2	$0.001 - 3$	$1 - 300$

It is known that inorganic ions naturally present in water sources can be involved in the absorption efficiency of incident radiation, in the scavenger effect of OH radicals with the formation of less reactive inorganic radicals, in the production of additional reactive radicals when photolyzed and in the complexation reactions with Fe^{2+} or Fe^{3+} which can affect the distribution and the reactivity of the iron species [5]. For these reasons, depending on their concentrations, SODIS and Photo-Fenton processes can be inhibited or promoted in varying degrees by inorganic ions [6].

In addition, NOM acts sometimes as photosensitizer for a large variety of chemical reactions that are produced by energy transfer, singlet oxygen and radical species generation, leading to the production of ROS and increasing the efficiency of both SODIS and Photo-Fenton processes [7].

6.1.1. Aim of the Work

The main goal of this work is to study the effect of concentrations of varied inorganic ions, like HCO_3^-, NO_3^-, NO_2^-, Cl^-, SO_4^{2-} and NH_4^+, in absence and in presence of NOM, on E. Coli inactivation by SODIS and Photo-Fenton processes. To reach this aim, disinfection experiments and evolution of pH and concentrations during both processes were performed and compared with the same in absence of these ions, in order to obtain kinetics information about the increase or decrease in efficiency.

6.2. Experimental

6.2.1. Reagents and Materials

Because the effect of Na^+ as counter ion is negligible due to its harmless for E. Coli, sodium salts as source of ions were used; compounds tested as source of ions were $NaHCO_3$, $NaNO_3$, $NaNO_2$, NaCl, Na_2SO_4 and $(NH_4)_2SO_4$ and were purchased by Sigma-Aldrich. Aqueous solutions of salts, in appropriate concentrations, were prepared in Milli-Q water.

$FeSO_4 \cdot 7H_2O$ and H_2O_2 30% w/v (Sigma-Aldrich) was used to prepare the Photo-Fenton reagent.

6.2.2. Photochemical Experiments

Solar irradiation with intensity of 620 W/m^2 was simulated by a Heraeus Solarbox (Hanau, Germany). Irradiation experiments at 350 rpm of agitation and at room temperature were performed by testing the effects of HCO_3^- from 5 to 100 mg L^{-1}, NO_3^- from 1 to 50 mg L^{-1}, NO_2^- from 0.01 to 5 mg L^{-1}, Cl^- from 1 to 500 mg L^{-1}, SO_4^{2-} from 10 to 500 mg L^{-1} and NH_4^+ from 0.1 to 10 mg L^{-1} on bacteria. In order to define the bacterial survival in the presence of maximum concentrations of these ions, control experiments after 240 minutes in dark conditions were performed. In Photo-Fenton experiments, the concentration of Fe^{2+} and H_2O_2 solutions were 1 mg L^{-1} and 10 mg L^{-1} respectively; for reproducibility, each experiment was carried out in duplicate.

The test took place in Pyrex glass reactors with Milli-Q water at near neutral starting pH containing 100 mL of E. coli solution with concentration of 10^6 Colony Forming Units per millilitre (CFU/mL). Before every experiments, reactors were sterilized by autoclaving and after each experiment, they were washed using acid to ensure iron removal, with ethanol to remove any other contaminant and finally with deionized water in abundant amounts.

6.2.3. Bacterial Strain and Growth Media

The bacterial strain used in this study was E. Coli K-12, a non-pathogenic wild-type strain, which can be handled with little genetic manipulation; E. Coli strain storage is ensured in cryo-vials containing 20% of glycerol at -20°C. Bacterial pre-cultures were obtained by spreading 20 µL of the

strain into Plate Count Agar (PCA; Merck) followed by 24 h of incubation at 37°C (Heraeus Instruments). A grown colony was then sampled and spread again on a new PCA plate for concentration purposes. After more 24 h of incubation at 37°C, the master plate was ready and stored at 4 °C; due to the uncertainty of the dispersion method, the process was done in duplicate.

In order to prepare bacterial stock solution, a colony of bacteria was extracted from master plate and inoculated into 5 mL of Luria-Bertani (LB) Broth. After a strong mixing by a vortex machine for 1 or 2 minutes, it was incubated at 37°C temperature controlled room for 8 h and constantly agitated by circular movement at 750 rpm. After 8 h, 2.5 mL of sample were diluted in 250 mL of LB Broth and incubated for 15 h in the same room to ensure that stationary physiological phase was reached. 25 mL of this bacterial sample were separated during the stationary growth phase by centrifugation and were washed with saline solution 3 times. Washing takes place in 4°C centrifuge (Hermle Z 323 K, Renggli Laboratory Systems), at 5000 rpm for 15 minutes the first time and 5 minutes the remaining two, with 10 mL of saline solution. After the final wash, at the bacterial pellet were added 25 mL of clean saline solution. This procedure resulted in a bacterial pellet of approximately 10^8 CFU/mL.

Specifically, LB consisted of 10 g L^{-1} tryptone, 10 g L^{-1} NaCl and 5 g L^{-1} yeast extract in Milli-Q water. The saline solution was a sterile NaCl/KCl solution (8 g L^{-1} NaCl and 0.8 g L^{-1} KCl at pH 7–7.5).

6.2.4. Sampling and Bacterial Enumeration

Samples of 1 mL, in sterile plastic Eppendorf vials to ensure their sterile preservation, was made from the body of the reactor under stirring. In order to obtain information about disinfection kinetics, sampling was performed at time intervals of 0, 30, 60, 90, 120, 180 and 240 minutes for SODIS and at time intervals of 0, 20, 40, 60, 90 and 120 minutes for Photo-Fenton.

Experiments were conducted in duplicate and using serial dilutions, to achieve measurable bacterial count on the plates; the optimal colony counts in this method are among 15–150 CFU. The total inactivation was considered achieved when none of the bacteria colony were observed in plates after treatments. The spread plate technique was performed on PCA, contained in plastic sterile Petri dishes injecting drop by drop 100 µL of samples. The detection limit is 1 CFU/mL for undiluted samples and 10 CFU/mL for diluted ones [8]. The incubation period was 18-24 hours at 37°C.

6.2.5. Data Treatment

In order to model the bacterial response under the solar light stress, the GInaFiT freeware add-on for Microsoft Excel was used [9]. Between the models tested and fit curves, a Shoulder log-linear was used, as it has yielded the highest R^2, and its calculation was possible for all cases. The Shoulder log-linear model was formulated as shown in Equation (6.1) [10].

$$log_{10}(N) = log_{10}(N_0) - k * \frac{t - t_s}{\ln(10)} - log_{10}[1 + (\exp(k * t_s) - 1) * \exp(-k * t)] \qquad (6.1)$$

where:

N is the bacterial population at any given time (CFU/mL).

N_0 is the initial bacterial population (CFU/mL).

t is the investigated time (s).

t_s is the length of the shoulder period or threshold time to observe inactivation

k is the rate of the inactivation.

6.2.6. Chemical and Analytical Methods

According to the standard methods for the examination of water [11], NO_3^- analysis (Standard Method 4500 - NO_3^- B) were carried out using a Shimadzu UV-1800 spectrophotometer with the minimum detectable NO_3^- concentration of 0.5 mg L^{-1} while HCO_3^-, expressed as alkalinity (Standard Method 2320 B), was measured by potentiometric titration with H_2SO_4. NH_4^+ and SO_4^{2-} were analysed by HACH DR 3900 spectrophotometer: NH_4^+ was measured using LCK 305 Ammonium-Nitrogen cuvettes (minimum detectable NH_4^+ concentration of 1 mg L^{-1}) while SO_4^{2-} was measured using LCK 153 Sulfate cuvettes (minimum detectable SO_4^{2-} concentration of 40 mg L^{-1}). NO_2^- and Cl^- were analysed by Quantofix semi quantitative strips (Macherey-Nagel, Germany); NO_2^- was determined with Quantofix nitrite 3000 (minimum detectable NO_2^- concentration of 0.1 mg L^{-1}) while Cl^- was determined with Quantofix chloride 91321 (minimum detectable Cl^- concentration of 500 mg L^{-1}). The pH evolution during treatments were recorded using a pH-meter Mettler Toledo.

6.3. Results and Discussions

6.3.1. HCO_3^- Effects

Carbonate and bicarbonate ions are the main forms of carbonate compounds in water; most of HCO_3^- and CO_3^{2-} ions are coming from the dissolution of carbonate minerals, the decomposition of organic matter, the respiration of aquatic animals and the exchange of carbon cycle. The content of these ions could indicate the local geochemical environment [12]. Due to its high solubility, HCO_3^- is widely distributed in natural water (see Table 6.1), in biological systems and constitutes the main biological buffer; it presents major solubility at pH 7.0–9.0, while gives the formation of less soluble Na_2CO_3 or carbonic acid above or below this range.

Table 6.2 reports the pseudo first order kinetic constants values calculated for both SODIS and Photo-Fenton processes for all tested HCO_3^- concentrations that are graphically showed in Figure 6.1 (a), while Figure 6.1 (b) shows the most significant disinfection graphs for both processes.

Results demonstrated that, for SODIS treatment, there are not significant changes in reaction kinetics using low HCO_3^- concentrations, up to 50 mg L^{-1}, while a decrease in the inactivation rate at high concentrations has been observed. For Photo-Fenton process, an increase in the disinfection kinetics at low HCO_3^- concentration, up to 10 mg L^{-1}, and a decrease at higher concentrations has been obtained.

Table 6.2: *Kinetic constants values with different HCO_3^- concentration.*

	SODIS		Photo-Fenton	
HCO_3^-	*k*	STD	*k*	STD
mg L^{-1}	min^{-1}		min^{-1}	
0	0.0299	0.012	0.0614	0.010
5	0.0304	0.010	0.0929	0.020
10	0.0311	0.010	0.1354	0.010
50	0.0308	0.010	0.0407	0.010
100	0.0259	0.010	0.0482	0.020
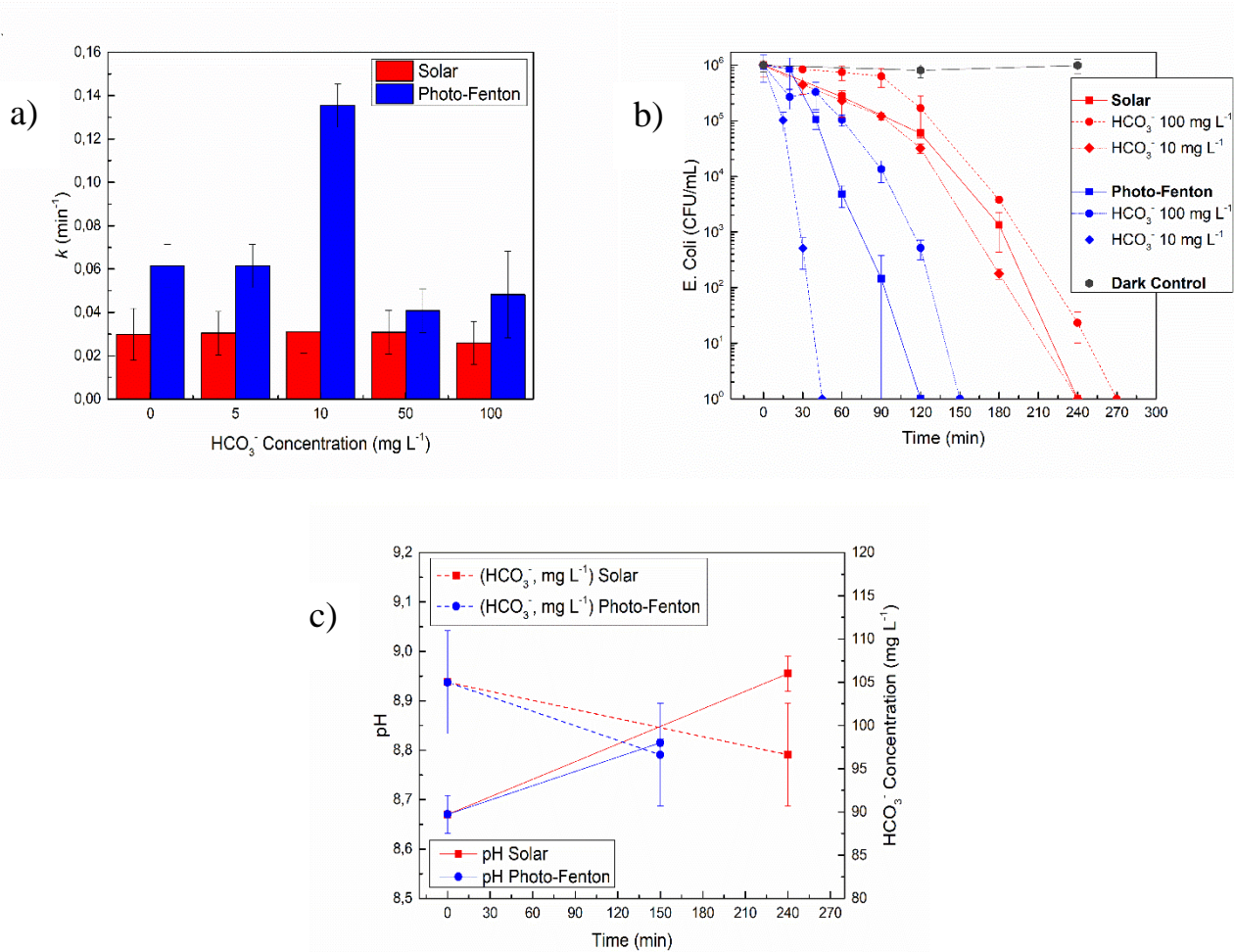
Figure 6.1: *Kinetic constants values with different HCO_3^- concentrations for SODIS and Photo-Fenton processes (a). Disinfection experiments with HCO_3^- (b). Changes of pH and HCO_3^- concentration during processes (initial HCO_3^- concentration of 100 mg L^{-1}) (c).*

Figure 6.1 (c) shows pH and HCO_3^- concentration changes during both SODIS and Photo Fenton processes exhibiting, with 100 mg L^{-1} of HCO_3^-, a basic pH of reaction systems that increases during both processes with a simultaneous decrease in HCO_3^- concentrations. Instead, at 10 mg L^{-1} of HCO_3^-, the pH of reaction systems was near neutral and showed no shift respect to the same processes in absence of HCO_3^- ions and, at the same time, HCO_3^- concentrations remained almost unchanged.

Negative effect of HCO_3^- on SODIS derived from light absorption induced by this ion, which limits the amount of light reaching bacteria in water [13]. In addition, in water with a pH equal or greater than 8.3, HCO_3^- generates CO_3^{2-} as confirmed by trends in pH and concentration for both processes; each of these ions influences Photo-Fenton process due to quenching effect on OH radicals, offering a protective effect on bacteria [6]. In fact, as shown in Equations (6.2) and (6.3), HCO_3^- and CO_3^{2-} react

with OH radicals to produce less reactive CO_3^- radicals, with a contemporary increase in pH [14], that lead to a consequent decrease in the efficiency due to decrease of OH radicals in reaction systems.

$$\cdot OH + HCO_3^- \rightarrow \cdot CO_3^- + H_2O \tag{6.2}$$

$$\cdot OH + CO_3^{2-} \rightarrow \cdot CO_3^- + OH^- \tag{6.3}$$

Similarly, in the presence of H_2O_2 is possible the formation of well-known two-electron oxidant peroxymonocarbonate (HCO_4^-) through Equation (6.4) [15] that it is known to proceed rapidly at near neutral pH in aqueous solutions. HCO_4^- is more reactive than H_2O_2 (up to 500 times) in different reactions depending on the substrate [15] and its role in the H_2O_2 activation has been extensively studied in organic reactions [16, 17] and in the formation of ROS in biology [15, 18]. For these reasons, bicarbonate activated hydrogen peroxide (BAP) systems were proposed in different studies [19] also due to enhance the degradation rates of pollutants by adding trace redox metal ions in the HCO_3^-/H_2O_2 system [20]. In addition, it is also reported that large interest is given to the application of HCO_3^- in combination with certain AOPs for sustainable wastewater treatment [16, 17, 19, 21].

$$H_2O_2 + HCO_3^- \rightarrow H_2O + HCO_4^- \tag{6.4}$$

At low HCO_3^- concentrations, where the pH of reaction systems was near neutral, the conditions were favourable for the formation of HCO_4^- [15] that can give decomposition in the presence of excess H_2O_2 by Equations (6.5) and (6.6) [22] or oxidize specific substrate (S = pollutant or bacteria) by Equation (6.7), regenerating HCO_3^-.

$$HCO_4^- \rightarrow \cdot CO_3^- + OH^- \tag{6.5}$$

$$H_2O_2 + \cdot CO_3^- \rightarrow HCO_3^- + \cdot O_2H \tag{6.6}$$

$$S + HCO_4^- \rightarrow SO + HCO_3^- \tag{6.7}$$

Therefore, lower HCO_3^- concentrations, in the Photo-Fenton process do not act as a scavenger of OH radicals, but catalyse the disinfection process through the formation of HCO_4^- by Equation (6.4), increasing the efficiency of disinfection.

All obtained results with HCO_3^- for SODIS and Photo-Fenton processes are schematized in Figure 6.2.
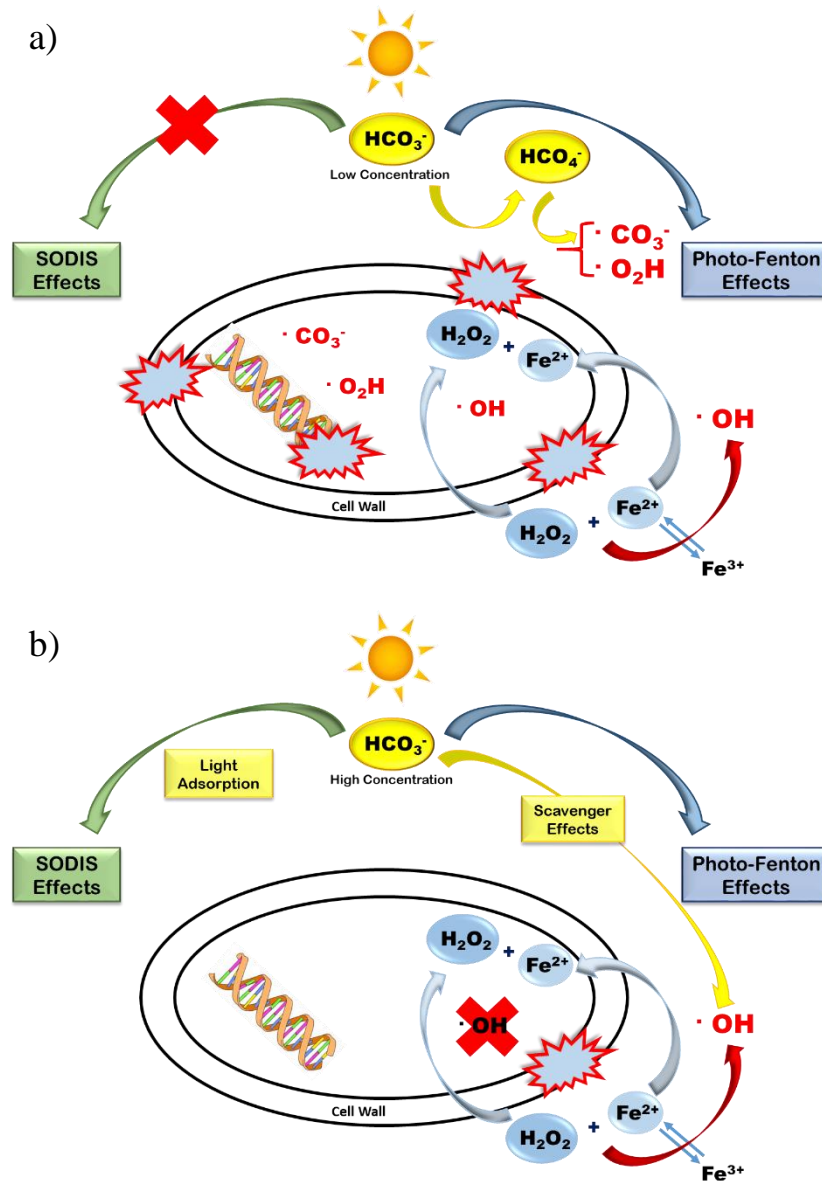
Figure 6.2: *Schematic representation of HCO_3^- effects for SODIS and Photo-Fenton processes. Low HCO_3^- concentration (a). High HCO_3^- concentration (b).*

6.3.2. Cl⁻ Effects

Chlorine is an important chemical in water purification, in disinfectants, in bleach and in mustard gas. In nature, it is only found combined with other elements mainly sodium in the form of common salt. Chlorides make up much of the salt dissolved in the Earth's oceans: about 1.9 % of the mass of seawater is Cl⁻ ions.

Figure 6.3 (a) shows the pseudo first order kinetic constants values calculated for both SODIS and Photo-Fenton processes for all tested Cl⁻ concentrations that are numerically reported in Table 6.3, while Figure 6.3 (b) shows the most significant disinfection graphs for both processes. For both SODIS and Photo-Fenton processes, an increase of disinfection kinetics with all Cl⁻ concentration tested was obtained.

Figure 6.3: *Kinetic constants values with different Cl^- concentrations for SODIS and Photo-Fenton processes (a). Disinfection experiments with Cl^- (b). Changes of Cl^- concentration during processes (initial Cl^- concentration of 1000 mg L⁻¹) (c).*

Table 6.3: *Kinetic constants values with different Cl^- concentration.*

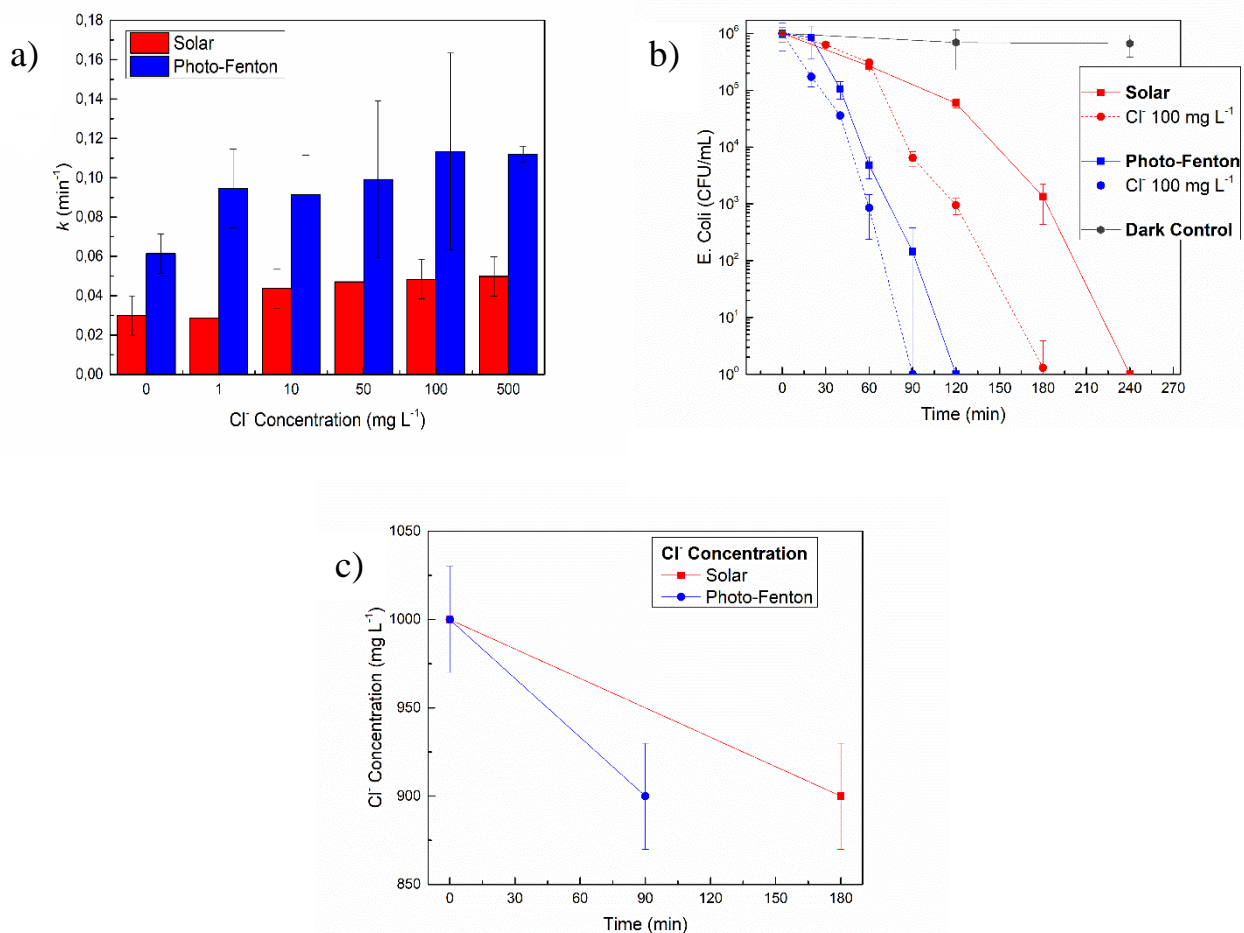|	SODIS		Photo-Fenton	
Cl^-	k	STD	k	STD
mg L^{-1}	min^{-1}		min^{-1}	
0	0.0299	0.012	0.0614	0.010
1	0.0287	0.010	0.0945	0.020
10	0.0437	0.010	0.0916	0.020
50	0.0471	0.010	0.0992	0.040
100	0.0484	0.010	0.1134	0.050
500	0.0498	0.010	0.1118	0.040

The pH of both reaction systems was near neutral and showed no substantial shift during SODIS and Photo-Fenton treatments respect to same processes in absence of Cl^- ion, while a decrease in Cl^- concentration during both processes was observed (Figure 6.3 c).

In SODIS treatment, the use of Cl^- improve the disinfection kinetics with all tested Cl^- concentrations because its absorption of UV-Vis radiation with λ greater than 200 nm increases the rate of singlet oxygen formation [23] that can form peroxidation products, thus increasing the efficiency of disinfection processes [14].

To explain the efficiency increase in Photo-Fenton process it is necessary to consider that Cl^- with Fe^{3+} gives the formation of less reactive $Fe(Cl)^{2+}$ and $FeCl_2^+$ complexes, although $Fe(OH)_2^+$ is still the predominant species at pH 3.0. In absence of any ions at pH 3.0 the reaction is dominated by the photo-reactive $Fe(OH)_2^+$ complex while, in presence of Cl^-, $Fe(Cl)^{2+}$ complex has a higher absorptivity with higher quantum yield of photolysis at 347 nm promoting the formation of Cl radicals by Equation (6.8) [24].

$$Fe(Cl)^{2+} + hv \rightarrow Fe^{2+} + \cdot Cl \tag{6.8}$$

In addition, Cl^- gives inhibiting effects for the scavenger activity on OH radicals through Equations (6.9) and (6.10) [5, 25, 26], by forming $ClOH^-$ radicals that successively promotes Equation (6.11) in which Cl radicals are produced.

$$\cdot OH + Cl^- \rightarrow \cdot ClOH^- \tag{6.9}$$

$$\cdot OH \ + \ Cl^- + \ O_2 \rightarrow HOCl \ + \ \cdot O_2^- \qquad (6.10)$$

$$\cdot ClOH^- \ + \ H^+ \ \rightarrow \ \cdot Cl \ + \ H_2O \qquad (6.11)$$

Cl radicals produced by Equations (6.8) and (6.11) can oxidize Fe^{2+} by Equation (6.12) [5] and react with Cl^- ions to form dichloride radical anions through Equation (6.13) [5] that is a strong oxidant radical species.

$$\cdot Cl \ + \ Fe^{2+} \rightarrow Cl^- + \ Fe^{3+} \qquad (6.12)$$

$$\cdot Cl \ + \ Cl^- \ \rightarrow \ \cdot Cl_2^- \qquad (6.13)$$

The yield of Cl_2^- radical formation depends on Cl^- and H_2O_2 concentrations and on solution acidity of the Photo-Fenton process [27]. Cl_2^- radical represents the predominant species that can actively participate in disinfection processes for its ability to oxidize H_2O_2 and Fe^{2+} with a rate constants of the same order of magnitude than those of OH radicals (Equations 6.14–6.16) [5] increasing therefore the inactivation rate of Photo-Fenton process.

$$\cdot Cl_2^- \ + \ H_2O_2 \rightarrow \cdot O_2H \ + \ 2Cl^- \qquad (6.14)$$

$$\cdot Cl_2^- \ + \cdot O_2H \ \ \rightarrow \ O_2 + \ H^+ + \ 2Cl^- \qquad (6.15)$$

$$\cdot Cl_2^- \ + \ Fe^{2+} \rightarrow Cl^- + \ FeCl^{2+} \qquad (6.16)$$

Lastly, termination reactions of Cl_2^- radicals (Equations 6.17–6.19) can led to the formation of free chlorine that can actively participate in the disinfection process justifying the decrease of Cl^- concentration during the processes.

$$\cdot Cl_2^- \ + \ \cdot Cl_2^- \ \ \rightarrow \ Cl_2 \ + \ 2Cl^- \qquad (6.17)$$

$$\cdot Cl_2^- \ + \ \cdot OH \ \rightarrow \ HOCl \ + \ Cl^- \qquad (6.18)$$

$$\cdot Cl_2^- \ + \ \cdot Cl \ \rightarrow \ Cl_2 \ + \ Cl^- \qquad (6.19)$$

All obtained results with Cl^- for SODIS and Photo-Fenton processes are schematized in Figure 6.4.
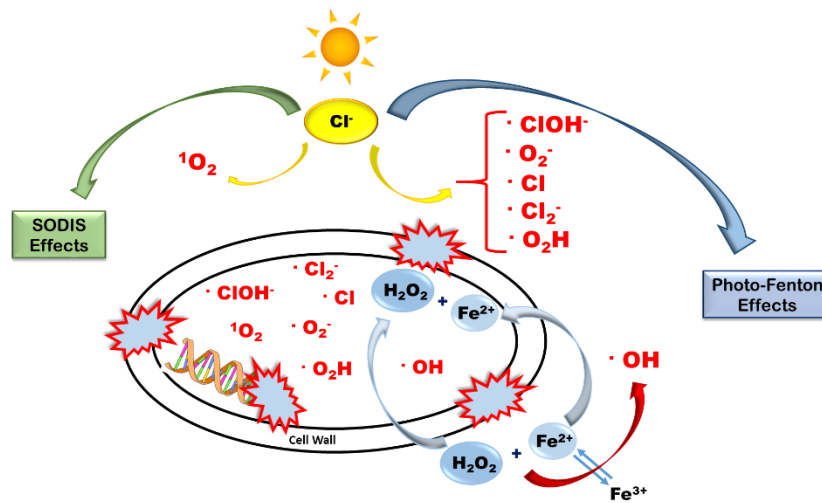

Figure 6.4: *Schematic representation of Cl^- effects for SODIS and Photo-Fenton processes.*

6.3.3. SO_4^{2-} Effects

The presence of sulphate in the environment is due to atmospheric and terrestrial processes. Major natural contributors of SO_4^{2-} to the environment are sulphur released from erosion of evaporite deposits and sulphide containing rocks and minerals as well as volcanoes. During this cycle, SO_4^{2-} is taken up by plants and microorganisms, and is later consumed by animals, thereby moving sulphur through the food chain.

Table 6.4 resumes the pseudo first order kinetic constants values calculated for both SODIS and Photo-Fenton processes for all tested SO_4^{2-} concentrations that are graphically showed in Figure 6.5 (a), while Figure 6.5 (b) shows the most significant disinfection graphs for both processes. Results demonstrated that for SODIS treatment there are not significant changes in reaction kinetics with all SO_4^{2-} concentrations, while an increase in the inactivation rate for Photo-Fenton has been obtained. In addition, both pH and SO_4^{2-} concentration showed no substantial shift during SODIS and Photo-Fenton treatments.

Table 6.4: *Kinetic constants values with different SO_4^{2-} concentration.*

SO_4^{2-}	SODIS		Photo-Fenton	
	k	STD	k	STD
mg L^{-1}	min^{-1}		min^{-1}	
0	0.0299	0.012	0.0614	0.010
10	0.0343	0.010	0.0665	0.020
20	0.0303	0.010	0.0737	0.040
50	0.0305	0.010	0.0976	0.040
250	0.0287	0.010	0.0938	0.040
500	0.0299	0.010	0.0845	0.030
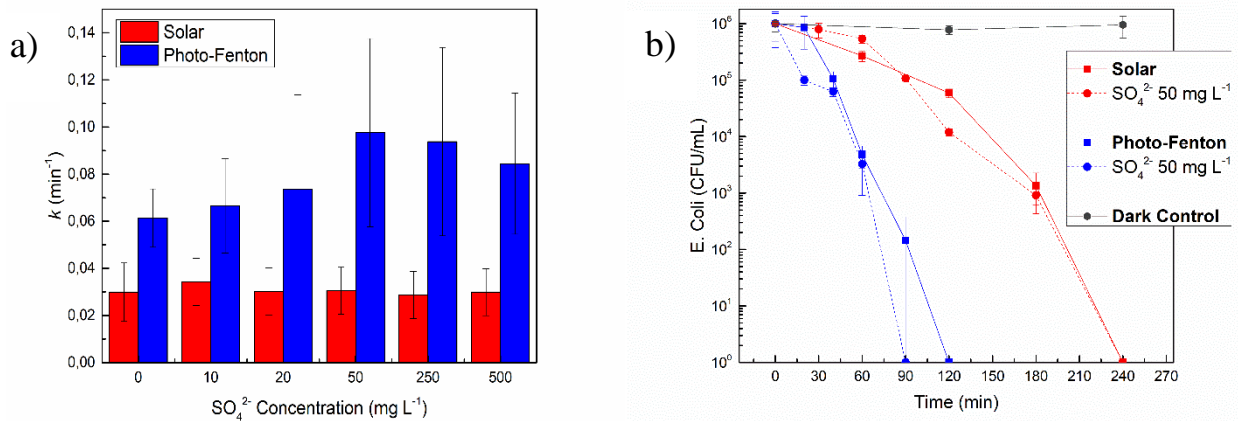
Figure 6.5: *Kinetic constants values with different SO_4^{2-} concentrations for SODIS and Photo-Fenton processes (a). Disinfection experiments with SO_4^{2-} (b).*

The behaviour on SODIS can be explained by the UV light absorption of SO_4^{2-} that protects E. Coli from light [28] according to disinfection results obtained by only solar light that appears not to be efficient enough.

In the Photo-Fenton process, the presence of SO_4^{2-} ions promote the formation of $FeSO_4$, $Fe(OH)^{2+}$, $FeSO_4^+$ and $Fe(SO_4)_2$ that affect the concentration of the Fe^{2+} and Fe^{3+} ions [29]. Among these species, the major predominant Fe^{3+} compound at pH 3.0, further $Fe(OH)^{2+}$, is $FeSO_4^+$ that adsorb at 350 nm and its irradiation produces Fe^{2+} ions and SO_4^- radical anions through Equation (6.20). In

addition, the presence of SO_4^{2-} causes a quenching effect for OH radicals generating SO_4^- radicals as shown in Equation (6.21).

$$FeSO_4^+ + hv \rightarrow Fe^{2+} + \cdot SO_4^- \tag{6.20}$$

$$SO_4^{2-} + \cdot OH \rightarrow \cdot SO_4^- + OH^- \tag{6.21}$$

SO_4^- radical obtained by these reactions, in water and in presence of H_2O_2, leads to the formation of additional OH and O_2H radical species by Equations (6.22) and (6.23) regenerating SO_4^{2-} ions; these ions can participate together in water disinfection, leading therefore to an increase in the Photo-Fenton process efficiency [26, 30].

$$\cdot SO_4^- + H_2O \rightarrow H^+ + SO_4^{2-} + \cdot OH \tag{6.22}$$

$$\cdot SO_4^- + H_2O_2 \rightarrow H^+ + SO_4^{2-} + \cdot O_2H \tag{6.23}$$

All obtained results with SO_4^{2-} for SODIS and Photo-Fenton processes are schematized in Figure 6.6.
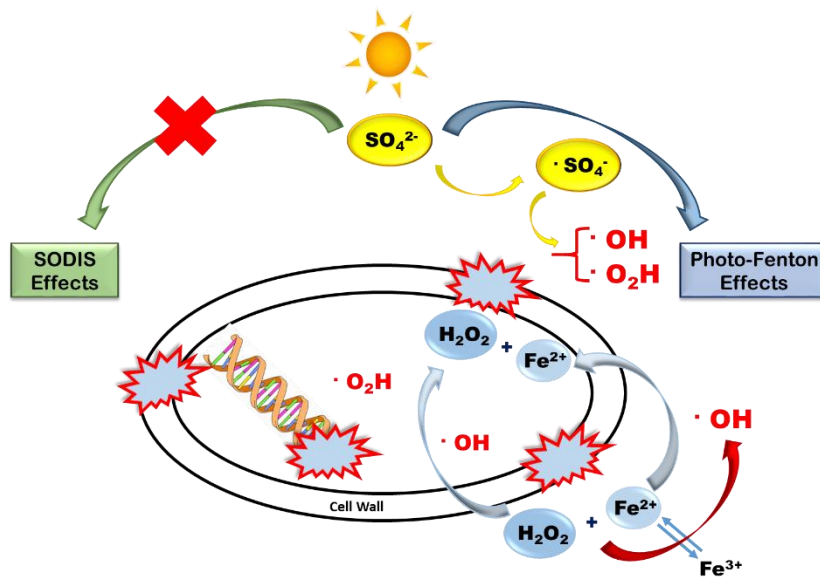

Figure 6.6: *Schematic representation of SO_4^{2-} effects for SODIS and Photo-Fenton processes.*

6.3.4. NO_3^- and NO_2^- Effects

Nitrate and nitrite are naturally occurring ions that are part of the nitrogen cycle; these ions can reach both surface water and groundwater because of agricultural activity, in fact, fertilizers contain inorganic nitrogen and wastes contain organic nitrogen that are first decomposed to give ammonia and then oxidized to give NO_2^- and successively NO_3^-.

Figures 6.7 (a) and (b) show all pseudo first order kinetic constants values calculated for both SODIS and Photo-Fenton processes for all NO_3^- and NO_2^- tested concentrations that are numerically reported in Tables 6.5 and 6.6 respectively while the most significant disinfection graphs for both processes are reported in Figure 6.7 (c).

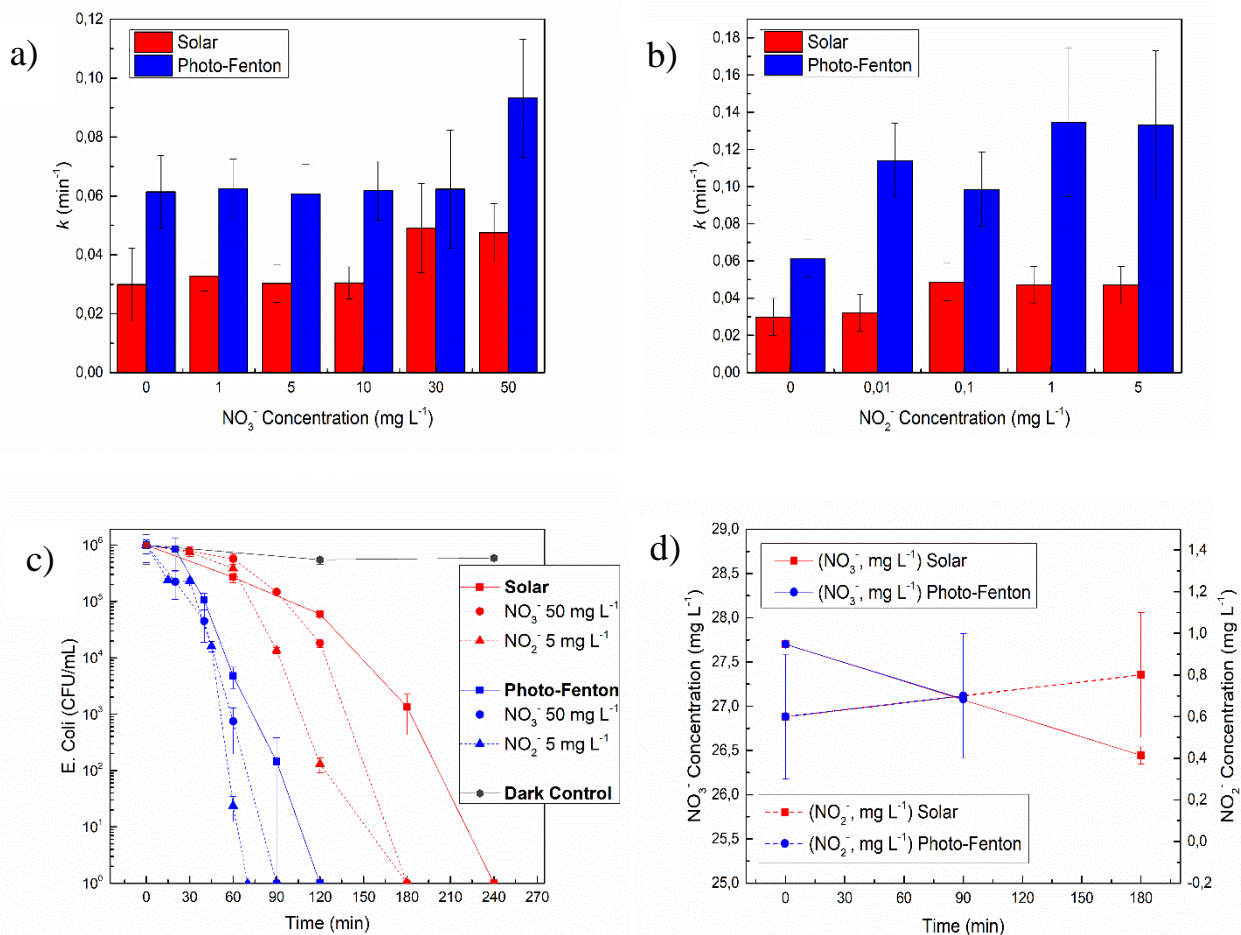

Figure 6.7: *Kinetic constants values with different NO_3^- (a) and NO_2^- (b) concentrations for SODIS and Photo-Fenton processes. Disinfection experiments with NO_3^- and NO_2^- (c). Changes of concentrations during processes (d).*

For both SODIS and Photo-Fenton processes disinfection kinetics increase with all tested concentration of NO_3^- and NO_2^- and this effect was greater for NO_2^- than for NO_3^-. In order to better understand this behaviour, pH and concentration changes of NO_3^- and NO_2^- were analysed during both processes. The pH of both reaction systems was near neutral and showed no substantial shift during SODIS and Photo-Fenton treatments respect to the same in the absence of these ions while, for both processes, the NO_3^- concentration decreases and the NO_2^- concentration undergoes a slight increase, as shows in Figure 6.7 (d). The similar effects of NO_3^- and NO_2^- ions in each process suggests that their effects are related only to photocatalytic reactions of these ions.

Table 6.5: *Kinetic constants values with different NO_3^- concentration.*

	SODIS		Photo-Fenton	
NO_3^-	k	STD	k	STD
mg L^{-1}	min^{-1}		min^{-1}	
0	0.0299	0.012	0.0614	0.010
1	0.0327	0.005	0.0625	0.010
5	0.0303	0.006	0.0607	0.010
10	0.0305	0.005	0.0618	0.010
30	0.0491	0.015	0.0623	0.020
50	0.0475	0.010	0.0932	0.020

Table 6.6: *Kinetic constants values with different NO_2^- concentration.*

	SODIS		Photo-Fenton	
NO_2^-	k	STD	k	STD
mg L^{-1}	min^{-1}		min^{-1}	
0	0.0299	0.012	0.0614	0.010
0.01	0.0322	0.010	0.1140	0.020
0.1	0.0487	0.010	0.0986	0.020
1	0.0471	0.010	0.1347	0.040
5	0.0470	0.010	0.1330	0.040

It is not surprising that NO_3^- and NO_2^- play a significant role in photochemical treatments. The absorption spectra of NO_3^- [31, 32] and NO_2^- [33], showed in Figure 6.8, in fact contain intense $\pi - \pi$ bands at 200 nm and 205 nm and weak n – π bands at 310 and 360 nm respectively.
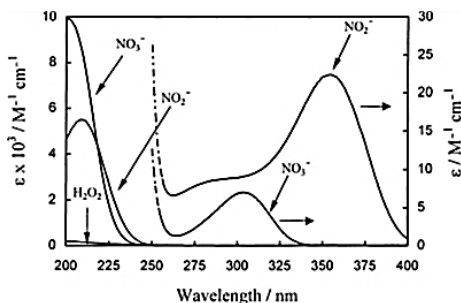

Figure 6.8: *UV-Vis absorption spectra of NO_3^- and NO_2^- [34].*

The presence of these anions gives a filter effect reducing the fraction of the incident UV radiation absorbed by H_2O_2 or gives the formation of additional radical species through photolytic process [35] with potential applications in AOPs [36, 37]. Photolysis of NO_3^- is a relevant source of OH radicals in natural waters while NO_2^-, although present at lower concentrations than NO_3^-, due to its higher molar absorptivity and photolysis quantum yield, represents a competitive photoactive compound [38]. Therefore, because the irradiation of NO_3^- represents one source of NO_2^-, their photochemical reactivity cannot be dissociated.

Photolysis of NO_3^- by light adsorption occurs in three main pathways [34]:

1) Formation of NO₂ and OH radicals by Equations (6.24) and (6.25)

$$NO_3^- + hv \rightarrow \cdot NO_2 + \cdot O^- \tag{6.24}$$

$$\cdot O^- + H_2O \rightarrow OH^- + \cdot OH \tag{6.25}$$

2) Formation of NO_2^- and $O(^3P)$ through Equation (6.26)

$$NO_3^- + hv \rightarrow NO_2^- + O(^3P) \tag{6.26}$$
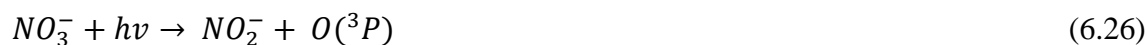
3) Isomerization to form peroxynitrite/peroxynitrous acid by light adsorption below 280 nm as shown in Equations (6.27) and (6.28) or by the recombination reaction of NO₂ and OH radicals shown in Equation (6.29)

$$NO_3^- + hv \rightarrow ONO_2^- \tag{6.27}$$

$$ONO_2^- + H^+ \rightarrow HOONO \tag{6.28}$$

$$\cdot NO_2 + \cdot OH \rightarrow HOONO \tag{6.29}$$

Similarly, the photolysis of NO_2^- in the 200–400 nm region results in the formation of NO and O^- radicals through Equation (6.30) and the subsequent protonation of O^- radicals gives the formation of additional OH radicals as shown in Equation (6.25) [34]. In addition, recombination reaction of NO and OH radicals (Equation 6.31) and the reaction of NO_2^- with OH radical (Equation 6.32) limit the steady-state concentration of OH radicals [34].

$$NO_2^- + hv \rightarrow \cdot NO + \cdot O^- \tag{6.30}$$

$$\cdot NO + \cdot OH \rightarrow HNO_2 \tag{6.31}$$

$$NO_2^- + \cdot OH \rightarrow \cdot NO_2 + OH^- \tag{6.32}$$

The UV irradiation of HNO₂ regenerates NO and OH radicals by Equation (6.33) and in solution containing O₂, NO radicals oxidizes to form NO_3^- as shown in Equations (6.34) and (6.35) [34].

$$HNO_2 + hv \rightarrow \cdot OH + \cdot NO \tag{6.33}$$

$$\cdot NO + \cdot NO \rightarrow N_2O_2 + O_2 \rightarrow N_2O_4 \tag{6.34}$$

$$N_2O_4 + H_2O \rightarrow NO_2^- + NO_3^- + 2H^+ \tag{6.35}$$

Therefore, the presence of NO_3^- and NO_2^- ions lead to the formation of additional OH radicals and other reactive species positively affecting both SODIS and Photo-Fenton processes, increasing their efficiency. All obtained results with NO_3^- and NO_2^- for SODIS and Photo-Fenton processes are schematized in Figure 6.9.
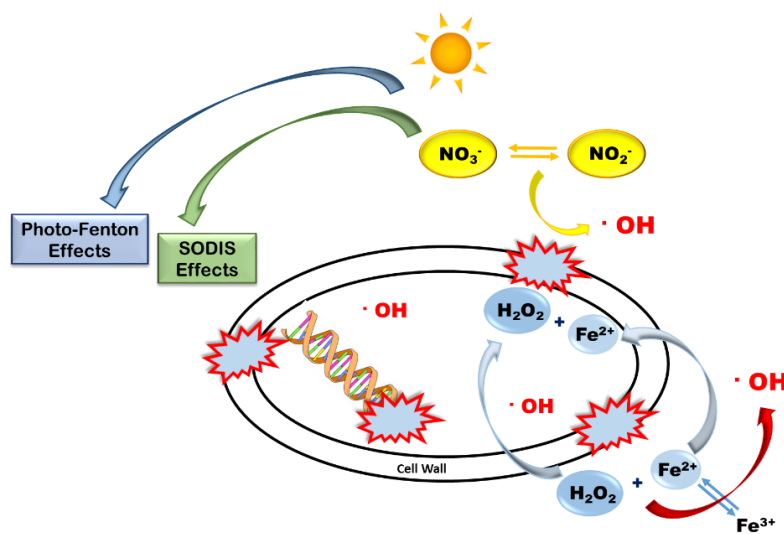

Figure 6.9: *Schematic representation of NO_3^- and NO_2^- effects for SODIS and Photo-Fenton processes.*

6.3.5. NH_4^+ Effects

Ammonia is a colourless inorganic compound usually in gaseous form with a characteristic pungent odour. Ammonia is irritating to the skin, eyes, nose, throat, and lungs and it is essential for many biological processes. The main local problem of NH_3 released into air is the unpleasant odour, which is detectable even at low concentrations, while the harm caused by NH_4^+ in water bodies is more serious, because it is very toxic to aquatic organisms.

Table 6.7 reports the pseudo first order kinetic constants values calculated for both SODIS and Photo-Fenton processes for all tested NH_4^+ concentrations that are graphically showed in Figure 6.10 (a), while the most significant disinfection graphs for both processes are reported in Figure 6.10 (b). For SODIS treatment there are not significant changes in reaction kinetics with all tested NH_4^+ concentrations, while an increase of inactivation rate in Photo-Fenton process it has been observed; the pH of both systems, depending on initial NH_4^+ concentration used, not showed change during both processes.

No variation in the NH_4^+ concentration was observed during SODIS treatment (Figure 6.10 c), demonstrating that the only action of solar light was not enough to improve the efficiency because no additional radical species are produced.

Table 6.7: *Kinetic constants values with different NH_4^+ concentration.*

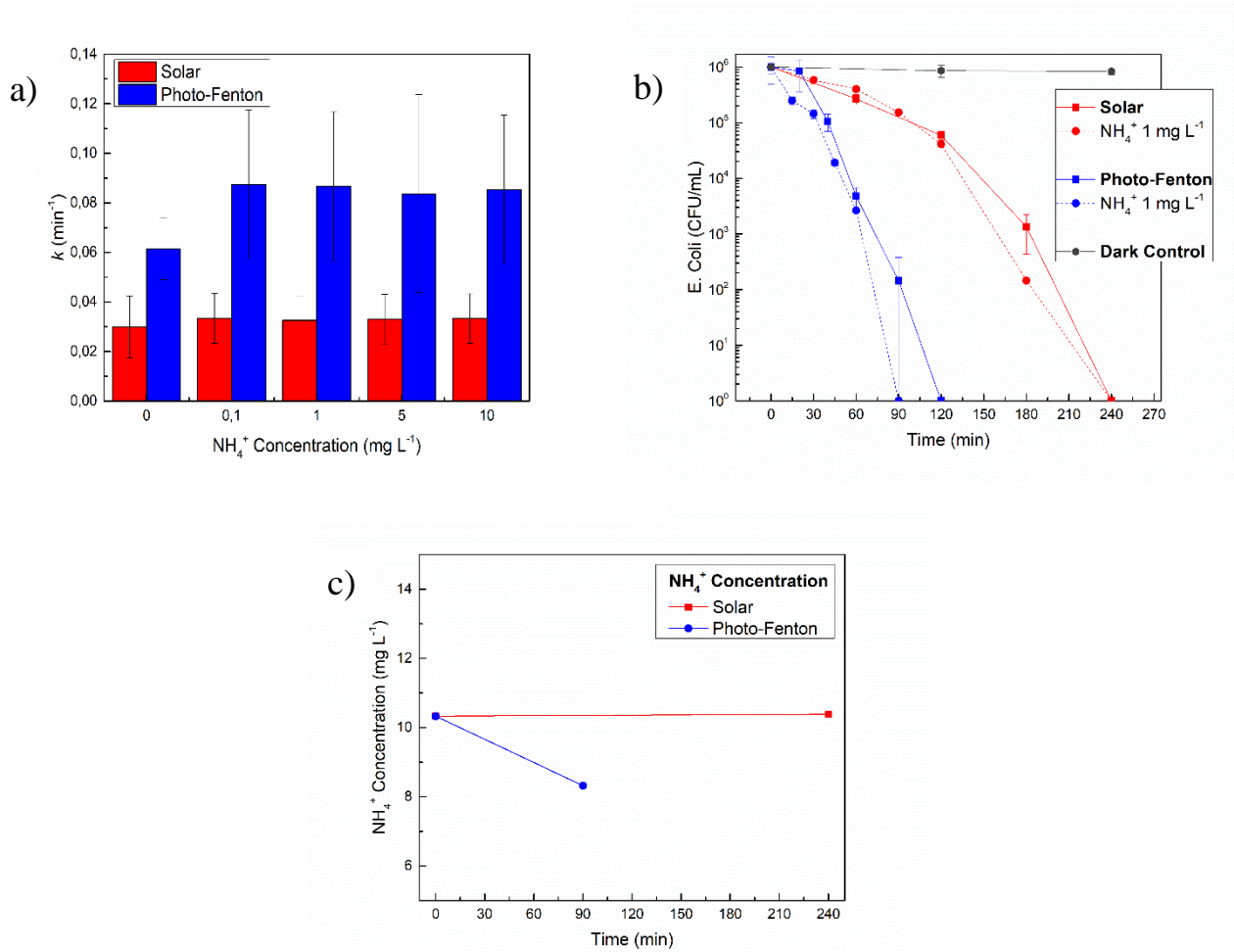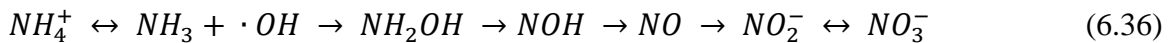|	SODIS		Photo-Fenton	
NH_4^+	k	STD	k	STD
mg L^{-1}	min^{-1}		min^{-1}	
0	0.0299	0.012	0.0614	0.010
0.1	0.0334	0.010	0.0874	0.030
1	0.0325	0.010	0.0867	0.030
5	0.0331	0.010	0.0837	0.040
10	0.0333	0.010	0.0854	0.030

Figure 6.10: *Kinetic constants values with different NH_4^+ concentrations for SODIS and Photo-Fenton processes (a). Disinfection experiments with NH_4^+ (b). Changes of NH_4^+ concentration during processes (c).*

However, the use of Photo-Fenton reagents showed a decrease in NH_4^+ concentration (Figure 6.10 c) due to Equation (6.36) in which the ammonia photo oxidation by OH radicals generates NO_2^- and NO_3^- ions [39].

$$NH_4^+ \leftrightarrow NH_3 + \cdot OH \rightarrow NH_2OH \rightarrow NOH \rightarrow NO \rightarrow NO_2^- \leftrightarrow NO_3^- \qquad (6.36)$$

In particular, the photochemical reduction of NO_3^- leads to NO_2^- and OH radical through Equation (6.37), while that of NO_2^- leads to NO and OH radical through Equation (6.38) [40, 41], justifying therefore the increase of inactivation rate.

$$NO_3^- + H_2O + h\nu \rightarrow NO_2^- + OH^- + \cdot OH \qquad (6.37)$$

$$NO_2^- + H_2O + h\nu \rightarrow NO + OH^- + \cdot OH \qquad (6.38)$$

All obtained results with NH_4^+ for SODIS and Photo-Fenton processes are schematized in Figure 6.11.
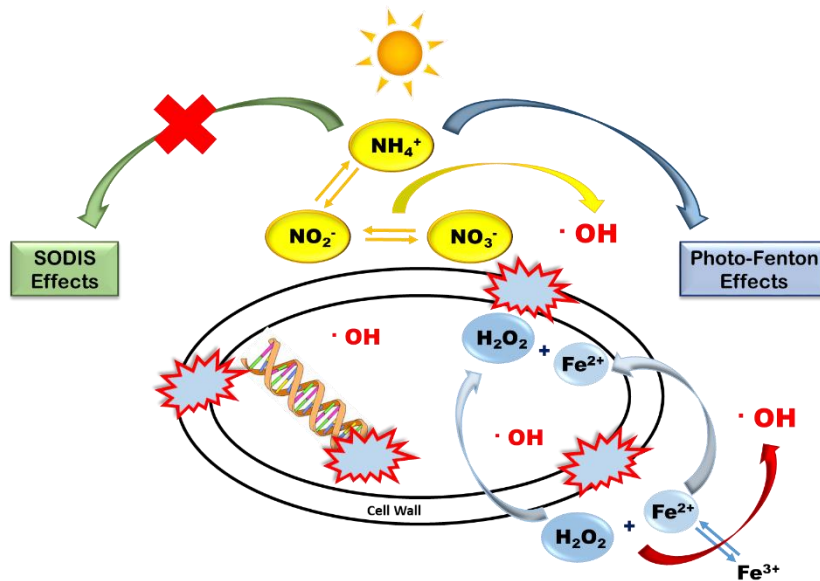

Figure 6.11: *Schematic representation of NH_4^+ effects for SODIS and Photo-Fenton processes.*

6.3.6. Combined Effects of OH Radicals Production Processes in the Presence of other Ions

Combined effects of OH radicals production processes (SODIS treatment with NO_3^- and NO_2^- and Photo-Fenton process) with SO_4^{2-}, HCO_3^- and Cl^-, which are scavengers active, with specific ions concentration was also studied. All obtained results are resumed in Figure 6.12 (a), (b) and (c) while Figure 6.12 (d) shows the pseudo first order kinetic constants values calculated for all experiments.

In the case of the production of OH radicals using NO_3^- and NO_2^- ions in SODIS treatment, observed rate constants in presence of SO_4^{2-}, HCO_3^- and Cl^- are very low compared to disinfection rates in the absence of these ions and are close to the rate constant of normal SODIS.

In addition, by using the Photo-Fenton process for the production of OH radicals, observed rate constants in presence of SO_4^{2-} and Cl^- are higher, while in the presence of HCO_3^- are very low compared to disinfection rates in absence of these ions.

All these results demonstrate that, in presence of NO_3^- and NO_2^-, all other ions act as scavengers of OH radicals, decreasing the efficiency of SODIS treatment. However, by using Photo-Fenton only

HCO_3^- acts as scavenger of OH radicals due to its high concentrations, while the presence of SO_4^{2-} and Cl^- generates an increase in disinfection kinetics for the reasons before described by using separated ions.
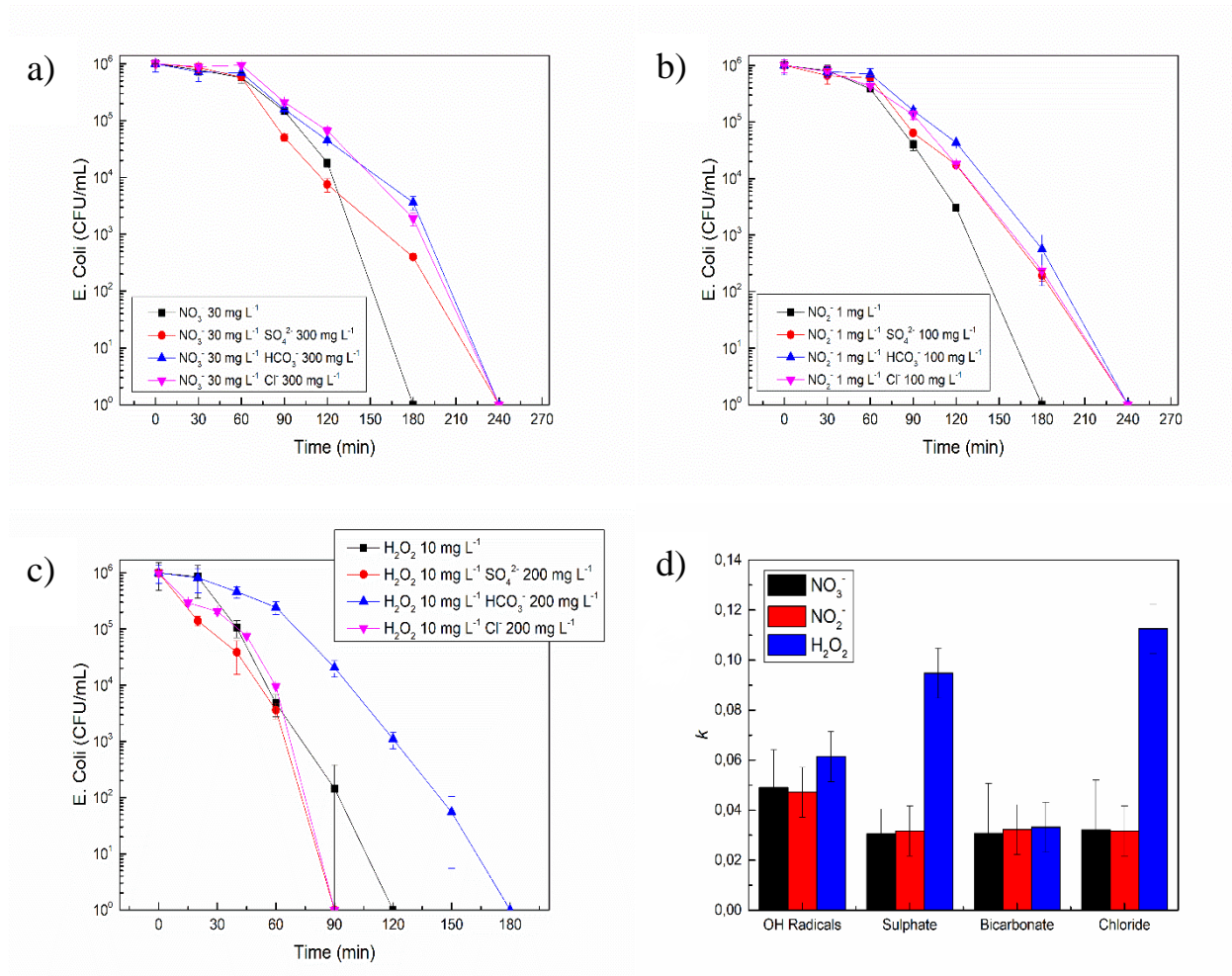

Figure 6.12: *Disinfection experiments of SO_4^{2-}, HCO_3^- and Cl^- combined effect with NO_3^- (a), NO_2^- (b) and H_2O_2 (c). Kinetic constants values (d).*

6.3.7. Combined Effect of Ions with Natural Organic Matter

The presence of Natural Organic Matter (NOM) in water can act as a filter of radiation and affect the inactivation of E. Coli [14]. However, UV light absorption by Dissolved Organic Matter (DOM) promote the triplet state and its deactivation occurs in several ways, including a reaction with oxygen to form singlet oxygen, as reported by Equations (6.39) and (6.40) [14].

$$DOM + hv \ \rightarrow \ {}^1DOM \ \rightarrow \ {}^3DOM^* \tag{6.39}$$

$$ {}^3DOM^* + \ O_2 \ \rightarrow DOM + \ {}^1O_2 \tag{6.40}$$

Singlet oxygen can react forming peroxidation products that interact with water contaminants increasing the efficiency of photochemical processes [42]. In addition, in presence of iron in water containing DOM, complex species like Fe^{3+} - DOM are generated showing higher light absorbance and quantum yields facilitating ligand to metal charge transfer as shows in Equation (6.41) and therefore contributing in bacteria inactivation [42].

$$Fe^{3+} - DOM + hv \ \rightarrow Fe^{2+} + \ DOM^+_{OX} \tag{6.41}$$

In these experiments, NOM actively participated in E. Coli inactivation for both SODIS and Photo-Fenton processes as it may be see in Table 6.8 and 6.9 respectively. Furthermore, in order to verify the effect of the presence of NOM on the efficiency of processes, combined effect on SODIS and Photo-Fenton processes with all ions in the presence of 2 mg L^{-1} of NOM was also monitored. Specifically, in the presence of NOM with all used ions, the only action of solar light in the SODIS treatments was not enough to improve the efficiency of process respect to the same in the presence of only NOM, as evidenced in Figure 6.13 suggesting a filter action of NOM that attenuated the radiation protecting bacteria.

In addition, the combined effect of NOM with NO_3^-, Cl^-, SO_4^{2-} and NH_4^+ in the Photo-Fenton process (Figure 6.14) not demonstrated variation in disinfection kinetics respect to the same in the presence of only NOM due, also in this case, to NOM radiation filter.

On the contrary, NOM and NO_2^- acted in additive way, as shown in Figure 6.14, increasing the production of OH radicals and the efficiency of process. In particular, in this case is opportune to evidence the comparison between specific kinetic constants in the presence of only NOM ($k_1 = 0,1057$) and only NO_2^- ($k_2 = 0,1330$) with that of NOM and NO_2^- ($k_{1,2} = 0,1545$). Considering $k'_{1,2}$ (Equation 6.42) the calculated constant as sum of respective active compounds while $k''_{1,2}$ (Equation 6.43) as the lost derived from the experimental process, the calculated $k''_{1,2}$ value is 0.0228.

$$k'_{1,2} = k_1 + k_2 - k_0 \tag{6.42}$$
$$k''_{1,2} = k'_{1,2} - k_{1,2} \ = k_1 + k_2 - k_0 - k_{1,2} \tag{6.43}$$

This fact can be explained considering that a portion of light adsorption of NO_2^- is out of that of NOM permitting only a part of the photochemical reactions attributed to this ion. These conditions are

favourable in the Photo-Fenton process while do not give benefit in SODIS treatment. In fact, if the correction value is subtracted to kinetic constant value of SODIS treatment in the presence of NO_2^- ($k_2' = 0.0470$), is then explained the different behaviour between two methods.

When instead disinfection processes was performed with NOM and HCO_3^-, the only positive effect is that of NOM; in this case, the evident suppression of the HCO_3^- effect was probably due to pH change that affects the formation of HCO_4^- due to the acidity of DOM that is largely made up of humic substances (e.g. humic and fulvic acids) [43].

Table 6.8: *Kinetic constants values for SODIS treatment.*

	k min^{-1}	STD
SODIS	0.0299	0.012
NOM	0.0478	0.010
NOM/HCO$_3^-$	0.0331	0.020
NOM/Cl$^-$	0.0468	0.010
NOM/SO$_4^{2-}$	0.0470	0.010
NOM/ NO$_3^-$	0.0478	0.010
NOM/NO$_2^-$	0.0419	0.010
NOM/NH$_4^+$	0.0459	0.010

Table 6.9: *Kinetic constants values for Photo-Fenton process.*

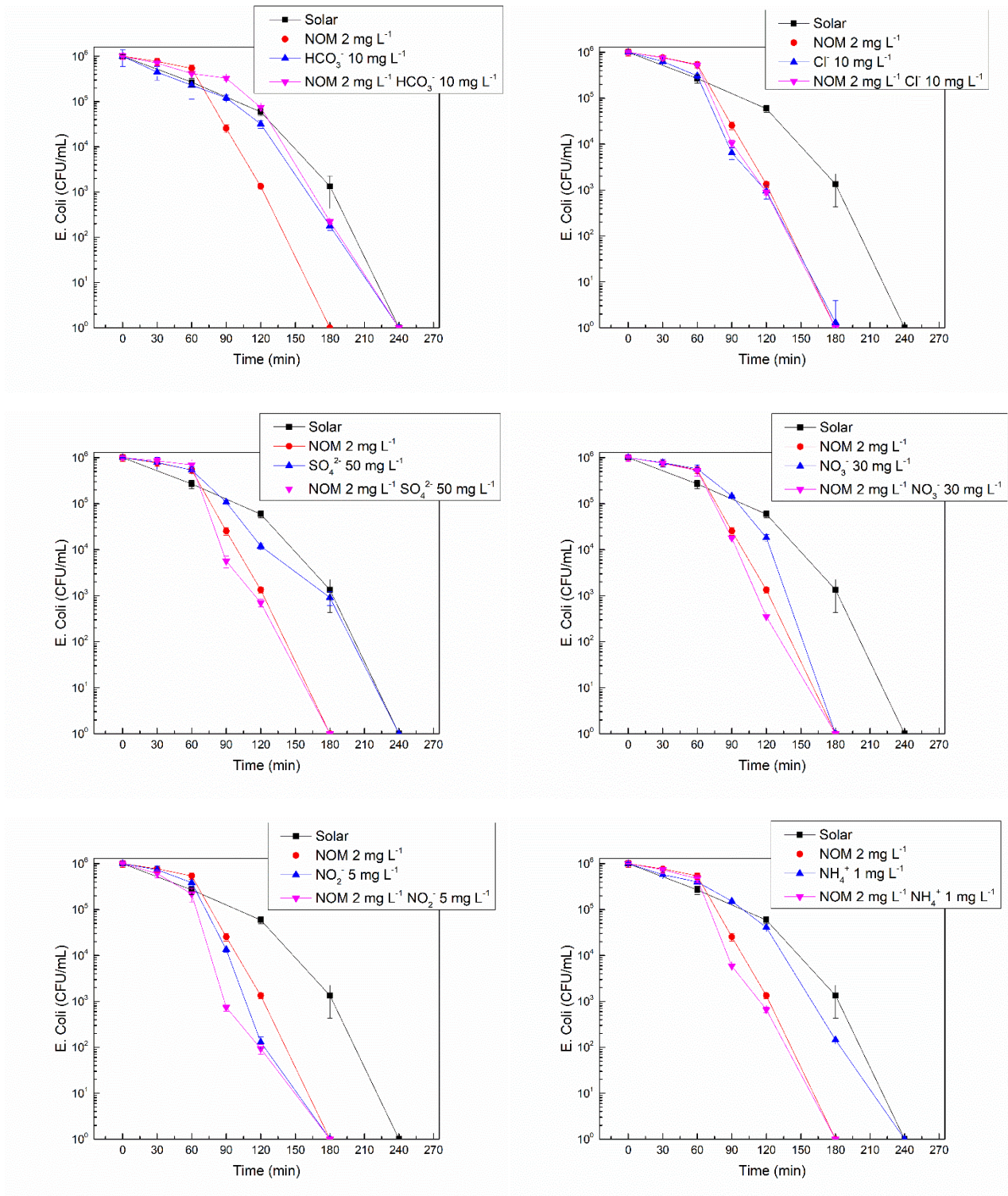|	k min^{-1}	STD
Photo-Fenton	0.0614	0.010
NOM	0.1057	0.030
NOM/HCO$_3^-$	0.1051	0.020
NOM/Cl$^-$	0.1053	0.020
NOM/SO$_4^{2-}$	0.1067	0.030
NOM/ NO$_3^-$	0.0673	0.020
NOM/NO$_2^-$	0.1545	0.020
NOM/NH$_4^+$	0.0947	0.020

Figure 6.13: *Combined effect of all ions with NOM in SODIS treatment.*
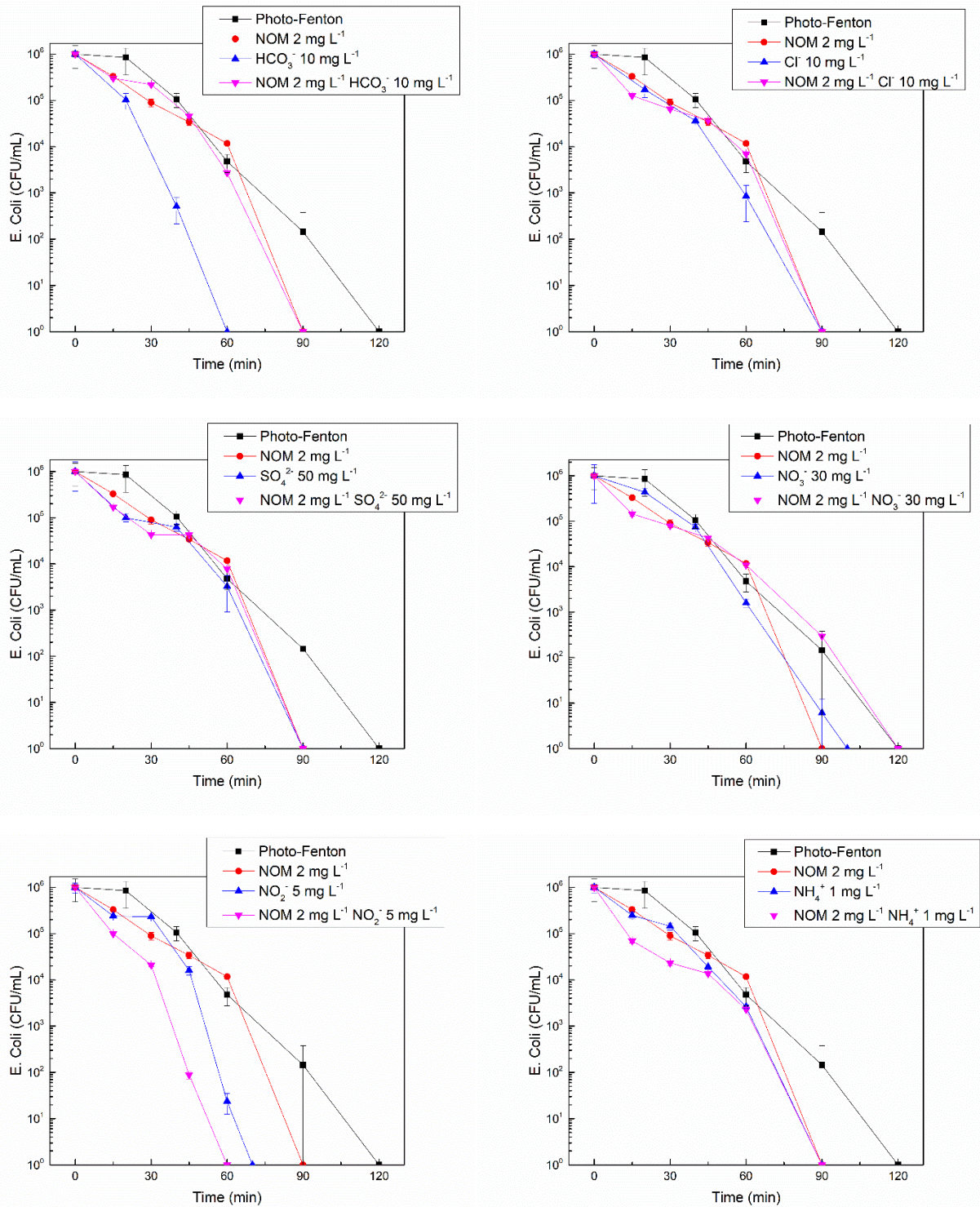
Figure 6.14: *Combined effect of all ions with NOM in Photo-Fenton process.*

All obtained results in presence of NOM for SODIS and Photo-Fenton processes are schematized in Figure 6.15 and 6.16 respectively.
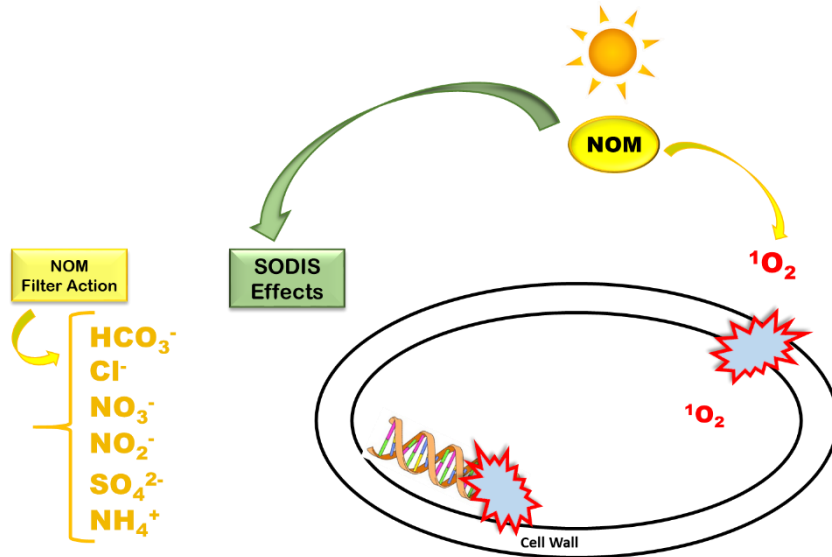

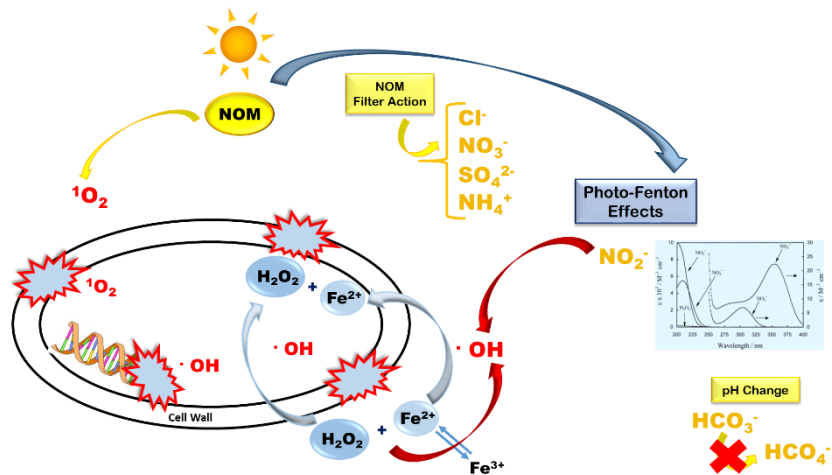***Figure 6.15:*** *Schematic representation of SODIS treatment.*

Figure 6.16: *Schematic representation of Photo-Fenton process.*

Conclusions

The effect of inorganic ions and natural organic matter present in aqueous E. Coli suspension on the SODIS and Photo-Fenton disinfection was studied in order to known the effect of the presence of individual ions on the efficiency of both processes. Because the sensitivity of bacteria to disinfection treatment can be influenced by chemical characteristics of waters, as composition, concentration of ions and pH, these characteristics were modified during the process.

The obtained results show that the addition of NO_3^-, NO_2^- and Cl^- ions increase the disinfection kinetics for both processes; NO_3^- and NO_2^- ions are able to form additional OH radicals that can contribute to the degradation of E. Coli, while in presence of Cl^- ion, that should act as OH radicals scavenger, various radical species can be formed as result of oxidation increasing the disinfection efficiency.

In the presence of SO_4^{2-} and NH_4^+ ions, no significant variation in the kinetics of SODIS was observed because the only action of solar light was not enough to produce additional reactive radicals necessary for increase the efficiency of process. On the contrary, an increase in the disinfection kinetics in the presence of these ions with Photo-Fenton process was obtained. Despite SO_4^{2-} ion acts as scavenger for OH radicals, in water and in presence of H_2O_2, SO_4^{2-} ions lead to the additional generation of OH radicals and other radical species increasing therefore the Photo-Fenton efficiency. In the presence of NH_4^+ ions, because NO_2^- and NO_3^- ions were formed using Photo-Fenton reagents with the formation of additional active OH radicals, an increase in the efficiency of this disinfection process was observed.

HCO_3^- ions reduced SODIS disinfection because its light absorption limits the amount of light reaching bacteria. In addition, in water with a pH equal or greater than 8.3, HCO_3^- generate CO_3^{2-}, these ions at high concentrations decrease the efficiency of Photo-Fenton process due to quenching effect on OH radicals. At low concentrations, where the pH of reaction systems was near neutral, conditions were favourable for the formation of HCO_4^- that catalyse the process increasing the efficiency of disinfection.

The combined effect of processes that produce OH radicals with the other ions that are scavengers active was also studied. The observed disinfection efficiencies in the presence of SO_4^{2-}, HCO_3^- and Cl^- ions are very low compared to the degradation in the presence of only NO_3^- and NO_2^- ions to demonstrate that, in the presence of NO_3^- and NO_2^- ions, all other ions act as OH radicals scavengers, decreasing therefore the efficiency of SODIS treatment. Instead, in the Photo-Fenton process, an

increase in the efficiency is obtained with SO_4^{2-} and Cl^- confirming the production of other active radicals, like superoxide radical anion, that, together with OH radicals, can actively participate in disinfection, while using high HCO_3^- concentration the scavenger effect on OH radicals decreasing the Photo-Fenton efficiency.

NOM actively participates in SODIS and Photo-Fenton processes due to UV light adsorption that promote the singlet oxygen formation which contributes to bacterial inactivation. Finally, combined effect of NOM with all ions showed that the presence of NOM, due to its light filter properties, give a negative effect on disinfection processes except in the Photo-Fenton with NO_2^-; in fact, in this process NOM act in additive way, increasing the production of OH radicals and therefore its overall efficiency. In this combined effect, although there is an increase in efficiency, the incomplete additive effect is due to the partial light absorption of NO_2^- despite the NOM filtering action. The lost of efficiency in the Photo-Fenton process justify a not evident additive effect in the SODIS treatment.

References

[1] C. Ruales-Lonfat, J. F. Barona, A. Sienkiewicz, J. Vélez, L. N. Benítez and C. Pulgarín, *Appl. Catal. B: Environ.*, 2016, 180, 379–390.

[2] D. Vione, M. Minella, C. Minero, V. Maurino, P. Picco, A. Marchetto and G. Tartari, *Environ. Chem.*, 2009, 6, 407–415.

[3] K. Finlay, R. J. Vogt, M. J. Bogard, B. Wissel, B. M. Tutolo, G. L. Simpson and P. R. Leavitt, *Nature*, 2015, 19, 215–218.

[4] R. Bhateria and D. Jain, *Sustain. Water Resour. Manag.*, 2016, 2, 161–173.

[5] J. De Laat, G. Truong Le and B. Legube, *Chemosphere*, 2004, 55, 715–723.

[6] J. Ndounla and C. Pulgarin, *Environ. Sci. Pollut. Res.*, 2015, 22, 17082–17094.

[7] A. G. Rincón and C. Pulgarin, *Appl. Catal. B: Environ.*, 2004, 51, 283–302.

[8] S. Giannakis, E. Darakas, A. Escalas-Cañellas and C. Pulgarin, *Chem. Eng. J.*, 2015, 281, 588–598.

[9] A. H. Geeraerd, V. P. Valdramidis and J. F. Van Impe, *Int. J. Food. Microbiol.*, 2005, 102, 95–105.

[10] A. H. Geeraerd, C. H. Herremans and J. F. Van Impe, *Int. J. Food. Microbiol.*, 2000, 59, 185–209.

[11] E. W. Rice, R. B. Baird and A. D. Eaton, Standard Methods for the Examination of Water and Wastewater. *American Public Health Association, American Water Works Association, Water Environment Federation* (2017) ISBN: 9780875532875.

[12] N. Zhan, Y. Huang, Z. Rao and X. L. Zhao, *Chinese J. Anal. Chem.*, 2016, 44, 355–360.

[13] K. G. McGuigan, R. M. Conroy, H. J. Mosler, M. du Preez, E. Ubomba-Jaswa and P. Fernandez-Ibanez, *J. Hazard. Mater.*, 2012, 235–236, 29–46.

[14] D. Rubio, E. Nebot, J. F. Casanueva and C. Pulgarin, *Water Res.*, 2013, 47, 6367–6379.

[15] C. A. S. Regino and D. E. Richardson, *Inorg. Chim. Acta*, 2007, 360, 3971–3977.

[16] H. Yao and D. E. Richardson, *J. Am. Chem. Soc.*, 2000, 122, 3220–3221.

[17] B. Balagam and D. E. Richardson, *Inorg. Chem.*, 2008, 47, 1173–1178.

[18] D. E. Richardson, C. A. S. Regino, H. R. Yao and J. V. Johnson, *Free Radical Biol. Med.*, 2003, 35, 1538–1550.

[19] A. Jawad, Z. Chen and G. Yin, *Chin. J. Catal.*, 2016, 37, 810–825.

[20] L. Zhou, W. Song, Z. Chen and G. Yin, *Environ. Sci. Technol.*, 2013, 47, 3833–3839.

[21] D. B. Medinas, G. Cerchiaro, D. F. Trindade and O. Augusto, *IUBMB life*, 2007, 59, 255–262.

[22] H. Chen, L. Lin, Z. Lin, G. Guo and J. M. Lin, *J. Phys. Chem. A*, 2010, 114, 10049–10058.

[23] L. Ge, J. Chen, X. Qiao, J. Lin and X. Cai, *Environ. Sci. Technol.*, 2009, 43, 3101–3107.

[24] J. Kiwi, A. Lopez and V. Nadtochenko, *Environ. Sci. Technol.*, 2000, 34, 2162–2168.

[25] A. Machulek Jr., J. F. Moraes, C. Vautier-Giongo, C. A. Silverio, L. C. Friedrich, C. A. O. Nascimento, M. C. Gonzalez and F. Quina, *Environ. Sci. Technol.*, 2007, 41, 8459–8463.

[26] L. Gomathi Devi, C. Munikrishnappa, B. Nagaraj and K. Eraiah Rajashekhar, *J. Mol. Catal. A: Chem.*, 2013, 374–375, 125–131.

[27] X. Y. Yu and J. R. Barker, *J. Phys. Chem. A*, 2003, 107, 1313–1324.

[28] B. Sengul Topac and U. Alkan, *Int. J. Civ. Eng.*, 2016, 20, 2632–2639.

[29] A. Machulek Jr., J. F. Moraes, L. T. Okano, C. A. Silvério and F. H. Quina, *Photochem. Photobiol. Sci.*, 2009, 8, 985–991.

[30] F. Ghanbari and M. Moradi, *Chem. Eng. J.*, 2017, 310, 41–62.

[31] E. Rotlevi and A. Treinin, *J. Phys. Chem.*, 1965, 69, 2645.

[32] H. J. Maria, J. R. McDonald and S. P. McGlynn, *J. Am. Chem. Soc.*, 1973, 95, 1050.

[33] S. J. Strickler and M. Kasha, *J. Am. Chem. Soc.*, 1963, 85, 2899.

[34] J. Mack and J. R. Bolton, *J. Photochem. Photobiol., A. Chem.*, 1999, 128, 1–13.

[35] M. von Grätzel, S. Taniguchi and A. Henglein, *Ber. Bunsenges Phys. Chem.*, 1970, 74, 488.

[36] P. Bilski, C. F. Chignell, J. Szychlinski, A. Borkowski, E. Oleksy and K. Reszka, *J. Am. Chem. Soc.*, 1992, 114, 549.

[37] P. A. King, V. E. Anderson, J. O. Edwards, G. Gustafson, R. C. Plumb and J. W. Suggs, *J. Am. Chem. Soc.*, 1992, 114, 5430.

[38] I. Wagner, H. Strehlow and G. Busse, *Z. Phys. Chemie. Neue Folge*, 1980, 123, 1.

[39] J. Ndounla and C. Pulgarin, *Sci. Total Environ.*, 2014, 493, 229–238.

[40] J. C. Fanning, *Coord. Chem. Rev.*, 2000, 199, 159–179.

[41] D. Kotzias, K. Hustert and A. Wieser, *Chemosphere*, 1987, 16, 505–511.

[42] S. Giannakis, *Environ. Sci. Pollut. Res. Int.*, 2018, 25, 27676–27692.

[43] F. J. Rodríguez, P. Schlenger and M. García-Valverde, *Sci. Total Environ.*, 2016, 541, 623–637.